DARK COSMOLOGY CENTRE
UNIVERSITY OF COPENHAGEN

Diana Juncher

Master's Thesis

SEARCHING FOR ATTRACTORS IN CLUSTERS OF GALAXIES

July 1, 2011

Supervisor: Steen H. Hansen

Cover illustration: The Bullet Cluster (1E0657-56)

Abstract

In this thesis we perform numerical simulations of cluster sized structures containing both gas and dark matter in the search for one or more attractors. We create ten different structures with a wide range of initial conditions and expose them to three different perturbations: perturbations of the dark matter, perturbations of the gravitational constant, and mergers. We use the TreeSPH code GADGET-2 to evolve the structures using both adiabatic simulations and simulations with radiation and star formation.

We find that the Jeans relation for dark matter, which has previously been proven to hold for structures containing only dark matter, holds for the dark matter in clusters as well. Even more interestingly, for the simulations with radiation and star formation, we find a very simple relation between the temperature of the gas and the properties of the dark matter, which holds at radii beyond the central star forming region of about 20kpc.

Finally, we discuss how these attractors can lead to 1) an estimate of the total mass of a cluster of galaxies by observations of its galaxies alone, and 2) an indirect measurement of the dark matter velocity anisotropy in galaxies or galaxy clusters.

Table of Contents

1 Introduction

Dark matter plays a central role in modern astronomy, and it appears in many different ares of study such as the cosmic microwave background radiation, structure formation and the dynamics of galaxies. Despite accounting for more than 80% of the matter in the universe, dark matter has never been observed directly, and a concrete understanding of its nature remains elusive.

Through indirect observations it is possible to estimate the mass distribution of dark matter in both galaxy and cluster sized structures, but more intricate properties such as the velocity anisotropy cannot be studied in this way. Fortunately, the past decades' advancement in computer performance has provided us with an alternative: numerical simulations.

High resolution cosmological simulations have revealed a number of universal profiles such as the radial dependencies of the density profile and the velocity anisotropy. However, the origin of these profiles is still an unsolved problem. Essentially there are two possibilities: either the found universalities are just a consequence of how the structures were created, or there exists one or more attractors. With this thesis we seek to determine if such attractors exist. We will do this by exposing equilibrated structures containing gas and dark matter to series of controlled perturbations and examine how these affect the structures.

In Section 2 we will briefly introduce the reader to the basics of clusters of galaxies, focusing on their two main components: gas and dark matter. We will discuss the various methods with which the two are observed, how they are typically distributed in the cluster and the fundamental difference between their collisional and collisionless properties. We will also discuss what kind of particles might constitute the unknown dark matter.

With the basics in place we will in Section 3 engage in a more detailed analysis of the properties of gas and dark matter. For the gas, we will derive the hydrostatic equation of equilibrium that describes how the pressure of the gas in a cluster is balanced by the total gravitational force of the cluster. We will also outline the physics of adiabatic processes and the more complicated processes of radiation and star formation. For the dark matter, we will derive the collisionless Boltzmann equation, which is a partial differential equation that describes stable distributions of dark matter particles in the cluster phase space. We will discuss two types of solutions to the equation that both rely on conserved quantities of the cluster. Finally, we will consider the existence of attractors in clusters of galaxies and discuss how these might be of use.

In Section 5 we will describe in detail, how we create ten equilibrated structures that differ in both dark matter density and anisotropy. We will use the TreeSPH code GADGET-2 to evolve these structures, and and overview of its main algorithms is presented in Section 4. In Section 6 we perform a series of thorough tests of the simulations parameters and the created structures to make sure everything works as it should, and that the created structures really are in

equilibrium.

In Section 7 we introduce the three types of perturbations, we will use: mild perturbations of the dark matter velocities, violent perturbations of the gravitational constant, and mergers. These perturbations give rise to both phase maxing and violent relaxation, two processes that are thought to play important roles in the relaxation of cosmological structures.

In Section 8 and 9 we present the results of our adiabatic simulations and simulations with radiation and star formation, respectively. For both types of simulations, we examine how the perturbations affect the structures, and we look for attractors of the dark matter and of the interaction between the dark matter and the gas. The results of the study are presented and discussed in Section 10.

In Section 11 we offer our conclusions.

I would like to thank my supervisor Steen H. Hansen for many inspiring discussions and guidance during the last 12 months. I would also like to thank Andrea V. Macciò for patiently answering all my questions regarding GADGET-2 and star formation. Martin Sparre also deserves thanks for his technical assistance. Last but not least, I would like to thank the Dark Cosmology Centre for giving me the opportunity to do my master's thesis with them.

2 Galaxy Clusters

Most galaxies are found in groups or clusters of galaxies. These are the largest known gravitationally bound structures in the universe, and they range from small groups that contain barely enough mass to hold themselves together to dense clusters with thousands of galaxies. Our own Milky Way is part of the Local Group, a small cluster with about 40 known members.

Typical galaxy clusters contain 50 to 1,000 galaxies, span from 2 to 10 megaparsecs and have total masses of 10^{14} to 10^{15} solar masses. Their great masses allow the velocity dispersions of the individual galaxies to reach an impressive 1000 kilometres per second. According to the standard model of big bang cosmology, the ΛCDM-model, the formation of galaxy clusters took place according to the bottom-up scenario, where individual galaxies formed first and then collected into clusters. As a consequence, galaxy clusters started forming relatively recently, and they are therefore dynamically young: a typical galaxy has completed only a few orbits since the formation of its cluster.

Only about 2% of the total mass of a galaxy cluster can be found in the stars of the galaxies. X-ray observations reveal a hot, diffuse gas between the galaxies, the intracluster medium (ICM), which accounts for about 11% of the total mass. The last 87%, the majority of the mass of a galaxy cluster, lies in the invisible dark matter [3, p. 32].

2.1 The Intracluster Medium

During the formation of a galaxy cluster, the release of gravitational energy heats the ICM, allowing it to reach temperatures between 10 and 100 million Kelvin. This may seem very hot, but at that temperature, the gas particles move at about 1000 km/s, which is comparable to the speed of the individual galaxies in the cluster.

The ICM consists primarily of hydrogen and helium, but there are also traces of iron and other heavy elements. Despite containing most of the baryons in the cluster, the average density of the gas is only about 10^{-3} particles per cubic centimetre. On average the metallicity of the ICM in a cluster is about one third of that of our Sun. Since the heavier elements can only be produced by fusion in stars or supernovae, some of the hot gas must have been ejected from stars within the galaxies in the cluster. However, there is too much hot gas in clusters for all of it to have come from stars. Most of it must have existed as intergalactic gas since the time the cluster formed.

2.1.1 Methods of Observation

Because of its high temperatures, the elements present in the ICM are ionised. The light elements have all the electrons removed from their nuclei, while the

heavier elements are missing only some of their electrons. This gives rise to a strong X-ray radiation in the the form of bremsstrahlung and atomic line emission. In Section 3.1.5 we will take a closer look at the physical processes behind this radiation.

Since the Earth's atmosphere absorbs the vast majority of X-rays, they are not detectable from Earth-based telescopes. Instead we use space-based telescopes such as the Chandra X-ray Observatory to study the ICM. X-ray observations of bremsstrahlung allow us to determine the density and temperature of the radiating gas. Furthermore, observations of X-ray emission and absorption spectra reveal the abundances of the various elements present in the gas.

2.1.2 Density Distribution

The density profile of the ICM is traditionally described by the β-model [6],

$$\rho_g(r) = \rho_0 \frac{1}{\left[1 + \left(\frac{r}{r_0}\right)^2\right]^{3\beta/2}}, \tag{2.1}$$

where 3β corresponds to the outer logarithmic slope of the profile, and the scale radius r_0 specifies at which radius the profile curves. The model has a flat core and a constant logarithmic slope beyond the scale radius. More recent observations of galaxy clusters have revealed that the gas density in the centres of relaxed clusters usually has a power-law-type cusp instead of a flat core, and that at larger radii the density profile tends to steepen relative to the power law at smaller radii [41]. A better estimate of the gas density is therefore

$$\rho_g(r) = \rho_0 \frac{1}{\left(\frac{r}{r_0}\right)^\alpha} \frac{1}{\left[1 + \left(\frac{r}{r_0}\right)^2\right]^{(3\beta-\alpha)/2}} \frac{1}{\left[1 + \left(\frac{r}{r_1}\right)^2\right]^{(\delta-\beta)/2}}, \tag{2.2}$$

where α, 3β and δ correspond to the inner, middle and outer logarithmic slopes of the profile respectively, and r_0 and r_1 specifies at which radii the profile curves.

2.1.3 Collisional Properties

The gas particles in the ICM interact with each other via the electromagnetic force. In other words, gas particles are collisional. Whenever two gas particles collide, they will exchange energy and momentum, and it is through this process that a gas will reach equilibrium; a state in which the motion of the particles is as random as possible. Because of the randomness, the average properties of the gas are the same in all directions. On a macroscopic scale we can therefore refer to the temperature or pressure of a gas, quantities that can be related by an equation of state.

2.2 Dark Matter

The existence of dark matter was first suggested in the early 1930s by the Swiss astronomer Fritz Zwicky [28, p. 134]. While studying the Coma Cluster of galaxies he noticed that the speeds of the galaxies in the cluster were too large for the mass of the visible stars and gas to hold them together. To explain this obvious contradiction, Zwicky suggested that the cluster contained a large amount of matter, which for some reason was unobservable: dark matter. In the following decades numerous observations of objects ranging from dwarf galaxies to the cosmic microwave background radiation and large scale structures have supported this idea, and dark matter is now an essential part of modern astronomy.

2.2.1 Methods of Observation

Zwicky discovered dark matter by observing, how the gravitational pull of its mass affected luminous matter. Much of the evidence for dark matter has been found using this indirect method of observation. A classic example is the observations of edge-on spiral galaxies, for which we can compare the velocity curves with the luminosity distribution and clearly see how the stars move faster in their orbits than expected.

Another way of detecting dark matter is by the use of gravitational lensing. Just like normal matter, dark matter can bend light by an angle that depends only on the mass of the dark matter and the distance at which the light passes. We can therefore map a distribution of dark matter by measuring the distortion and magnification of the light from galaxies in the background.

Last but not least, we can determine the mass of dark matter in galaxy clusters by observing the X-ray radiation from the ICM. The equation of hydrostatic equilibrium relates the total mass of gravitating matter as a function of radius to the radial gas temperature and gas density in a cluster. The two latter can be inferred from the X-ray observations, and if the structure is in hydrostatic equilibrium we can then find the mass distribution of the dark matter.

2.2.2 Density Distribution

The density distribution of a dark matter structure is often described by a double power-law function

$$\rho_{DM}(r) = \rho_0 \frac{1}{\left(\frac{r}{r_0}\right)^{\alpha}} \frac{1}{\left(1+\frac{r}{r_0}\right)^{\delta-\alpha}}, \tag{2.3}$$

where α and δ correspond to the inner and outer logarithmic slopes of the function respectively, and the scale radius r_0 specifies at which radius the function curves [3, p. 70]. The popular Jaffe ($\alpha = 2$, $\delta = 4$), Hernquist ($\alpha = 1$, $\delta = 4$) and NFW ($\alpha = 1$, $\delta = 3$) models are all double power-law functions of this form.

One of the first general properties of dark matter to be discovered was the relation between the mass density and the radius:

$$\gamma(r) = \frac{\mathrm{d}\ln(\rho_{DM}(r))}{\mathrm{d}\ln(r)}. \tag{2.4}$$

Simulations show that $\gamma(r)$ typically goes from about -1 in the central region to -3 in the outer regions [25, 36]. Observations of large structures such as galaxy clusters are in fair agreement with simulations [4, 5, 26, 41].

2.2.3 Collisionless Properties

Dark matter particles are very weakly interacting. In fact, observations suggest that dark matter is collisionless. The Bullet cluster is one of the most famous examples of this. It was first observed in the year 2000 and consists of two colliding clusters of galaxies: a bullet-like sub-cluster is seen exiting its main cluster with a bow shock. The stars, gas and dark matter behave in different ways during the collision. By observing in visible light, one can see the stars and galaxies passing right through each other, while X-ray observations reveal the hot gas slowing down as a result of the collision. The dark matter distribution was mapped in 2003 by the use of gravitational lensing [9], and it was seen to be moving as the stars of the clusters: it was not lagging behind like the colliding gas. This strongly supports the idea of collisionless dark matter.

Another indication that dark matter structures are collisionless is the value of their velocity anisotropy defined by

$$\beta = 1 - \frac{\sigma_\theta^2 + \sigma_\phi^2}{2\sigma_r^2}, \tag{2.5}$$

where σ_r^2, σ_θ^2 and σ_ϕ^2 are the radial and tangential velocity dispersions [3, p. 294]. In theory, the velocity anisotropy can take on values between 1 (perfect radial orbits) and $-\infty$ (perfect circular orbits). For a collisional gas, $\beta = 0$ as a result of the scattering of the particles. If dark matter was collisional, we would therefore expect the velocity anisotropy of dark matter structures to be zero. However, recent observations show that β is significantly different from zero and seems to grow with the distance to the centre [16, 19]. Furthermore, simulations of collisionless dark matter structures show that β is radially varying and goes from about 0 in the inner regions to 0.5 in the outer regions [10]. The observations and simulations are in remarkable agreement implying that dark matter structures are effectively collisionless.

2.2.4 The Dark Matter Particle

Even though dark matter plays a significant role in the evolution of our universe, a concrete understanding of its nature still remains elusive. Early theories hypothesised that dark matter was made up of non-luminous objects such as black

holes, neutron stars, white and brown dwarfs and planets, collectively known as MACHOs (MAssive Compact Halo Objects). Astronomical surveys such as MACHO, EROS and OGLE have since the early nineties searched for these hidden MACHOs in the halo of our Milky Way. Some candidates have been found, but their number is nowhere near sufficient to explain the missing dark matter in the universe [12, p. 17]. The majority of dark matter is therefore thought to be non-baryonic, i.e. made of one or more elementary particles other than the usual electrons, protons and neutrons.

The non-baryonic dark matter candidates can be divided into two groups: hot dark matter and cold dark matter. Neutrinos are the prototype of hot dark matter. For a long time they were considered a good dark matter candidate. Apart from gravity, neutrinos only interact with normal matter via the weak force making them very difficult to detect. However, observations indicate that the average neutrino mass is too small for neutrinos alone to account for the expected amount of dark matter [12, p. 272-275].

The cold dark matter candidates are commonly referred to as WIMPs (Weakly Interacting Massive Particles). They are provided in supersymmetric extensions of the Standard Model of particle physics. WIMPs have masses of 10 to 10,000 times greater than that of a proton and, as the name suggests, only interact very weakly with other particles. As a consequence, they are difficult to observe. The DAMA experiment has claimed to directly detect WIMPs, though many scientists remain sceptical of their results.

The models of galaxy formation depend very sensitively on whether the universe is dominated by hot or cold dark matter. In a universe dominated by low-mass neutrinos, small fluctuations in the early universe would not have grown to galaxies, as the super-relativistic neutrinos could easily have escaped from these mass aggregations. As a result, structure formation would have taken place according to the top-down scenario, where larger structures form first and subsequently fragment to form smaller structures such as galaxies. This would imply that galaxies formed only for redshifts $z \leq 1$. However, from observations we know that even for $z \geq 3$ large populations of galaxies existed [12, p. 281-282].

WIMPs are non-relativistic because of their high masses, so they are easily bound gravitationally to mass fluctuations of small sizes. In a universe dominated by cold dark matter, the initially small mass aggregations would collapse and grow by further mass attractions to form galaxies. These galaxies would then develop galaxy clusters and later superclusters. Cold dark matter therefore favours a bottom-up scenario, a model that agrees very well with the COBE and WMAP observations of the cosmic microwave background [12, p. 282-283].

From the above discussion, evidence suggests that the universe is dominated by cold dark matter. Therefore the following work will be based on the cold dark

matter model, and the term “dark matter” will from now on refer to cold dark matter.

3 Theory

Gas particles constantly collide with each other and thus constantly change direction as they move through the ICM. Dark matter particles, on the other hand, move freely in collisionless orbits. This fundamental difference between their behaviours is reflected in the equations that describe their dynamics. We will therefore derive and discuss these equations separately in the following.

3.1 The Intracluster Medium

3.1.1 The Ideal Gas Law

Because the ICM is both very diffuse and very hot, we can to a good approximation use the ideal gas law to describe the relation between the pressure, density and temperature of the gas. It states that

$$P_g = \frac{k_B}{\langle m_g \rangle} \rho_g T_g, \tag{3.1}$$

where P_g, ρ_g and T_g are the gas pressure, density and temperature, respectively, k_B is Boltzmann's constant and $\langle m_g \rangle$ is the average mass of a gas particle. The latter can also be written

$$\langle m_g \rangle = \mu m_u, \tag{3.2}$$

where μ is the mean molecular mass of the gas, and m_u is the atomic mass constant. The mean molecular mass depends on the element abundances in the gas. In a primordial gas, where the mass fraction of hydrogen is $X \approx 74\%$, the mass fraction of helium is $Y \approx 24\%$ and the mass fraction of heavier elements is $Z \approx 2\%$, the mean molecular mass is

$$\mu = \frac{1}{2X + \frac{3}{4}Y + \frac{1}{2}Z} \approx 0.6. \tag{3.3}$$

For details see Appendix A.1.

3.1.2 The Equation of Hydrostatic Equilibrium

Although the motion of the single gas particles appears perfectly random, their mass distribution and temperature adhere to a higher level of order on a larger scale. In a galaxy cluster, the pressure of the ICM gas is balanced by the total gravitational force of the cluster. This balance is called hydrostatic equilibrium, and if the cluster is spherical, it can be described by the radial component of Euler's equation

$$\frac{\partial v_r}{\partial t} + v_r \frac{\partial v_r}{\partial r} - \frac{v_\theta^2 + v_\phi^2}{r} = -\frac{1}{\rho_g} \frac{\partial P_g}{\partial r} - \nabla \Phi, \tag{3.4}$$

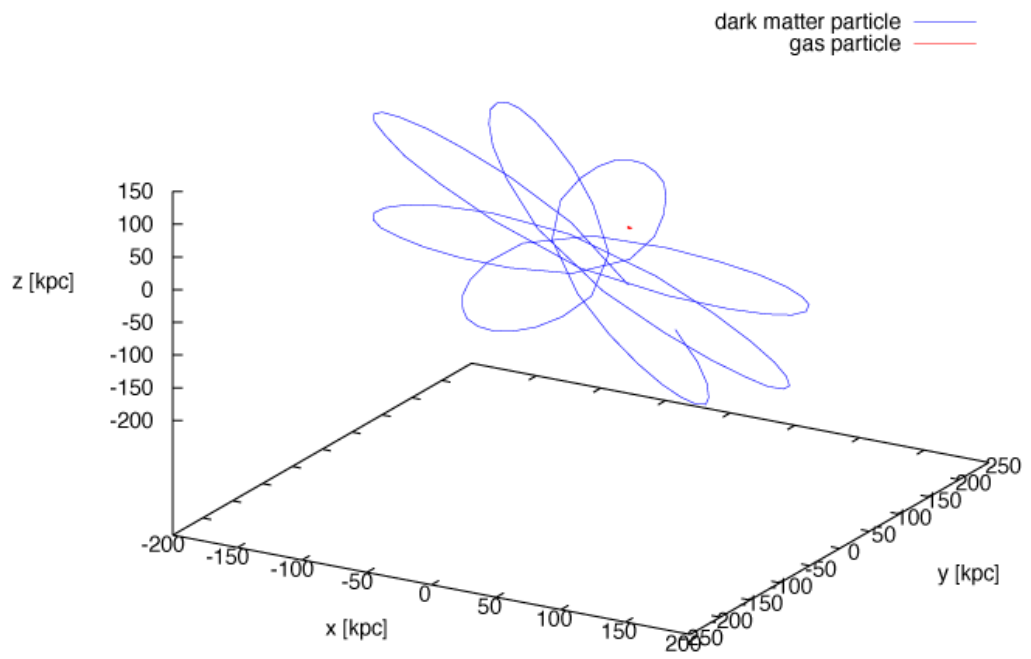

Figure 3.1: *Paths of a gas particle and a dark matter particle in a simulated galaxy cluster. The gas particle (red) is constantly scattered, while the dark matter particle (blue) moves freely in a collisionless orbit.*

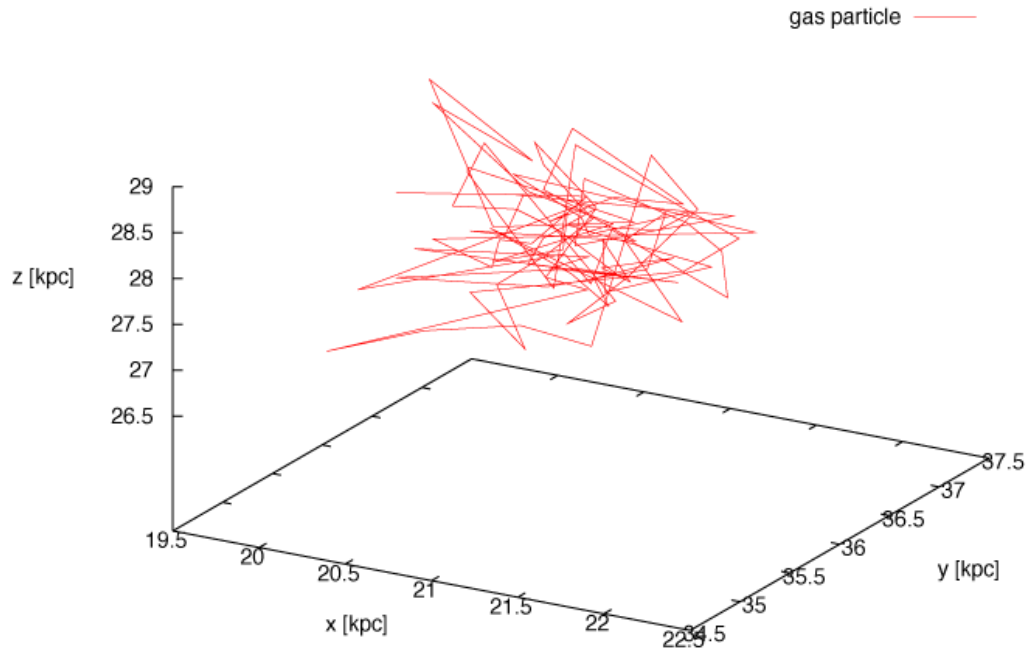

Figure 3.2: *Close-up of the gas particle's path in figure 3.1. Here the scattering is obvious.*

where t is the time, v_r, v_θ and v_ϕ are the velocities of the gas, r is the distance from the centre and Φ is the total gravitational potential (Euler's equation is derived in Appendix A.2). Note that the only forces acting on the gas is pressure and gravity, so the gas is assumed to be inviscid [3, p. 809]. If the gas is at rest, then $v_r = v_\theta = v_\phi = 0$, and the equation reduces to

$$0 = \frac{1}{\rho_g}\frac{\mathrm{d}P_g}{\mathrm{d}r} + \frac{\mathrm{d}\Phi}{\mathrm{d}r} = \frac{1}{\rho_g}\frac{\mathrm{d}P_g}{\mathrm{d}r} + \frac{GM}{r^2}, \tag{3.5}$$

where M is the total mass of the galaxy cluster. Recalling the ideal gas law from equation (3.1) and using that

$$\frac{\mathrm{d}\ln x}{\mathrm{d}x} = \frac{1}{x} \Rightarrow \mathrm{d}x = x\mathrm{d}\ln x, \tag{3.6}$$

we find that

$$\begin{aligned} 0 &= \frac{1}{\rho_g}\frac{k_B}{\langle m_g\rangle}\frac{\mathrm{d}(\rho_g T_g)}{\mathrm{d}r} + \frac{GM}{r^2} \\ &= \frac{k_B T_g}{\langle m_g\rangle}\frac{1}{r}\frac{\mathrm{d}\ln(\rho_g T_g)}{\mathrm{d}\ln r} + \frac{GM}{r^2}. \end{aligned} \tag{3.7}$$

Rearranging, we end up with

$$M(r) = -r\frac{k_B T_g}{\langle m_g\rangle G}\left(\frac{\mathrm{d}\ln(\rho_g)}{\mathrm{d}\ln r} + \frac{\mathrm{d}\ln(T_g)}{\mathrm{d}\ln r}\right). \tag{3.8}$$

3.1.3 Temperature and Internal Energy

Equation (3.8) is a first order differential equation in T_g which has the solution

$$T_g(r) = \frac{1}{\rho_g(r)}\int_r^\infty \rho_g(r)\frac{G\langle m_g\rangle M(r)}{k_B r^2}\mathrm{d}r. \tag{3.9}$$

The internal energy of a monoatomic ideal gas is proportional to its temperature, and it is given by

$$U = \frac{3}{2}Nk_B T_g, \tag{3.10}$$

where N is the number of gas particles.

3.1.4 Adiabatic Processes

An adiabatic process is a process where no heat is transferred to or from the gas. The only way its temperature can change is by a change of volume or pressure. An adiabatic process is described by the equation

$$P_g V_g^\gamma \propto T_g V_g^{\gamma-1} = \text{constant}, \tag{3.11}$$

where V_g is the volume of the gas and γ is the adiabatic index, which is $\gamma = \frac{5}{3}$ for a monoatomic gas such as the ICM.

3.1.5 Radiative Cooling

The ICM strongly emits X-ray radiation because of its high temperatures. Figure 3.3 illustrates how the total luminosity of a gas of solar composition varies with the temperature. In the following, we will take a look at some of the processes behind this curve.

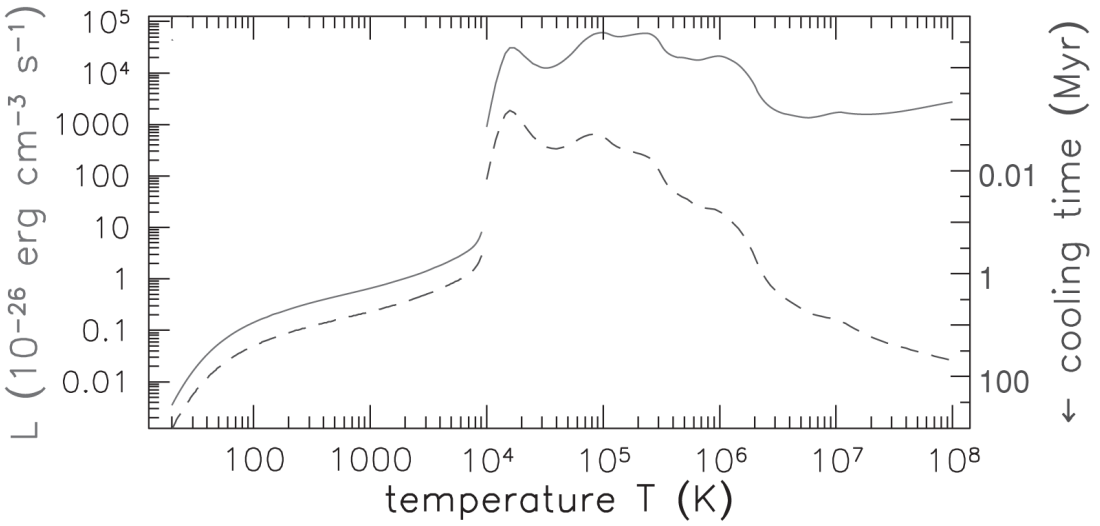

Figure 3.3: *Luminosity per volume per second (solid curve) and cooling time (broken curve) for a gas of solar composition. The density is one hydrogen atom per cubic centimetre for temperatures above* $10^4 K$ *[31, p. 106].*

Above about 10^7K the ICM is a plasma that is nearly entirely ionised. The hydrogen and helium are fully stripped off of their electrons, while the heavier elements have only few of their electrons. In this state, the ICM radiates by free-free radiation, also called bremsstrahlung. It is produced by the acceleration of a charged particle, when deflected by another charged particle. The radiation is continuous because the charged particles move freely in the plasma. Because the electron mass is so small compared to the mass of the atomic nuclei in the gas, bremsstrahlung is mainly produced by electrons. The luminosity is given by

$$L = \nu_g^2 \Lambda(T_g), \tag{3.12}$$

where ν_g is the number density of the gas, and $\Lambda(T_g)$ is the cooling function [37]. Since the latter depends only on the temperature, denser gas cools more rapidly. The cooling time, a measure of how fast the gas radiates away its thermal energy, is given by

$$t_{\text{cool}} \propto \frac{\nu_g T_g}{L} = \frac{T_g}{\nu_g \Lambda(T_g)}. \tag{3.13}$$

For bremsstrahlung, $\Lambda(T_g) \propto \sqrt{T_g}$, so hotter gas needs longer to cool. Gas at densities smaller than or equal to one hydrogen atom per cubic centimetre takes at least 1Gyr to cool from 10^7K or more [31, p. 263-264].

For temperatures between 10^5K and 10^7K the resonance lines of iron and other metals become the main coolants [31, p. 106]. Free electrons recombine with the ions and are initially in high excited states. They emit radiation when they subsequently jump to lower excitation states [21, p. 96]. For temperatures in the range $10^7 - 10^8$K, the main emission lines are from iron related transitions. There are also other radiation processes in play at these temperatures. Free-bound radiation and two-photon radiation both produce continuous radiation, while collisional excitation, dielectronic recombination and resonant excitation produce discrete line emission.

For temperatures between 10^4K and 10^5K the emission lines from forbidden transitions in metals become the main coolants. A forbidden line is produced when an electron jumps from an upper excitation state, where it can remain for a long time, to a lower excitation state. Such a jump has a very low transition probability and only occurs in low-density gases, since the excited atom would otherwise collide and loose the energy before radiating it away.

Below 10^4K the gas is no longer ionised, and there is a sharp drop in the luminosity.

Temperature	Cooling process	Spectral region
$> 10^7$K	free-free (bremsstrahlung)	X-ray
$10^7\text{K} < T_g < 10^8\text{K}$	iron resonance lines	X-ray
$10^5\text{K} < T_g < 10^7\text{K}$	metal resonance lines	UV, soft X-ray
$10^4\text{K} < T_g < 10^5\text{K}$	C, N, O, Ne forbidden lines	IR, optical

Table 3.1: *Main processes that cool the ICM gas [31, p. 106].*

Because the ICM is so diffuse, most of the radiation escapes without interacting with the plasma. The total X-ray luminosities range from about 10^{43}erg s^{-1} to 10^{46}erg s^{-1}. The gas therefore cools rapidly and needs a continuous energy supply to stay hot. Energy is added to the ICM by supernovae, galactic winds and active galactic nuclei.

3.1.6 Star Formation

The ICM will remain in hydrostatic equilibrium as long as the gas pressure is balanced by the gravitational pull of the whole cluster. The equilibrium is stable if small perturbations are damped and unstable if they are amplified. For a homogenous gas, a perturbation is amplified if its wavelength exceeds the Jeans length λ_J:

$$\lambda^2 > \lambda_J^2 = \frac{\pi c_s^2}{G\rho_g^0}, \tag{3.14}$$

where c_s is the speed of sound in the gas, or if the mass within a sphere of diameter λ_J exceeds the Jeans mass:

$$M > M_J = \frac{4\pi}{3}\rho_g^0 \left(\frac{1}{2}\lambda_J\right)^3. \tag{3.15}$$

In both equations ρ_g^0 is the first order density profile, i.e. the perturbation-free density [3, p. 401-406].

The Jeans mass depends on the density and temperature of the gas. In general, a gas cloud is unstable, if it is either very massive at a given temperature or very cold at a given mass. Once the Jeans mass is exceeded, the perturbations will grow as the gas cloud collapses under its own gravity. As it collapses, it breaks into smaller and smaller pieces in a hierarchical manner, until the fragments reach stellar mass. The fragments are heated as they collapse further until at some point, if a fragment is sufficiently massive, hydrogen begins to fuse in the core, and a star is born.

In triggered star formation, some event might occur to compress a gas cloud and initiate its gravitational collapse. For example, two gas clouds could collide with each other, or a nearby supernova explosion could send shocked matter into the gas cloud at very high speeds. An active galactic nuclei emits strong winds that can both limit and trigger star formation, depending on the type of jets.

3.2 Dark Matter

3.2.1 The Distribution Function

When modeling a system of many collisionless particles, it is neither practical nor worthwhile to follow the orbit of each particle. Instead we turn to statistics and introduce the distribution function f. It describes the probability of finding a particle in the six-dimensional phase space volume $\mathrm{d}^3\mathbf{x}\mathrm{d}^3\mathbf{v}$ around the position $\mathbf{x}$ and velocity $\mathbf{v}$ at a time t [3, p. 275]. If the particles in a system are all identical, they are described by the same distribution function. Because of its nature, f will always be larger than or equal to zero, and it is usually normalised such that

$$\int f(\mathbf{x}, \mathbf{v}, t)\mathrm{d}^3\mathbf{x}\mathrm{d}^3\mathbf{v} = 1. \tag{3.16}$$

We can find the number density at a given position $\mathbf{x}$ by integrating f over all velocity space:

$$\nu(\mathbf{x}) = \int f(\mathbf{x}, \mathbf{v})\mathrm{d}^3\mathbf{v}. \tag{3.17}$$

Multiplying by the total mass of the system M we obtain the density at $\mathbf{x}$:

$$\rho(\mathbf{x}) = M\nu(\mathbf{x}). \tag{3.18}$$

The probability that a particle at $\mathbf{x}$ has a velocity of $\mathbf{v}$ can be found using the definition of conditional probability:

$$P_{\mathbf{x}}(\mathbf{v})d^3\mathbf{v} = \frac{f(\mathbf{x},\mathbf{v})d^3\mathbf{v}}{\nu(\mathbf{x})}. \tag{3.19}$$

If we know the distribution function of a system of particles, we pretty much know everything there is to know about the system. The hard part is finding the distribution function.

3.2.2 The Collisionless Boltzmann Equation

The Collisionless Boltzmann Equation (CBE) is a partial differential equation that describes how the distribution function changes in time and phase space. To derive it, we can start by considering a single particle in a collisionless system. As it moves through phase space, the probability of finding it at any phase space location changes with time. The mass of the particle is conserved, and since the particle is collisionless so is its velocity. It follows that the probability is a conserved quantity. We can therefore describe the evolution of the distribution function using an equation similar to the continuity equation, where we use conservation of probability instead of conservation of mass [3, p. 276]. After a bit of math we arrive at the CBE (the full derivation can be found in Appendix A.3):

$$\frac{\mathrm{d}f(\mathbf{x},\mathbf{v},t)}{\mathrm{d}t} = 0. \tag{3.20}$$

Since f is a function of no less than 7 variables, the CBE can be quite difficult to solve. Fortunately, the Jeans Theorem can help us choose distribution functions which are solutions to the CBE. The theorem states that

> *Any steady-state solution of the collisionless Boltzmann equation depends on the phase space coordinates only through integrals of motion in the given potential, and any function of the integrals yields a steady-state solution of the collisionless Boltzmann equation* [3, p. 283].

In other words, any function of one or more conserved quantities of the system is a steady-state solution of the CBE.

3.2.3 Spherical Systems

Before we begin to explore possible solutions of the CBE, we will take a moment to consider the physics of spherical systems. Not only are they the simplest kind of systems, but they are also decent representatives of what we observe in the universe: some elliptical galaxies and clusters of galaxies and most globular clusters are very nearly spherical.

If we know the density profile $\rho(r)$ of a spherical system we can calculate the cumulative mass as well as the gravitational potential as a function of radius [3, p. 62]:

$$M(r) = 4\pi \int_0^r r^2 \rho(r) \mathrm{d}r \tag{3.21}$$

$$\Phi(r) = -4\pi G \left(\frac{1}{r} \int_0^r r^2 \rho(r) \mathrm{d}r + \int_r^\infty r \rho(r) \mathrm{d}r \right). \tag{3.22}$$

The total energy of the system is the sum of the potential energy and the kinetic energy:

$$E = \Phi + \frac{1}{2} v^2. \tag{3.23}$$

If the potential energy depends both on the radius and the time, we find that

$$\begin{aligned} \frac{\mathrm{d}E}{\mathrm{d}t} &= \frac{\partial E}{\partial v}\frac{\mathrm{d}v}{\mathrm{d}t} + \frac{\partial E}{\partial \Phi}\frac{\mathrm{d}\Phi}{\mathrm{d}t} \\ &= -v\nabla\Phi + \frac{\mathrm{d}\Phi}{\mathrm{d}t} \\ &= -v\nabla\Phi + \frac{\partial \Phi}{\partial t} + \frac{\partial \Phi}{\partial r}\frac{\mathrm{d}r}{\mathrm{d}t} \\ &= -v\nabla\Phi + \frac{\partial \Phi}{\partial t} + v\nabla\Phi \\ &= \frac{\partial \Phi}{\partial t}. \end{aligned} \tag{3.24}$$

We see that the total energy is function of time only if the potential energy is. Or, in other words, if the potential energy is static, then the total energy is conserved. In this case we know from the Jeans Theorem that any function of the total energy is a solution of the CBE.

The angular momentum of a particle is defined

$$\mathbf{L} = \mathbf{r} \times \mathbf{v}. \tag{3.25}$$

A collisionless particle moving in a spherical system is subject only to a radial gravitational acceleration. The time derivative of the angular momentum is therefore

$$\begin{aligned} \frac{\mathrm{d}\mathbf{L}}{\mathrm{d}t} &= \frac{\mathrm{d}}{\mathrm{d}t}(\mathbf{r} \times \mathbf{v}) \\ &= \frac{\mathrm{d}\mathbf{r}}{\mathrm{d}t} \times \frac{\mathrm{d}\mathbf{r}}{\mathrm{d}t} + \mathbf{r} \times \frac{\mathrm{d}^2\mathbf{r}}{\mathrm{d}t^2} \\ &= \mathbf{r} \times \nabla\Phi\hat{\mathbf{r}} \\ &= 0. \end{aligned} \tag{3.26}$$

The angular momentum of a spherical system is therefore conserved and any function of it is a solution to the CBE.

As we shall see in the following sections, it is convenient to define the relative potential by

$$\Psi = -\Phi, \tag{3.27}$$

and the relative energy by

$$\mathcal{E} = \Psi - \frac{1}{2}v^2. \tag{3.28}$$

3.2.4 Isotropic Models

Consider a spherical system with a potential $\Phi(r)$. We know that if the potential is static, any non-negative function of the energy is a steady-state distribution function. It turns out that, for a given spherical density distribution $\rho(r) = M\nu(r)$, there exists a unique ergodic distribution function. In this section we will derive it.

From equation 3.17 we have

$$\begin{aligned}
\nu(r) &= \int f(\mathcal{E})\mathrm{d}^3\mathbf{v} \\
&= \int_0^{2\pi}\int_0^{\pi}\int_0^{\infty} f(\Psi - \frac{1}{2}v^2)v^2\sin(\eta)\mathrm{d}v\mathrm{d}\eta\mathrm{d}\psi \\
&= 4\pi\int_0^{\infty} v^2 f(\Psi - \frac{1}{2}v^2)\mathrm{d}v \\
&= 4\pi\int_0^{\Psi} f(\mathcal{E})\sqrt{2(\Psi-\mathcal{E})}\mathrm{d}\mathcal{E}.
\end{aligned} \tag{3.29}$$

Since Ψ and ν are both monotonic functions of r, we can think of ν as a function of Ψ:

$$\frac{1}{\sqrt{8}\pi}\nu(\Psi) = 2\int_0^{\Psi} f(\mathcal{E})\sqrt{\Psi-\mathcal{E}}\mathrm{d}\mathcal{E}. \tag{3.30}$$

Differentiating both sides with respect to Ψ we obtain a so-called Abel integral equation which has the solution

$$f(\mathcal{E}) = \frac{1}{\sqrt{8}\pi^2}\left[\int_0^{\mathcal{E}} \frac{\mathrm{d}\Psi}{\sqrt{\mathcal{E}-\Psi}}\frac{\mathrm{d}^2\nu}{\mathrm{d}\Psi^2} + \frac{1}{\sqrt{E}}\left(\frac{\mathrm{d}\nu}{d\Psi}\right)_{\Psi=0}\right]. \tag{3.31}$$

Equation 3.31 is known as Eddington's Formula. It implies that, given a spherical density distribution, we can find an ergodic distribution function that generates an isotropic system with the given density [3, p. 290].

Knowing the distribution function we can now calculate the velocity distribution function at a given radius. From equation (3.19) we have

$$P_r(v)\mathrm{d}v = \frac{4\pi f(\Psi(r) - \frac{1}{2}v^2)v^2\mathrm{d}v}{\nu(r)}. \tag{3.32}$$

In figure 3.4 we plot the velocity distribution function at different radii for a Hernquist model with $r_0 = 100$kpc. They are all terminated at the velocity corresponding to the escape velocity at their radius. At small radii the velocity distribution functions have longer tails because the escape velocity is larger near the centre of the structure. Correspondingly, at large radii the velocity distribution functions have shorter tails.

3.2.5 The Osipkov-Merrit Model

In Section 2.2.3 we discussed how observations and simulations both indicate that the velocity anisotropy of a collisionless structure increases with the radius. This corresponds to a nearly ergodic distribution function in the centre and a radially biased distribution function in the outer region. We can construct such a distribution function by letting f depend on both $\mathcal{E}$ and L (which are both conserved quantities for a spherical, static structures) through the variable

$$Q = \mathcal{E} - \frac{L^2}{2r_a^2} = \frac{1}{2}v^2\left(1 + \frac{r^2}{r_a^2}\sin^2\eta\right), \tag{3.33}$$

where r_a is a constant called the anisotropy radius, and η is the angle between the velocity vector and the position vector. From equation 3.17 we have

$$\begin{aligned}
\nu(r) &= \int f(Q)\mathrm{d}^3\mathbf{v} \\
&= \int_0^{2\pi}\int_0^{\pi}\int_0^{\infty} f(Q)v^2\sin(\eta)\mathrm{d}v\mathrm{d}\eta\mathrm{d}\psi \\
&= 2\pi\int_0^{\pi}\int_0^{\Psi} f(Q)\frac{\sin(\eta)\sqrt{2(\Psi - Q)}}{\left[1 + (r/r_a)^2\sin^2(\eta)\right]^{3/2}}\mathrm{d}Q\mathrm{d}\eta \\
&\Leftrightarrow \\
\left(1 + \frac{r^2}{r_a^2}\right)\nu(r) &= 4\pi\int_0^{\Psi} f(Q)\sqrt{2(\Psi - Q)}\mathrm{d}Q.
\end{aligned} \tag{3.34}$$

This equation is identical to equation 3.29 if we replace Q by $\mathcal{E}$ and

$$\nu_Q(r) = \left(1 + \frac{r^2}{r_a^2}\right)\nu(r) \tag{3.35}$$

by $\nu(r)$. The solution is therefore

$$f(Q) = \frac{1}{\sqrt{8}\pi^2}\left[\int_0^Q \frac{\mathrm{d}\Psi}{\sqrt{Q - \Psi}}\frac{\mathrm{d}^2\nu_Q}{\mathrm{d}\Psi^2} + \frac{1}{\sqrt{Q}}\left(\frac{\mathrm{d}\nu_Q}{d\Psi}\right)_{\Psi=0}\right]. \tag{3.36}$$

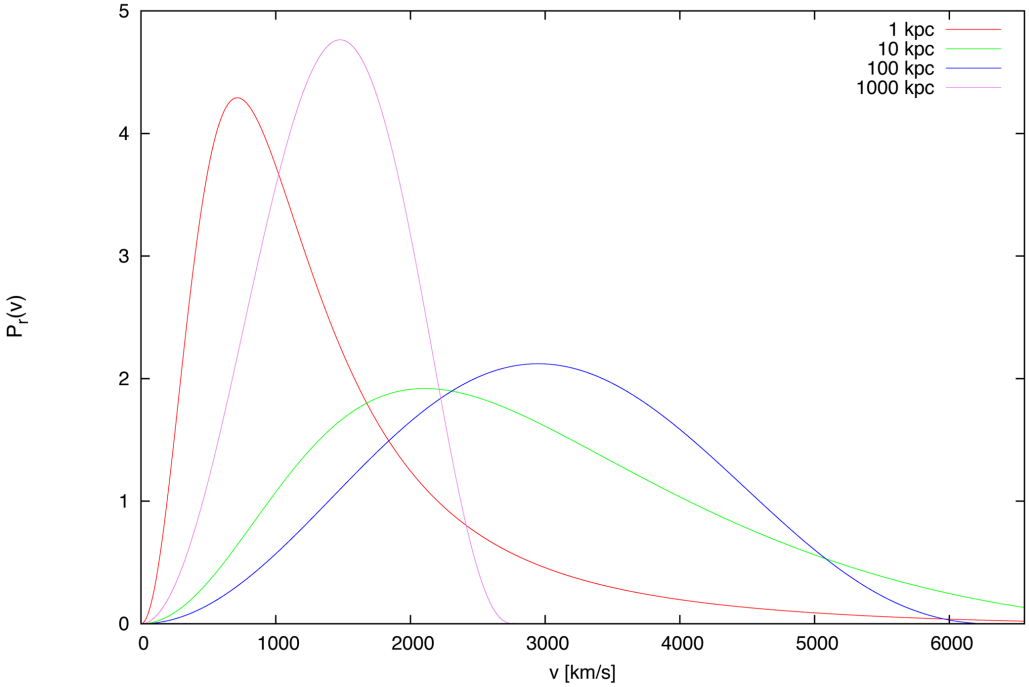

Figure 3.4: *Velocity distribution functions for an isotropic Hernquist model at different radii.*

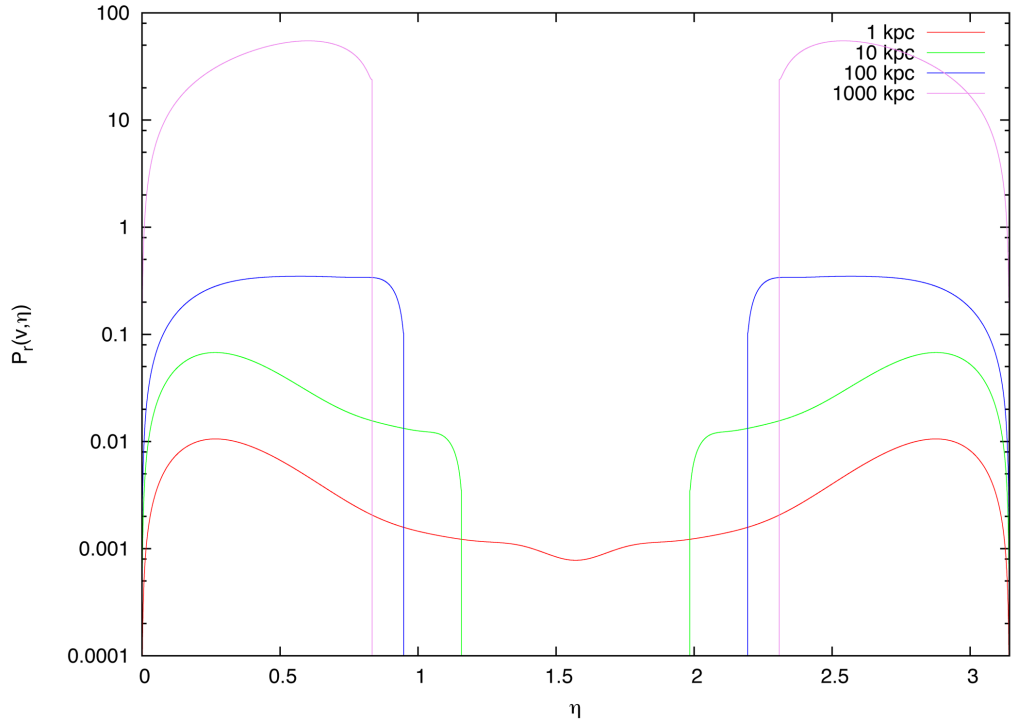

Figure 3.5: *A slice of the three-dimensional velocity distribution function for a Hernquist model with the anisotropy profile of equation (3.38). The velocity is fixed at half the escape velocity.*

A model which is described by this distribution function is called an Osipkov-Merrit model.

Knowing the distribution function we can now calculate the velocity distribution function. From equation 3.19 we have

$$P_r(v,\eta)\mathrm{d}v\mathrm{d}\eta \;=\; \frac{2\pi f(Q)v^2\mathrm{d}v\sin(\eta)\mathrm{d}\eta}{\nu(\mathbf{r})}. \tag{3.37}$$

In figure 3.5 we plot a slice of the velocity distribution function at different radii for a Hernquist model with $r_0 = 100$kpc. The anisotropy radius is $r_a = r_0$ and the velocity is fixed at half the escape velocity. Since $\eta \in [0; 2\pi[$ and only appears through $\sin(\eta)$, the velocity distribution function is symmetric about $\eta = \pi/2$. At small radii, the distribution of velocities is isotropic, and the particles move in all directions, even perpendicular to their position vector. At large radii, the velocities are radially biased, and none of them are therefore moving in tangential orbits.

The anisotropy profile of an Osipkov-Merrit model is

$$\beta(r) = \frac{1}{1 + r_a^2/r^2}. \tag{3.38}$$

It goes from zero at $r \ll r_a$ to unity at $r \gg r_a$.

3.2.6 The Jeans Equation

Finding the distribution function of a system is rarely an easy task, and it is not always necessary to know all the details that it offers. For many purposes information about simpler quantities such as the density is enough. This is where the Jeans equation comes in handy. It is obtained by multiplying the CBE with v_r and integrating over all velocities. By further assuming that the system is spherical, in equilibrium and has no bulk motion we end up with a rather simple equation, that relates the total mass of the system to its density, velocity dispersion and velocity anisotropy. The equation is known as the Jeans Equation, and in spherical coordinates it is given by

$$M(r) = -\frac{r\sigma_r^2}{G}\left(\frac{\mathrm{d}\ln(\rho)}{\mathrm{d}\ln(r)} + \frac{\mathrm{d}\ln(\sigma_r^2)}{\mathrm{d}\ln(r)} + 2\beta(r)\right). \tag{3.39}$$

The full derivation can be found in Appendix A.4.

3.3 Searching for Attractors

An attractor is a state towards which a dynamical system tends to evolve regardless of the starting conditions of the system. Points that get close enough to

the attractor remain close, even if they are slightly disturbed. Geometrically, an attractor can be a point, a curve or a more general manifold. The motivation for the existence of an attractor lies in the dissipative nature of dynamical systems. If it were not for some driving force, the motion would cease. The dissipation and the driving force tend to combine to kill out initial transients and settle the system into its typical behaviour.

We know that scattering is what makes an ideal gas evolve towards thermodynamic equilibrium. Although we can create infinitely many different structures in hydrostatic equilibrium, the thermodynamic equilibrium of a gas is always the same: a state, in which the distribution function is Maxwellian, and the entropy is maximised.

What about dark matter? It is compelling to approach the question by turning to the principle of maximum entropy. However, it turns out that the entropy of a system of collisionless particles is maximised only if the system has the distribution function of an isothermal sphere. Since the isothermal sphere has both infinite mass and energy, this is not a physical solution, and we are not any closer to finding an equilibrium state for dark matter [3, p. 377].

Many attempts to identify attractors of dark matter structures have been made throughout the years, both observationally and numerically. As mentioned, both the slope of the density and the velocity anisotropy seem to follow universal profiles. Furthermore, numerical simulations have revealed the power-law nature of the pseudo phase space density [38],

$$\frac{\rho}{\sigma^{\epsilon}} \propto r^{-\alpha}, \tag{3.40}$$

where ϵ and α are constants, the Hansen-Moore relation [15, 17],

$$\gamma \approx -5\beta - 0.75, \qquad -2.5 < \gamma < -1, \tag{3.41}$$

and the Jeans relation [13],

$$\gamma + \kappa \approx \begin{cases} -8\beta, & \beta < 0.3, \\ -0.7 - 4\beta, & 0.3 \leq \beta < 0.75, \end{cases} \tag{3.42}$$

where γ and κ are the logarithmic derivatives with respect to r of the dark matter density and radial dispersion, and β is the velocity anisotropy of the dark matter.

If there exists one or more attractors for dark matter, they must be a result of some physical mechanism(s). Two-body relaxation works on too large timescales to be relevant, but there are two other mechanisms that might explain the existence of attractors: phase mixing and violent relaxation [3, p. 379-382].

Phase mixing is a process where particles are mixed and smoothed out in phase space. As a simple example, consider a group of stars in a slice of the disk of a spiral galaxy. If we assume that their circular velocity is constant, the

time it takes a single star to complete one orbit is inversely proportional to its distance to the centre of the galaxy. After a few crossing times, the stars closer to the centre will have completed more orbits than the stars further away from the centre, and the initial group of stars will therefore be spread out. Still, for a small enough area around any star, the distribution function will remain constant.

While phase mixing leaves the energy of the particles unchanged, violent relaxation changes the potential and therefore also the energy of the particles according to equation (3.24). For collisionless particles, a time-varying potential provides a relaxation mechanism analogous to collisions in a gas. However, there is an important distinction between the two: while collisional relaxation establishes and equipartition of energy, violent relaxation establishes an equipartition of energy per mass.

Having considered gas and dark matter separately, we will now examine how the two affect each other. Looking at the equation of hydrostatic equilibrium (3.8) and the Jeans equation (3.39) we see that they are very similar. Ignoring the velocity anisotropy in the Jeans equation, the equations can be matched term by term, suggesting that the radial velocity dispersion of the dark matter might be related to a pseudo dark matter temperature, pseudo, because the word *temperature* implicitly refers to Gaussian velocity distributions. We could define such a temperature by

$$\frac{T_{DM} k_B}{\mu m_u} = \frac{1}{3}(\sigma_r^2 + \sigma_\phi^2 + \sigma_\theta^2). \tag{3.43}$$

There is no fundamental reason why the temperature of the gas should be identical to the dark matter temperature (the dark matter only gives rise to an upper limit to the gas temperature). We will, however, consider the ratio between the gas temperature and the temperature derived from the dark matter dispersions, namely

$$\Gamma = \frac{T_g}{T_{DM}} = \frac{T_g k_B}{\mu m_u} \frac{3}{\sigma_r^2 + \sigma_\phi^2 + \sigma_\theta^2}. \tag{3.44}$$

Adiabatic merger simulations and cosmological simulations of galaxies with radiation and star formation have shown that $\Gamma \approx 1$ [14, 42].

We learned earlier that the Jeans equation, because of its many variables, is very difficult, if not impossible, to solve analytically. Observationally, the Jeans equation also poses problems, as several of its variables are difficult to observe. The identification of one or more attractors could give us the means to reduce the Jeans equation to fewer variables, thereby making it easier to work with both analytically and observationally.

Consider a dwarf galaxy. We can observe its stars to find the stellar density and stellar line-of-sight velocity dispersion. Plugging these into the Jeans

equation along with an *assumed* velocity anisotropy profile, we can calculate the total mass of the system and thereby estimate how much dark matter there is. But if the assumed velocity anisotropy profile is incorrect, the total mass will be incorrect too. This problem is known as the mass velocity anisotropy degeneracy. However, if the stars in the dwarf galaxy follow the Jeans relation, we can completely eliminate the velocity anisotropy from the Jeans equation and thus solve the problem. This is described in further detail in Section 10.1.

4 GADGET-2

We use the cosmological simulation code GADGET-2 to evolve the structures [32]. It is written and maintained by Volker Springel and it is both fast and well tested.

GADGET-2 simulates fluid flows by means of smoothed particle hydrodynamics and computes gravitational forces with a hierarchical tree algorithm. As a time integrator the code uses a variant of leapfrog integration. In the following we will take a closer look at the ideas behind these methods. We will also briefly discuss the method used to simulate cooling and star formation.

4.1 Smoothed Particle Hydrodynamics

The smoothed particle hydrodynamics (SPH) method uses a set of discrete elements, so-called tracer particles, to describe the state of a fluid. The particles have a spatial distance called the smoothing length, over which their properties are smoothed by a kernel function. This means that their physical quantities can be obtained by summing the relevant properties of all the particles that lie within the range of the kernel.

GADGET-2 estimates the density of a particle by

$$\rho_i = \sum_{j=1}^{N} m_j W(|\mathbf{r}_{ij}|, h^i_{\text{sph}}), \tag{4.1}$$

where m is the mass of a particle, $\mathbf{r}$ is the separation vector, h_{sph} is the SPH smoothing length and $W(r, h_{\text{sph}})$ is the Monaghan-Lattanzio spline kernel [23] given by

$$W(r, h_{\text{sph}}) = \frac{8}{\pi h^3_{\text{sph}}} \begin{cases} 1 - 6\left(\frac{r}{h_{\text{sph}}}\right)^2 + 6\left(\frac{r}{h_{\text{sph}}}\right)^3, & 0 \leq \frac{r}{h_{\text{sph}}} \leq \frac{1}{2}, \\ 2\left(1 - \frac{r}{h_{\text{sph}}}\right)^3, & \frac{1}{2} < \frac{r}{h_{\text{sph}}} \leq 1, \\ 0, & \frac{r}{h_{\text{sph}}} > 1. \end{cases} \tag{4.2}$$

The kernel function weighs the contributions of each neighbouring particle according to their distance from the particle of interest and to their density. Note that the kernel function is exactly zero for particles further away than one smoothing length. This has the advantage of saving computational work by not including the relatively minor contributions from distant particles.

The smoothing length is defined such that the kernel volume for a particle contains a constant mass for the estimated density:

$$\frac{3}{4}\pi (h_{\text{sph}})^3 = N_{\text{sph}} \overline{m}, \tag{4.3}$$

where N_{sph} is the typical number of smoothing neighbours and $\overline{m}$ is the average particle mass. The equation can be solved using the Newton-Raphson method [27, 355-362]. By giving each particle its own time dependent smoothing length, the resolution of a simulation can automatically adapt itself depending on local conditions. For example, in a very dense region the smoothing length can be made relatively short, yielding high spatial resolution. Conversely, in low-density regions where the resolution is low, the smoothing length can be increased, thereby optimising the computation time for the regions of interest.

The GADGET-2 implementation of SPH uses the entropy as an independent variable. It has been shown to give more accurate results than most other implementations that use the thermal energy as a variable [33]. The entropy is defined by

$$A = P/\rho^{\gamma} = (\gamma - 1)\rho^{1-\gamma}u, \tag{4.4}$$

where P is the pressure, γ is the adiabatic index and u is the specific energy. The last equation follows from the ideal gas law. Starting from a discretised version of the fluid Lagrangian, it can be shown that the acceleration of a particle is given by [33]

$$\begin{aligned}\frac{\mathrm{d}\mathbf{v}_i}{\mathrm{d}t} = -\sum_{j=1}^{N} m_j \Bigg[& f_i \frac{P_i}{\rho_i^2}\nabla_i W_{ij}(h^i_{\text{sph}}) + f_j \frac{P_j}{\rho_j^2}\nabla_i W_{ij}(h^j_{\text{sph}}) \\ & + \frac{1}{2}\Pi_{ij}\nabla_i \left(W_{ij}(h^i_{\text{sph}}) + W_{ij}(h^j_{\text{sph}})\right)\Bigg],\end{aligned} \tag{4.5}$$

where

$$W_{ij}(h_{\text{sph}}) = W(|\mathbf{r}_i - \mathbf{r}_j|, h), \tag{4.6}$$

and

$$f_i = \left[1 + \frac{h^i_{\text{sph}}}{3\rho_i}\frac{\partial \rho_i}{\partial h^i_{\text{sph}}}\right]^{-1}. \tag{4.7}$$

The last term is included to generate an artificial viscosity which takes the form

$$\Pi_{ij} = -\frac{\alpha_{\text{visc}}}{2}\frac{(c_i + c_j - 3w_{ij})\, w_{ij}}{\rho_{ij}}, \tag{4.8}$$

where

$$w_{ij} = \begin{cases} \mathbf{v}_{ij} \cdot \frac{\mathbf{r}_{ij}}{|\mathbf{r}_{ij}|}, & \mathbf{v}_{ij} \cdot \mathbf{r}_{ij} < 0, \\ 0, & \text{otherwise} \end{cases} \tag{4.9}$$

and $c_i = \sqrt{\gamma P_i/\rho_i}$ is the speed of sound. Here $\Pi_{ij} \geq 0$ is non-zero only when particles approach each other. The parameter α_{visc} determines the strength of the viscosity, and its value typically lies in the range $0.5 - 1.0$. The need for an artificial viscosity arises because flows of ideal gases easily develop discontinuities. Such shocks can be captured by an artificial viscosity.

4.2 Tree Code

A collisionless code attempts to mimic the evolution of a system that contains infinitely many particles. Consequently, the system's density distribution is to be thought of as a continuum that is sampled with a finite number N of tracer particles [32]. Since GADGET-2 uses particles to represent both the collisionless dark matter and the gaseous fluid, it is possible to compute the self-gravity of both components with gravitational N-body methods.

The basic concept of N-body simulations is actually very simple. From the current positions of the particles in a structure we can derive the force on each particle, and then use it to advance the position and momentum of each particle for a short time. This process can be repeated as many times as needed. However, producing a code that can efficiently do this for a large number of particles is a major challenge.

A straightforward approach is to calculate the gravitational force on a single particle by summing the contributions from all the other particles in the system. Each force evaluation involves the calculation of $N - 1$ distances, and the work per time step will therefore increase as $O(N^2)$. For simulations involving a large amount of particles, this method is therefore not an attractive strategy. Fortunately there exists more efficient methods.

GADGET-2 uses a tree code that was introduced by Barnes and Hut in 1986 [2]. The idea behind the method is to group nearby particles together in a hierarchy of cubes. If a group is sufficiently far away, its gravitational effects can be calculated using its centre of mass. This reduces the number of force calculations per time step to $O(N \log N)$ for a uniform distribution.

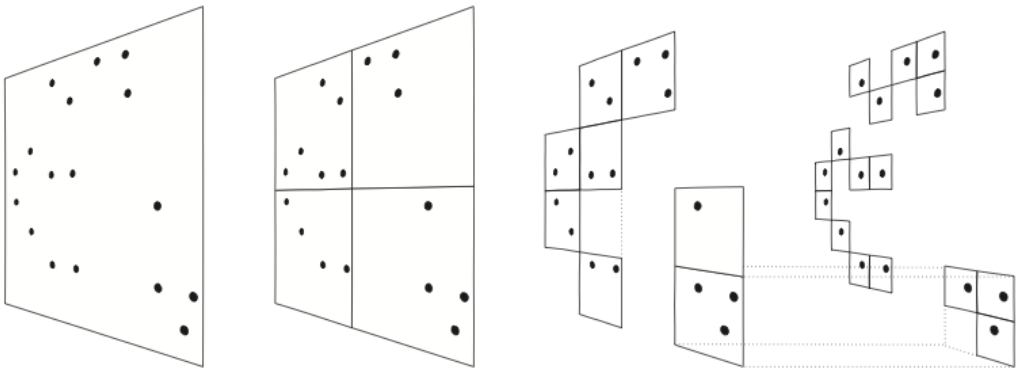

Figure 4.1: *A two-dimensional illustration of the Barnes and Hut oct-tree [35].*

To begin with the algorithm places a cube around all the particles in a system and calculates its centre of mass. It then recursively divides this cube into eight subcubes, calculating the centre of mass for each of them, until each cube contains 0 or 1 particles. This hierarchy of cubes forms an oct-tree, and the original cube

is called the root of the tree, while each group of eight subcubes are called nodes. To calculate the force on a particle, the algorithm traverses the nodes of the tree starting from the root. To determine if a node is sufficiently far away from a particle, the algorithm evaluates the inequality

$$\frac{GM}{r^2}\left(\frac{l}{r}\right)^2 \leq \alpha|\mathbf{a}|, \tag{4.10}$$

where M and l are the mass and size of the node, respectively, r is the distance, α is a fixed tolerance parameter that typically lies in the range $0.5 - 1$, and $\mathbf{a}$ is the total acceleration obtained in the last time step. If the inequality is true, the force is calculated by approximating the particles contained in the cube as a single body, whose position is the body's centre of mass, and whose mass is the body's total mass. If the inequality is false, the algorithm recursively traverses each of the node's subtrees [18].

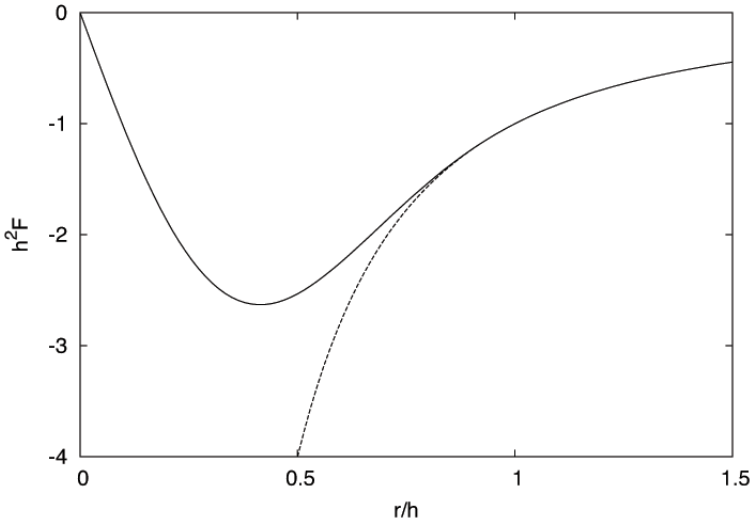

Figure 4.2: *Comparison of the softened force law of equation (4.13) (solid) with Newton's law (dashed). Here $G = M = 1$.*

GADGET-2 uses a monopole expansion to estimate the gravitational potential acting on a particle due to a (distant) group of particles. If r is the distance from the particle to the centre of mass of the group and M is the total mass of the group, the potential is

$$\Phi(r) = \frac{GM}{h} W_2\left(\frac{r}{h}\right), \tag{4.11}$$

where

$$W_2(u) = \begin{cases} \frac{16}{3}u^2 - \frac{48}{5}u^4 + \frac{32}{5}u^5 - \frac{14}{5}, & 0 \leq u \leq \frac{1}{2}, \\ \frac{1}{15u} + \frac{32}{3}u^2 - 16u^3 + \frac{48}{5}u^4 - \frac{32}{15}u^5 - \frac{16}{5}, & \frac{1}{2} < u \leq 1, \\ -\frac{1}{u}, & u > 1 \end{cases} \tag{4.12}$$

is the gravitational softening kernel, and h is the gravitational softening length [35]. If there is only one particle in the group, equation (4.11) is exact for $r > h$. The gravitational force on the particle is

$$\mathbf{F}(\mathbf{r}) = -\nabla\Phi = -\frac{GM}{h^2} W_2'\left(\frac{r}{h}\right)\frac{\mathbf{r}}{r}. \tag{4.13}$$

The gravitational softening is included to prevent the force from diverging when two particles approach each other closely. Apart from the chance of numerical overflow, it is an entirely unphysical behaviour, since we are simulating a continuum. Equation (4.13) tends to the Newtonian force for distances bigger than the gravitational softening length, and tends smoothly to zero for small distances. To find the total gravitational force on a particle, the contribution from each group of particles in the system is summed.

GADGET-2's tree code is both fast and precise. Because it does not employ any grid, it can handle problems such as galaxy mergers, in which dense stellar systems move through a large volume of nearly empty space. It can also easily be parallelized by, for example, assigning the construction of each of the root's eight subcubes' trees to a different processor. Still, for very dense regions the complexity of the code will approach $O(N^2)$ as each node will have to be traversed.

4.3 Leapfrog Time Integrator

A time integrator advances the position and momentum of the particles forward in time. Leapfrog integration is a simple second order method which calculates positions and velocities at interleaved time points, interleaved in such a way that they 'leapfrog' over each other.

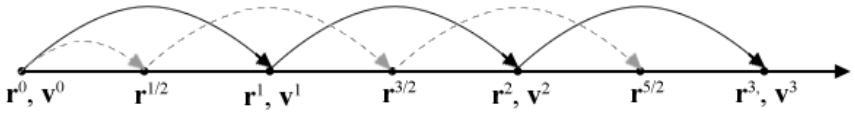

Figure 4.3: *Illustration of the leapfrog method for a single particle using a constant time step.*

The time integration for collisionless particles proceeds as follows. Starting at $t = t_0$, the position $\mathbf{r}^0$ and velocity $\mathbf{v}^0$ of a particle are given as initial conditions. Choosing a small time step Δt the particle position at $t = t_0 + \frac{1}{2}\Delta t$ is predicted according to

$$\mathbf{r}^{1/2} = \mathbf{r}^0 + \mathbf{v}^0 \cdot \frac{1}{2}\Delta t. \tag{4.14}$$

The acceleration $\mathbf{a}^{1/2}$ at $t = t_0 + \frac{1}{2}\Delta\mathrm{t}$ of the particle is then calculated using the tree code discussed above. The position and velocity of the particle at $t = t_0 + \Delta t$

can now be calculated by

$$\mathbf{v}^1 = \mathbf{v}^0 + \mathbf{a}^{1/2} \cdot \Delta t, \tag{4.15}$$

$$\mathbf{r}^1 = \mathbf{r}^0 + \frac{1}{2}\left(\mathbf{v}^0 + \mathbf{v}^1\right) \cdot \Delta t. \tag{4.16}$$

This process can be repeated as many times as needed [35].

The time integration scheme for collisional particles follows the same concept, but it also involves integrating the entropy equation, and the particle accelerations also receive a hydrodynamical component.

Cosmological structures embrace a large dynamic range of timescales. In high-density regions such as in the centres of galaxies, orders of magnitude smaller time steps are required than in low-density regions such as the intracluster medium. Evolving all particles with the smallest required time step is therefore a considerable waste of computational resources. Using individual time steps handles this situation more efficiently. The principal idea is to compute forces only for a certain group of particles in a given advancement, with the other particles being evolved on larger time steps thereby being progressed more rarely.

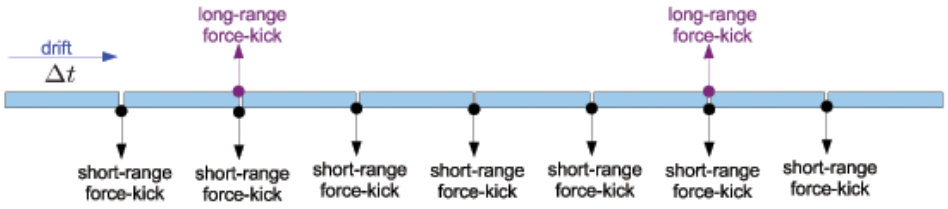

Figure 4.4: *Illustration of the short- and long-range time stepping used by GADGET-2. The code evolves the position of the particles in the system to the next time when a force computation is required. This is called drifting. At that time changes of the particle momenta are applied based on short-range or long-range forces, or on both [32].*

For collisionless particles, there are several possible time step criterions to choose from. GADGET-2 uses a combination of two criterions, setting the time step equal to the minimum of the two time steps

$$\Delta t_1 = \alpha_{\mathrm{tol}} \frac{\sigma}{|\mathbf{a}|}, \tag{4.17}$$

$$\Delta t_2 = \alpha'_{\mathrm{tol}} \frac{3}{\sqrt{8\pi G\rho}}. \tag{4.18}$$

Here σ is the square root of the typical velocity dispersion of the particles, and the tolerance parameters are related by $\alpha_{\mathrm{tol}} \simeq 3\alpha'_{\mathrm{tol}}$. The criterion in equation (4.17) can lead to small secular effects in high-density regions. The criterion in equation (4.18) does better in this respect, but it does not work well in regions of very low density. But the combination of the two provides good integration

accuracy in low density environments and simultaneously does well in the central regions of large haloes.

For collisional particles, the time step criterion needs to be supplemented by the Courant condition. It requires that the time interval must not be greater than that required for a sound wave to cross a spatial cell and is given by

$$\Delta t_3 = \frac{\alpha_{\mathrm{cour}} h_{\mathrm{sph}}}{h_{\mathrm{sph}}|(\nabla \cdot \mathbf{v})| + \max(c_s, |\mathbf{v}|)(1 + 0.6\alpha_{\mathrm{visc}})}, \tag{4.19}$$

where α_{cour} is an accuracy parameter, the Courant factor. The time step of collisional particles is then equal to the minimum of the three time steps in equations (4.17-4.19).

Newton's equations of motion are symplectic in nature; they preserve phase space areas. For the regions spanned by the four particles in figure 4.5 this means that

$$\mathrm{d}A = \mathrm{d}A'. \tag{4.20}$$

Since this property is an exact feature of Newton's equations, it is desirable that

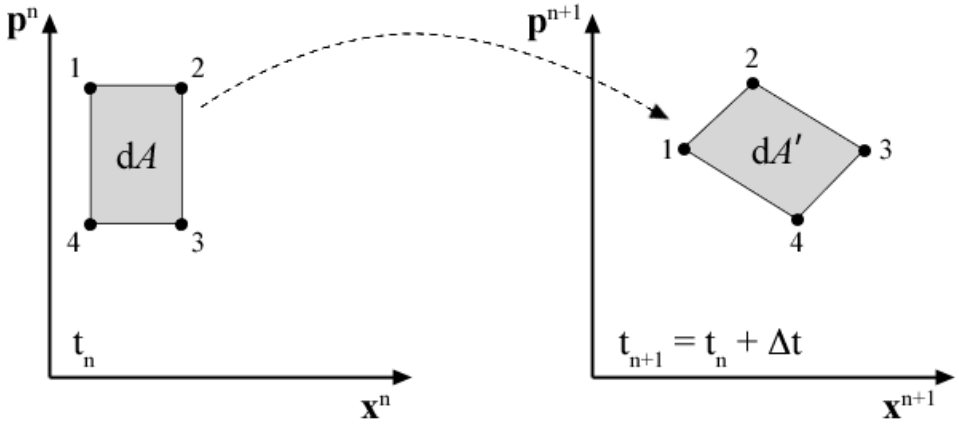

Figure 4.5: *Illustration of the symplectic nature of Newton's equations.*

the simulation code possesses it as well. While the leapfrog method for constant time steps is symplectic, the same is not true for individual time steps. Still, the evolution can be expected to reach an accuracy comparable to a symplectic integration. This quasi-symplectic nature of GADGET-2's integration scheme possesses a sort of global stability that makes it superior to non-symplectic integrators such as the second order Runge-Kutta method. Although the leapfrog method and the second order Runge-Kutta method produce comparable errors in a single step, the Runge-Kutta method displays a large drift in orbital energy over time, while the leapfrog method is much more stable [32].

4.4 Additional Physics

We use a semi-analytic galaxy formation model to simulate gas cooling, star formation and feedback [29, 30, 34]. In this model, a gas particle is treated as a two-phase medium, comprised of condensed clouds in pressure equilibrium with an ambient hot gas. The clouds supply the material available for star formation.

In the following, $\rho_{\rm h}$ denotes the density of the hot ambient gas, $\rho_{\rm c}$ is the density of cold clouds, ρ_* the density of stars, and $\rho = \rho_{\rm h} + \rho_{\rm c}$ is the total gas density. Furthermore, the average thermal energy per unit volume of the gas can be written as $\epsilon = \rho_{\rm h} u_{\rm h} + \rho_{\rm c} u_{\rm c}$, where $u_{\rm h}$ and $u_{\rm c}$ are the energy per unit mass of the hot and cold components, respectively.

Three basic processes are responsible for mass exchange between the hot gas, the cold gas and the stars: cloud growth caused by radiative cooling, star formation and cloud evaporation arising from supernovae. These processes are only active when the density exceeds a threshold, namely $\rho_g > \rho_{\rm th}$, otherwise only ordinary cooling is active.

4.4.1 Cooling

The model computes the cooling time using the equation

$$t_{\rm cool} = \frac{3}{2} \frac{\langle m_g \rangle k_B T_{\rm h}}{\rho_g(r) \Lambda(T_{\rm h}, Z_{\rm h})}, \tag{4.21}$$

where the cooling function depends on the temperature and metallicity of the hot gas. Assuming that the gas density profile is described by that of a singular isothermal sphere,

$$\rho_{\rm h}(r) = \frac{M_{\rm h}}{4\pi r_{\rm vir} r^2}, \tag{4.22}$$

where $M_{\rm h}$ is the total mass of the hot gas, we can solve the equation for the cooling radius $r_{\rm cool}$:

$$r_{\rm cool} = \sqrt{\frac{t_{\rm cool} M_{\rm h} \Lambda(T_{\rm h}, Z_{\rm h})}{6\pi \langle m_g \rangle k_B T_{\rm h} r_{\rm vir}}}. \tag{4.23}$$

This is the radius within which all of the gas can cool within a time $t_{\rm cool}$. Writing the expression for the mass within $r_{\rm cool}$ and differentiating, we obtain the rate at which the gas can cool:

$$\frac{{\rm d}m_{\rm c}}{{\rm d}t} = \frac{M_{\rm h}}{2t_{\rm cool}} \frac{r_{\rm cool}}{r_{\rm vir}}. \tag{4.24}$$

4.4.2 Star Formation and Feedback

The model assumes that (quiescent) star formation converts cold clouds into stars on a characteristic timescale t_*,

$$t_*(\rho) = t_*^0 \left(\frac{\rho}{\rho_{\rm th}} \right)^{-1/2}, \tag{4.25}$$

and that a mass fraction β of these stars are short-lived and instantly die as supernovae. This can be described by

$$\frac{\mathrm{d}\rho_*}{\mathrm{d}t} = (1-\beta)\frac{\rho_\mathrm{c}}{t_*}. \tag{4.26}$$

Star formation therefore depletes the reservoir of cold clouds at the rate ρ_c/t_* and leads to an increase of the hot gas as $\beta\rho_c/t_*$, as we assume that ejecta from supernovae are returned as hot gas. The parameter β is the mass fraction of massive stars ($> 8M_\odot$) formed for each initial population of stars, and it therefore depends on the adopted stellar initial mass function (IMF). This model assumes a universal Chabrier IMF [7].

In addition to returning gas to the hot gas of the ICM, supernovae also release energy. The precise amount of this energy depends on the IMF. If the average energy returned per formed solar mass is ϵ_SN, the average heating rate is

$$\frac{\mathrm{d}}{\mathrm{d}t}(\rho_h u_h)\Big|_\mathrm{SN} = \epsilon_\mathrm{SN}\frac{\mathrm{d}\rho_*}{\mathrm{d}t} = \beta u_\mathrm{SN}\frac{\rho_c}{t_*}, \tag{4.27}$$

where $u_\mathrm{SN} = (1-\beta)\beta^{-1}\epsilon_\mathrm{SN}$ can be expressed in terms of an equivalent supernova temperature

$$T_\mathrm{SN} = \frac{2\mu}{3k_B}(1-\beta)\beta^{-1}\epsilon_\mathrm{SN}. \tag{4.28}$$

The mass of the hot ambient gas is not only increased by exploding stars, but also by cloud evaporation. When cold clouds are evaporated inside hot bubbles of supernovae, material is moved from the cold clouds to the hot gas. The total mass of clouds that are evaporated is assumed to be proportional to the mass in supernovae,

$$\left(\frac{\mathrm{d}\rho_c}{\mathrm{d}t}\right)_\mathrm{EV} = A\beta\frac{\rho_c}{t_*}, \tag{4.29}$$

where the efficiency A of the evaporation process is expected to be a function of the local environment. For simplicity, the code only takes the expected theoretical dependence on density,

$$A = A_0\left(\frac{\rho}{\rho_\mathrm{th}}\right)^{-4/5}, \tag{4.30}$$

into account [22].

5 Creating a Structure

In this section we will describe how we create different structures in equilibrium using the equations that we discussed in Section 3.

5.1 Structures

The dimensions of our structures are chosen to resemble those of a large galaxy cluster such as the Perseus Cluster. Each cluster has a maximum radius of 10Mpc and a total mass of $10^{15}\mathrm{M}_{\odot}$ of which 10% is gas and 90% is dark matter.

To obtain a wide range of initial conditions, we create 10 different structures. Their gas density profiles all follow the general profile from equation (2.2), with the following parameters:

$$\begin{aligned} r_0 &= 100 \text{ kpc}, \\ r_1 &= 1000 \text{ kpc}, \\ \alpha &= 0.8, \\ \delta &= 1, \\ \beta &= 2/3. \end{aligned}$$

The dark matter density profiles follow the general profile from equation (2.3). They all have $r_0 = 100$kpc, but the values of α and δ vary. So does the velocity anisotropy profile. The various combinations are presented in table 5.1.

Structure	α	δ	β
S1a	1	4	0
S1b	1	4	$1/(1+(r_0/r)^2)$
S1c	1	4	$1/(1+(2r_0/r)^2)$
S2a	0	5	0
S2b	0	5	$1/(1+(r_0/r)^2)$
S3a	2	6	0
S3b	2	6	$1/(1+(r_0/r)^2)$
S4a	0	3.5	0
S4b	0	3.5	$1/(1+(r_0/r)^2)$
S5a	1	4	0

Table 5.1: *The various combinations of the dark matter density profile and velocity anisotropy.*

We create two sets of the structures, one with 1 million particles and one with 100,000 particles. For both sets, 10% of the particles represent the gas, while the rest represent dark matter. The mass of the gas particles and dark matter particles are thus the same in both sets, namely $10^9\mathrm{M}_{\odot}$ and $10^{10}\mathrm{M}_{\odot}$, respectively.

5.2 Method

A dark matter particle is described by its position, velocity and mass, while a gas particle is described by its position, internal energy and mass. GADGET-2 also accepts extra input variables such as the potential and density of a particle, but this is not necessary to provide, since these properties can be calculated from the particles' positions and masses. Below we describe how we assign to each particle in the structure its position and velocity or internal energy.

5.2.1 Position

GADGET-2 requires the position of a particle in Cartesian coordinates. Because of the spherical nature of our structures, we will therefore first calculate the position of each particle in spherical coordinates and then convert it to Cartesian coordinates. In spherical coordinates a particle's position is described by its distance to the structure's centre and its direction via the numbers r, θ and ϕ.

To distribute a number of particles according to a density profile $\rho(r)$ we first calculate their cumulative mass function $M(r)$ using equation (3.21). Assuming that each particle has the same mass we can then find the radius of a particle by generating a uniformly distributed number $u \in [0; M[$, where M is the total mass of the particles, and by solving the equation $M(r) = u$ numerically for r.

Choosing θ and ϕ according to

$$\theta = \arccos(1 - 2u_1), \tag{5.1}$$
$$\phi = 2\pi u_2, \tag{5.2}$$

where u_1 and u_2 are uniformly distributed numbers $u_1, u_2 \in [0; 1[$, we get an isotropic particle distribution (see a proof of this in Appendix A.5).

Finally, we convert the spherical coordinates to Cartesian coordinates using the equations

$$x = r\sin(\theta)\cos(\phi), \tag{5.3}$$
$$y = r\sin(\theta)\sin(\phi), \tag{5.4}$$
$$z = r\cos(\theta). \tag{5.5}$$

5.2.2 Velocity

GADGET-2 requires the velocity of a particle in Cartesian coordinates. We will first calculate the velocity of a particle using the coordinates v, η and ψ, where v is the length of the velocity vector, η is the angle between the position vector and the velocity vector, and ψ is the rotation of the velocity vector around the position vector. We then convert this to spherical coordinates v_r, v_θ and v_ϕ, where the unit vectors depend on the position of the particle, and then Cartesian coordinates.

The velocities of the particles are sampled from velocity distributions whose shapes depend on both the density distribution and the velocity anisotropy profile of the structure. For an isotropic structure we can calculate the 1-dimensional speed distribution function from equation (3.32). We can then use the accept-reject method to find the speed of each particle in three steps:

1. We generate a uniformly distributed number $u_1 \in [0; P_{\max}[$, where $P_{\max}$ is the maximum of the speed distribution function.

2. We generate another uniformly distributed number $u_2 \in [0; \sqrt{2\Psi}[$, where $\sqrt{2\Psi}$ is the escape velocity.

3. We check if $P(u_2) \leq u_1$. If this is the case, we give the particle speed $v = u_2$, if not we repeat steps 1 and 2 until it is.

We can find the particle's direction of velocity using the same method as in equations (5.1-5.2), with $\eta = \theta$ and $\psi = \phi$.

For a structure with a velocity anisotropy profile that follows the Osipkov-Merrit model, we can use equation (3.37) to calculate the 2-dimensional velocity distribution function. We can then use the accept-reject method to find the speed and the angle η of each particle in four steps:

1. We generate a uniformly distributed number $u_1 \in [0; P_{\max}[$, where $P_{\max}$ is the maximum of the velocity distribution function.

2. We generate a second uniformly distributed number $u_2 \in [0; \sqrt{2\Psi}[$.

3. We generate a third uniformly distributed number $u_3 \in [0; \pi[$.

4. We check if $P(u_2, u_3) \leq u_1$. If this is the case, we give the particle speed $v = u_2$ and angle $\eta = u_3$, if not we repeat steps 1-3 until it is.

The last component of the velocity is found by generating a uniformly distributed number $\psi \in [0; 2\pi[$.

Knowing the velocity of a particle in coordinates (v, η, ψ), we first convert them to spherical coordinates using the equations

$$v_r = v\cos(\eta), \tag{5.6}$$
$$v_\theta = v\sin(\eta)\cos(\psi), \tag{5.7}$$
$$v_\phi = v\sin(\eta)\sin(\psi), \tag{5.8}$$

and then to Cartesian coordinates using the equations

$$v_x = v_r\sin(\theta)\cos(\phi) + v_\theta\cos(\theta)\cos(\phi) - v_\phi\sin(\phi), \tag{5.9}$$
$$v_y = v_\theta\sin(\theta)\sin(\phi) + v_\theta\cos(\theta)\sin(\phi) + v_\phi\cos(\phi), \tag{5.10}$$
$$v_z = v_\phi\cos(\theta) - v_\theta\sin(\theta). \tag{5.11}$$

5.2.3 Internal Energy

A gas particle of mass M can be thought of as representing $N = M/\langle m_g \rangle$ real gas particles, and we can therefore describe its internal energy by equation (3.10). GADGET-2 requires the internal energy per unit mass as input variable. It is given by

$$\begin{aligned} u &= \frac{U}{M} \\ &= \frac{3}{2}\frac{N k_B T_g}{N\langle m_g \rangle} \\ &= \frac{3}{2} k_B \frac{T_g}{\langle m_g \rangle}. \end{aligned} \tag{5.12}$$

Using equation (3.9) with $\mu = 0.6$, we first calculate the temperature of each particle and then the internal energy per unit mass. For S5a alone, we give each particle the same internal energy, namely the average of the correct internal energy of all the particles.

5.3 Code Optimisation

Equation (3.31) involves the evaluation of the differential $\mathrm{d}^2\rho/\mathrm{d}\Psi^2$. Because $\rho(\Psi)$ is very steep in the inner region of the structure, numerical differentiation results in numerical overflow. To avoid the problem and to speed up the program, we therefore evaluate the differential analytically. The chain rule allows us to rewrite the differential as

$$\frac{\mathrm{d}^2\rho}{\mathrm{d}\Psi^2} = \frac{1}{(\mathrm{d}\Psi/\mathrm{d}r)^2}\left[\frac{\mathrm{d}^2\rho}{\mathrm{d}r^2} - \frac{\mathrm{d}\rho}{\mathrm{d}r}\frac{1}{\mathrm{d}\Psi/\mathrm{d}r}\frac{\mathrm{d}^2\Psi}{\mathrm{d}r^2}\right]. \tag{5.13}$$

We can then use that

$$\frac{\mathrm{d}\Psi}{\mathrm{d}r} = -\frac{GM(r)}{r^2}, \tag{5.14}$$

$$\frac{\mathrm{d}^2\Psi}{\mathrm{d}r^2} = \frac{2GM(r)}{r^3} - 4\pi G\rho(r). \tag{5.15}$$

In the code, the analytical values of $\mathrm{d}\rho/\mathrm{d}r$ and $\mathrm{d}^2\rho/\mathrm{d}r^2$ are used to avoid any numerical differentiation during the calculation of $\mathrm{d}^2\rho/\mathrm{d}\Psi^2$. This increases the speed of the program significantly. The differential in equation (3.36) is calculated correspondingly.

Looking at equation (3.31) we see that $f(\mathcal{E})$ diverges for $\Psi \approx \mathcal{E}$. Substituting

$$u = \arctan\left(\frac{1}{\sqrt{\mathcal{E} - \Psi}}\right), \tag{5.16}$$

the integral can be written

$$\int_0^{\mathcal{E}} \frac{\mathrm{d}\Psi}{\sqrt{\mathcal{E}-\Psi}} \frac{\mathrm{d}^2\rho}{\mathrm{d}\Phi^2} = \int_{\arctan\left(1/\sqrt{\mathcal{E}}\right)}^{\pi/2} \frac{2\mathrm{d}u}{\sin^2 u} \frac{\mathrm{d}^2\rho}{\mathrm{d}\Psi^2}. \tag{5.17}$$

With this transformation the integrand is much more well-behaved, and the number of calculations needed to do the integration accurately is reduced by an order of magnitude. The corresponding transformation is performed in equation (3.36).

6 Simulation Parameters

6.1 Units

We use $10^{10}M_{\odot}$, kpc and km/s as units for mass, length and velocity. The time unit is

$$t_u = \frac{\text{kpc}}{\text{km/s}} = 9.8 \cdot 10^8 \text{ yr}. \tag{6.1}$$

In these units the gravitational constant is

$$G = 43007.1 \text{ kpc}(\text{km/s})^2(10^{10}M_{\odot})^{-1}, \tag{6.2}$$

and the Boltzmann constant is

$$k_B = 4.4 \cdot 10^{-45} \text{ (km/s)}^2 10^{10} M_{\odot}\text{K}^{-1}. \tag{6.3}$$

6.2 Dynamical Time

The dynamical time of a structure is

$$t_{\text{dyn}} \approx (G\overline{\rho})^{-1/2}, \tag{6.4}$$

where $\overline{\rho}$ is the total average density of the structure. This is the time it takes for a particle to complete a significant fraction of its orbit or, in other words, the time it takes the structure to approach equilibrium [3, p. 64]. Letting a structure run for $1.5t_u$ will result in the equilibrium radii presented in table 6.1. The majority of the particles in a structure are within its equilibrium radius, so most of the structure is in equilibrium.

Structure	r_{eq}[Mpc]	N
S1a, S1b, S1c	1.26	87%
S2a, S2b	1.315	96%
S3a, S3b	1.32	99%
S4a, S4b	1.13	63%
S5a	1.26	87%

Table 6.1: *The equilibrium radii of the structures after a run time of* $1.5t_u$*, and the approximate percentage of particles within this radius.*

6.3 Gravitational Softening Length

The size of the gravitational softening length introduced in Section 4.2 is directly related to how tightly the particles are bound. A relatively large gravitational softening length will bind the particles less tightly, and as a consequence, the

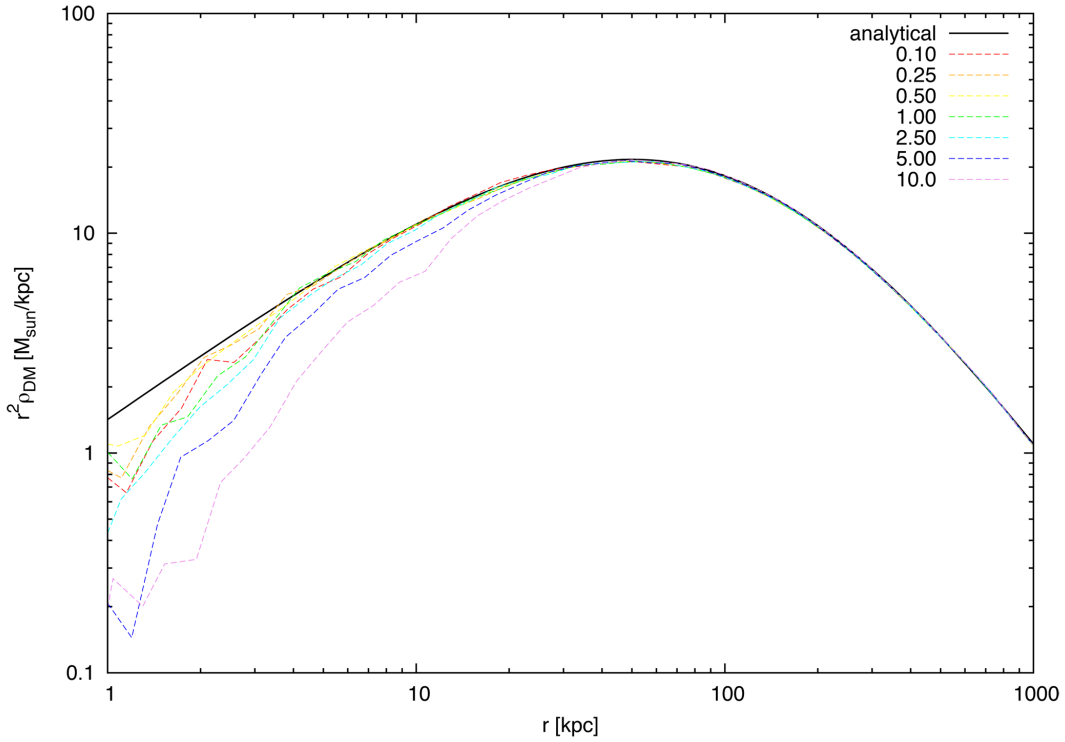

Figure 6.1: *The dark matter density profile of S1a after the structure has been evolved for* $1.5t_u$ *using various softenings.*

density profile will be more shallow in the inner region. This is illustrated in figure 6.1 where we have plotted the dark matter density profile of S1a after the structure has been evolved for $1.5t_u$ using various softenings.

As a rule of thumb we cannot trust any distances shorter than about three times the gravitational softening length, so the use of gravitational softening gives rise to a measure of resolution. For our analysis we would like to look at radii $r > 5$ kpc so $h > 5/3$ is too large. The smallest gravitational softening length possible would appear to be the most favourable, but we also need to take into account that the smaller a value we use, the longer it takes to run a simulation (see table 6.2). We therefore choose a softening of $h = 0.5$ since this is a good compromise between resolution and computing time. This gives us a minimum resolution of $r \approx 1.5$kpc.

Gravitational softening [kpc]	0.01	0.1	0.25	0.5	1
Computing time [h:m]	14:20	3:34	2.33	1:50	1:42

Table 6.2: *Softening and corresponding computing time for* $1.5t_u$*. Each simulation has been run on four oct-core computers.*

6.4 Gas Parameters

Most of the values of the gas parameters were chosen simply because they were suggested in the standard parameter file that is distributed with GADGET-2. They are shown in table 6.3.

N_{sph}	50 ± 1
α_{visc}	0.8
α_{cour}	0.1
h_{sph}	$> 0.1h$

Table 6.3: *Gas parameters.*

In addition to the three time criteria in equations (4.17-4.19), we require that the time step has a maximum value. This is to protect against too large time steps for particles with very small acceleration. Usually a few percent of the dynamical time of the system gives sufficient accuracy:

$$\Delta t_{\max} = 0.02 t_u. \tag{6.5}$$

6.5 Radiation, Star Formation and Feedback Parameters

Choosing the right parameters for radiation and star formation is difficult and usually involves a lot of testing. We will adopt a set of well-tested parameters that have previously been used to model mergers between galaxies with GADGET-2 and with the same model for radiation and star formation [24].

t_{th}	$0.00032 \cdot 10^{10}$ $\text{M}_\odot/\text{kpc}^3$
t_*^0	$3.5\ t_u$
T_{SN}	$1.25 \cdot 10^8$ K
T_{cold}	1000.0 K
β	0.1
A_0	1250.0

Table 6.4: *Parameters for radiation, star formation and feedback.*

6.6 Tests

To make sure the simulation parameters are sound and that the created structures really are in equilibrium, we now perform a series of tests.

6.6.1 Adiabatic Simulations

We let each structure run for $3.0t_u$, taking snapshots every $0.6t_u$. By looking at how the structures evolve from snapshot to snapshot we can get an idea of how stable they are. For all the structures we find that any initial instabilities settle into an equilibrium within $r = 1000$kpc before $t = 1.5t_u$.

In figure 6.2 we plot the dark matter density as a function of radius for the structure S1a. As expected the inner slope ends up a bit more gentle than the initial profile because of the gravitational softening. The same thing happens for S1b, S1c and S5a. For S2a, S2b, S4a and S4b, however, the initial profiles are already too shallow to be affected, and the inner slope remains the same. The opposite happens for S3a and S3b. With their steep inner slopes they suffer greatly under the softening, and they end up having an almost flat density profile in the inner region. For all the structures, the final dark matter density profiles lie very close to the initial profiles for $r > 10$kpc.

In figure 6.3 we plot the dark matter velocity anisotropy as a function of radius for the structure S1a. Apart from some scattering in the inner and outer regions, the final profile is very similar to the initial profile. The velocity anisotropy profiles for S1b, S1c, S2a, S2b, S4a, S4b and S5a are also very well-behaved, again it is S3a and S3b that stand out. The change of their density profiles has affected their velocity anisotropy profiles, and the final velocity anisotropy profile of S3a lies a bit above zero, while the final velocity anisotropy profile of S3b lies a bit above zero in the inner region and a little below unity in the outer region.

In figure 6.4 we see that the final temperature of the gas of S1a remains close to the initial temperature. In figure 6.5 we compare the internal energy of the gas to the radial and tangential velocity dispersions of the gas. Because the SPH equations describe the gas from a frame of reference that moves with the gas, the velocity dispersions are very small compared to the internal energy. Therefore we do not need to take them into account, when we calculate the temperature of the gas.

When we derived the equation of hydrostatic equilibrium and the Jeans equation, we assumed that our structures were spherical and free of bulk motion. To check if these are valid assumptions, we plot the total mass of S1a together with the right hand side of equations (3.8) and (3.39). We see in figure 6.6 that the equations hold perfectly within $r = 1000$kpc.

Figure 6.7 shows a contour plot of the radius of the particles in S1a at $t = 0$ and $t = 3.0t_u$. Most of the points lie close to the straight line, where the radius of a particle is the same for $t = 0$ and $t_u = 3.0t_u$. This means that the initial structure does not change much as it settles into equilibrium; the particles remain in their initial orbits. The deviations from the main line occur because the particles are caught at different points in their elliptical orbits. The corresponding plots for the other structures are very similar. There is a tendency for the plots to be broader for the structures with an Osipkov-Merrit model. This is because their

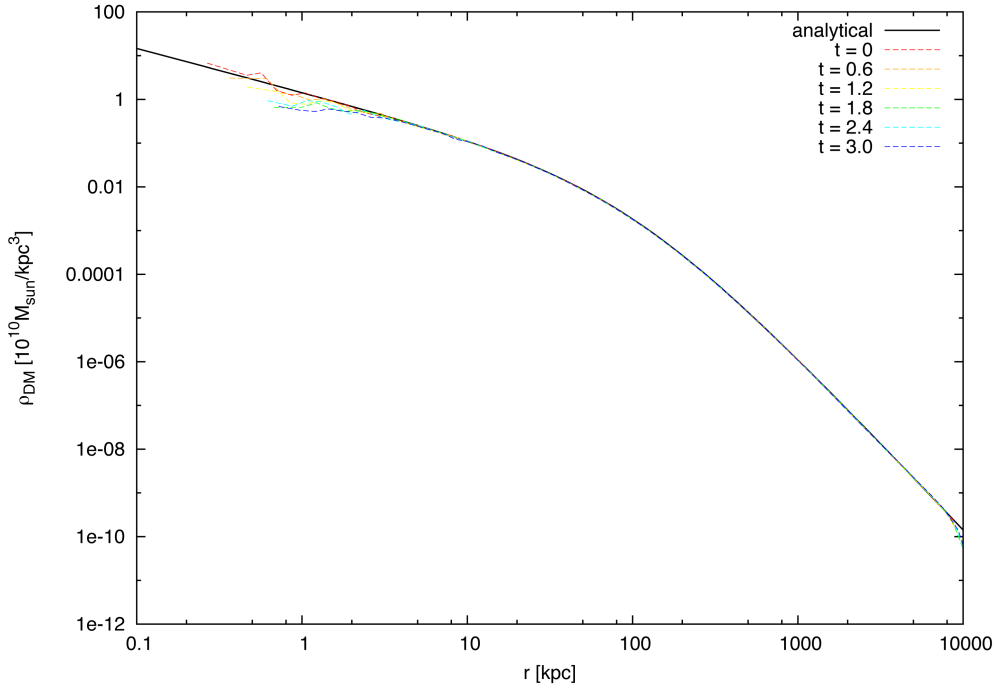

Figure 6.2: *The dark matter density profile of S1a.*

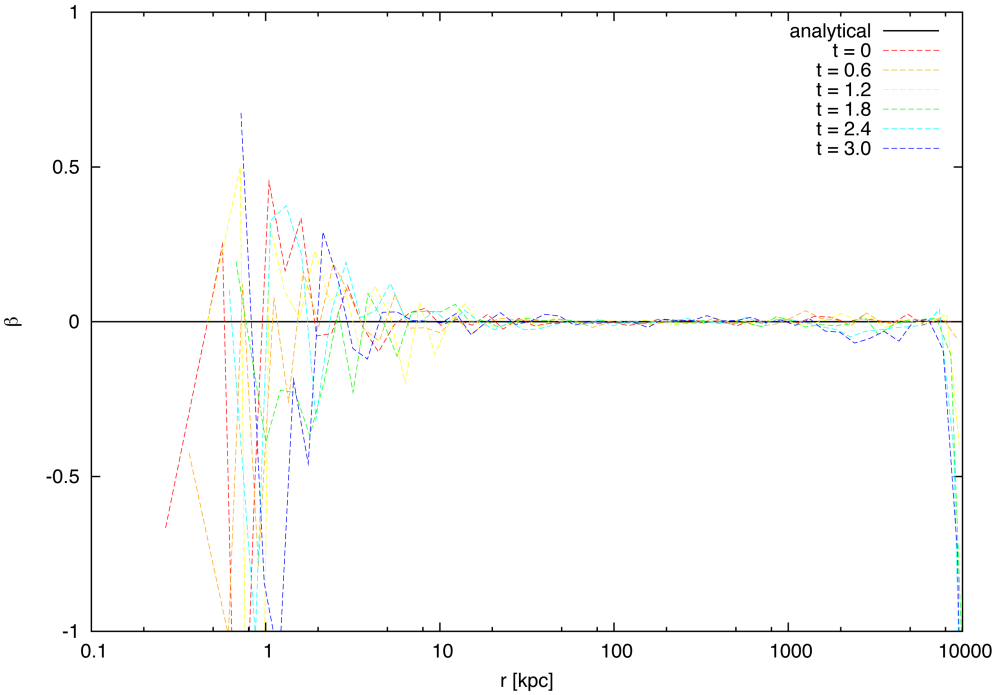

Figure 6.3: *The velocity anisotropy profile of S1a.*

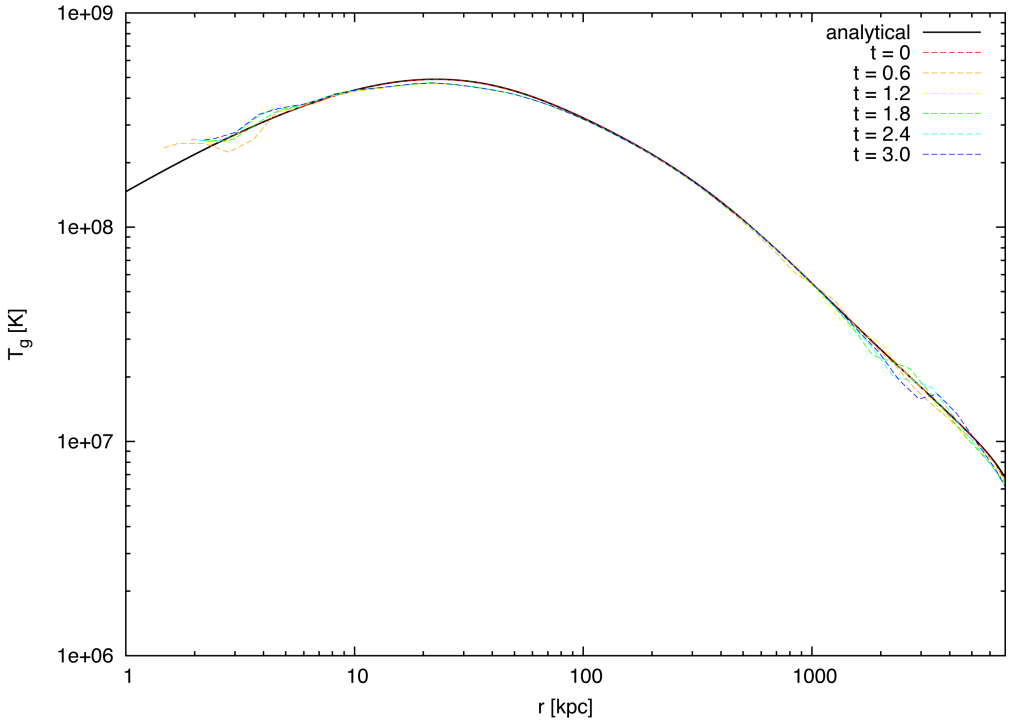

Figure 6.4: *The gas temperature profile of S1a.*

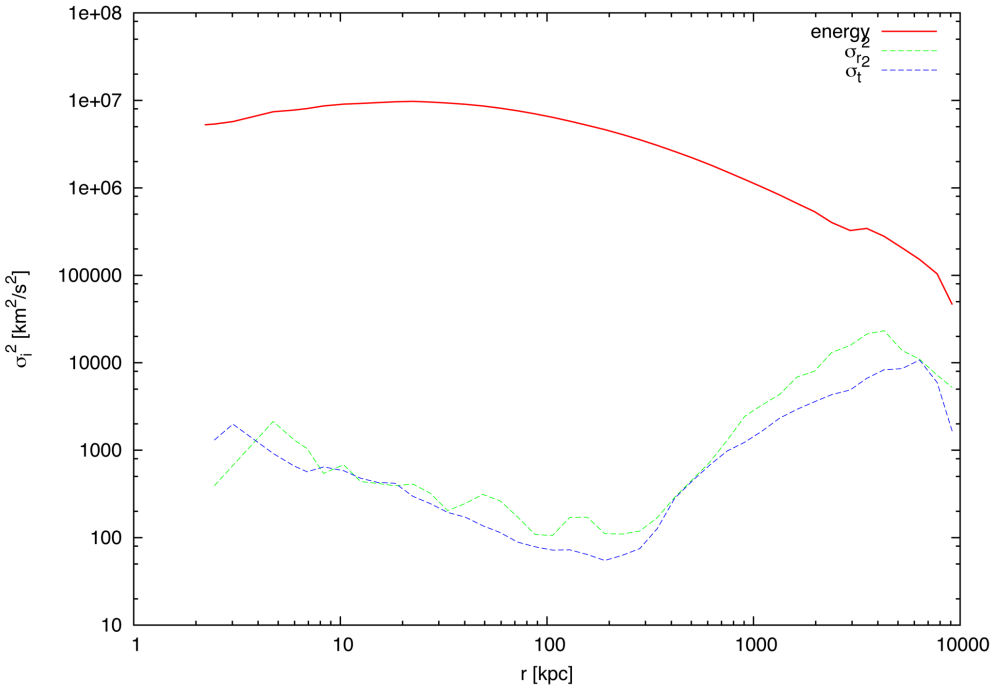

Figure 6.5: *The gas energy profile and velocity dispersions of S1a.*

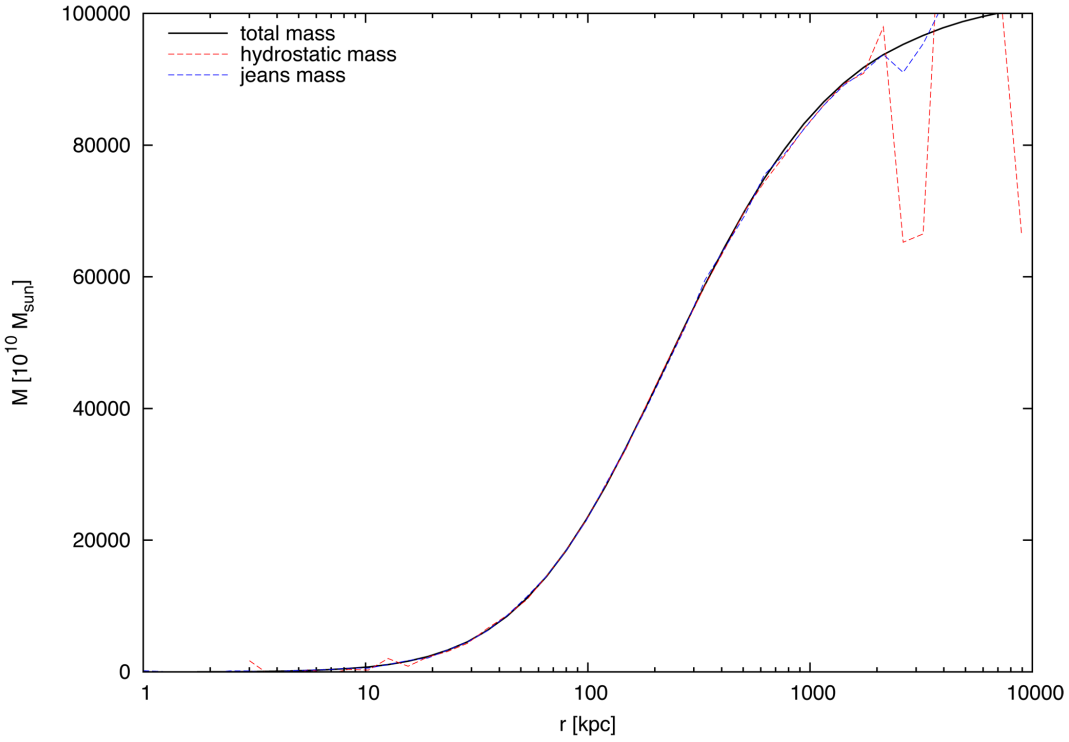

Figure 6.6: *The total mass, hydrostatic mass and Jeans mass of S1a.*

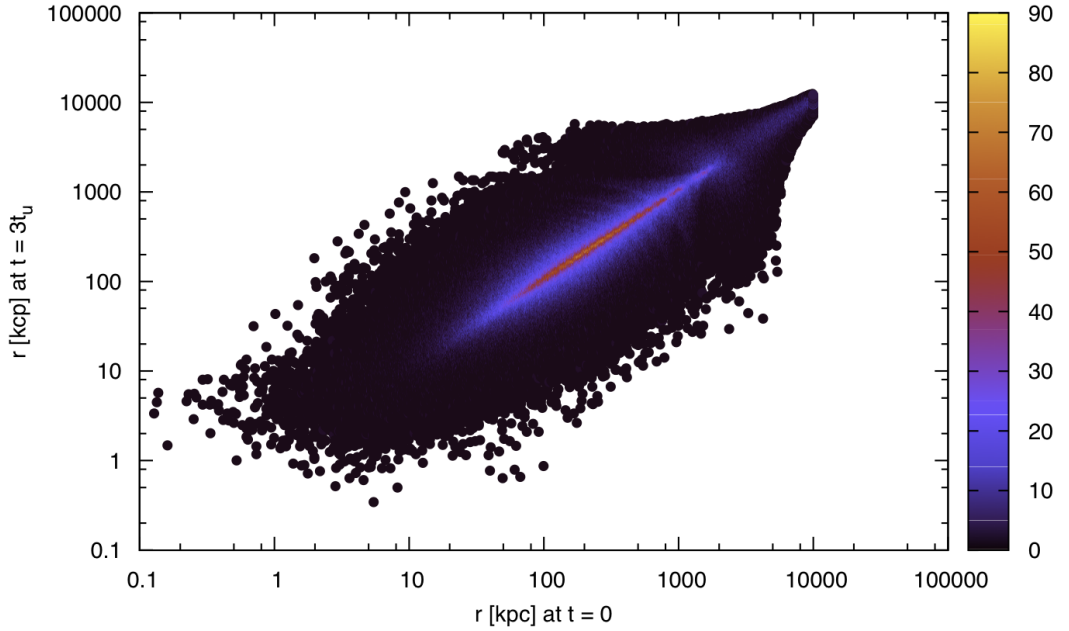

Figure 6.7: *Contour plot of the radii of the particles of S1a at* $t = 0$ *and* $t = 3.0t_u$.

particles are more radially biased.

6.6.2 Simulations with Radiation and Star Formation

To check if the radiation and star formation parameters are sound, we will run S1a for $3.0t_u$ with radiation and star formation activated.

Figure 6.8 shows a contour plot of the gas density and temperature. We see that the gas temperature beyond the inner region (lower densities) has the temperature of hydrostatic equilibrium. In the inner region (higher densities) the gas cools rapidly because of the high density, and star formation sets in.

In figure 6.9 we plot the average radial velocity of the gas. There is a lot of scattering in the inner region where the star formation takes place. Further out the velocity is slightly below zero indicating a small flow of gas inwards. As the gas in the centre of the cluster cools, its pressure drops, and the pressure of the ICM further out causes more gas to flow inwards. This is called a cooling flow.

In figure 6.10 we plot the density profiles of the dark matter, gas and stars. The plot confirms that stars are created from the gas in the central region as expected.

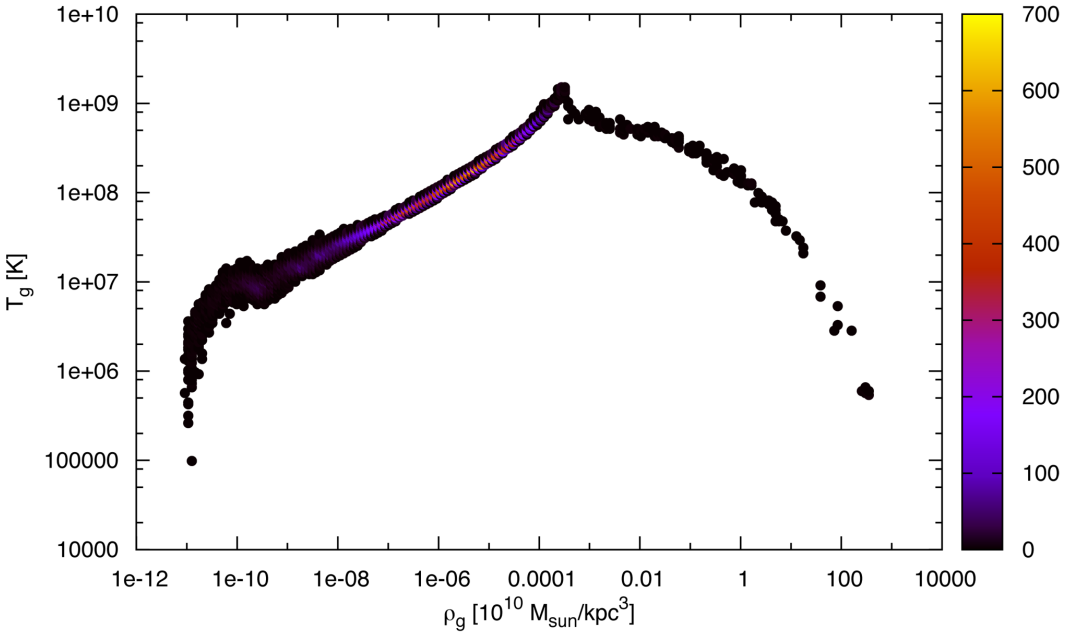

Figure 6.8: *Contour plot of the gas density and temperature for S1a at* $3.0t_u$.

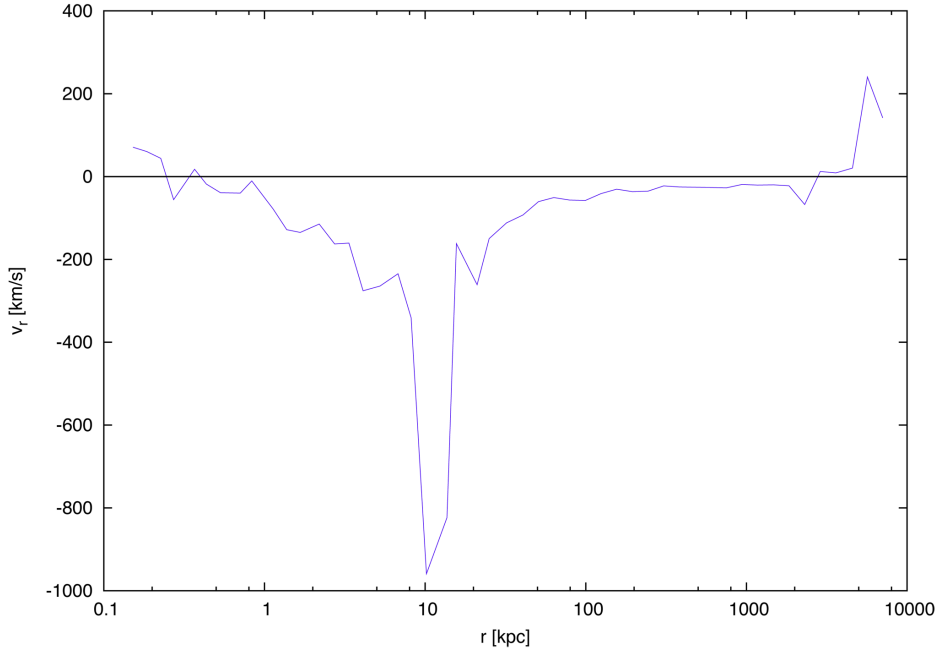

Figure 6.9: *Average radial velocity of the gas particles of S1a at* $3.0t_u$.

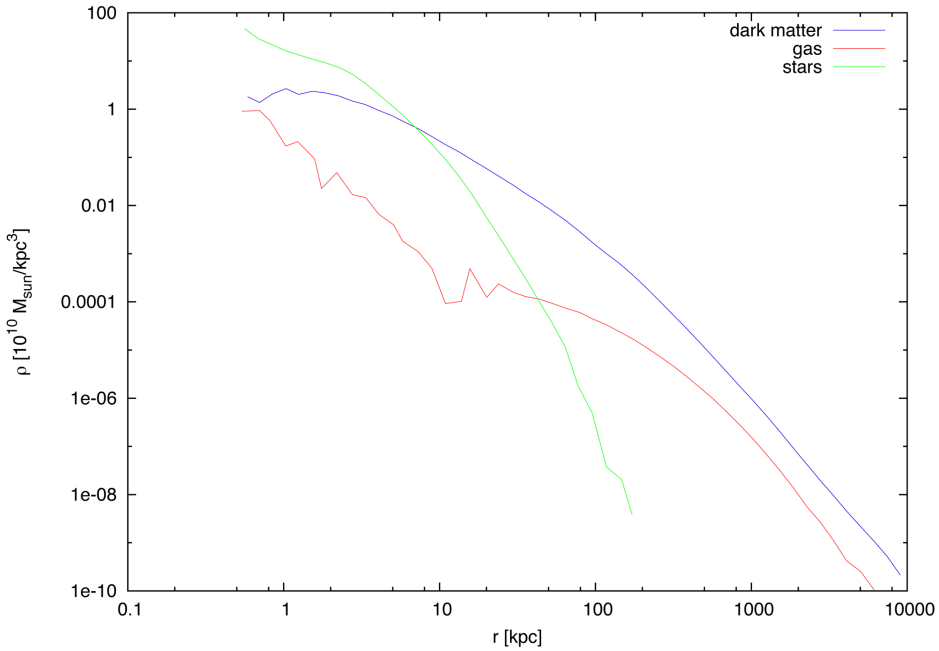

Figure 6.10: *The density profiles of the dark matter, gas and stars of S1a at* $3.0t_u$.

7 Perturbations

When we perturb a structure, we push it out of equilibrium. Subsequently, the particles will adjust in order to find a new equilibrium. If there exists no attractor of any kind, we would expect the particles to choose a random path back to equilibrium. If, on the other hand, there does exist some kind of attractor, we would expect the particles to move towards that attractor on their path to equilibrium. We will therefore search for systematic changes in e.g. the velocity dispersion when we perturb the structures.

We will perform three different types of perturbations: perturbations of the dark matter only, perturbations of the gravitational constant, and mergers. While the first type is mild and barely affects the structures, the second and third types are very violent, as they change the potential drastically and send shockwaves through the structures.

7.1 Dark Matter Perturbations

The dark matter perturbation interchanges energy between the dark matter particles:

1. We divide the dark matter particles into 50 logarithmically distributed radial bins and calculate both the kinetic energy of each particle and of the whole bin.

2. For each particle, we generate a uniformly distributed number $u \in [1 - p; 1 + p[$, where $p \in]0; 1]$ is related to the strength of the perturbation.

3. We check if the product of the speed of the particle and the square root of u is less than the escape velocity. If this is the case, we continue to step 4, if not we repeat step 2 until it is.

4. We multiply each velocity component of the particle with the square root of u. This conserves the average kinetic energy of a bin and of the structure as a whole to a good approximation.

5. To obtain perfect kinetic energy conservation we scale the total kinetic energy of each bin so that it is exactly the same as before.

After having perturbed a structure we let it run for $1.5t_u$, thereby allowing it to reach a new equilibrium state. We repeat this procedure, a kick followed by a flow, a number of times, until it does not affect the structure anymore.

The dark matter perturbation is instantaneous, since it affects the velocities directly. During the flow phase, some of the particles will move further out, while others will move closer to the centre, so the perturbation gives rise to phase mixing.

If the perturbation is too small (i.e. p is too small) nothing will happen, and if it is too large, the resulting velocity distribution functions will become too unnatural. We perform a series of ten perturbations with $p = 0.25$, $p = 0.50$ and $p = 0.75$ for S1a. The results are presented in figures 7.1-7.3, where we plot the radial velocity dispersion of the dark matter. We see that all the perturbations move the structure in the same direction although at different paces, so the range of strengths they cover can all be used. The stronger the perturbation is, the fewer perturbations we need to perform, and we will therefore use $p = 0.75$.

To demonstrate how mild this type of perturbation is, we perform 10 perturbations in a row with no flow between the kicks. The result is presented in figure 7.4, where we see that the radial velocity is completely unaffected.

7.2 Perturbations of the Gravitational Constant

Using a gravitational constant with a value that is larger or smaller than the true value, changes the forces between the particles. As a result they are bound either more tightly or more loosely, and the structure as a whole will contract or expand. A few experiments show that changing the value of G by twenty percent combined with running a structure for $1.5t_u$ perturbs the structure without destroying it. We will perturb the structures by alternating between a larger and smaller gravitational constant.

The G perturbations are continuous as they affect the accelerations and not the velocities of the particles. Since the potential is a function of G, the perturbations change the potential and thus the energy of the particles. The perturbation therefore gives rise to violent relaxation.

7.3 Mergers

The mergers are carried out by placing the centres of two identical structures 2 Mpc apart and giving them a relative velocity of -200 km/s. With ten different structures, this gives us ten different mergers. The mergers all have an impact parameter of zero. Like the G perturbations, the mergers are continuous and give rise to violent relaxation.

Unlike the two other types of perturbations, the mergers are more of a toy experiment instead of a serious study. The latter would require us to perform mergers with for example varying masses and impact parameters. For elongated structures that have already been merged once, we could also perform additional mergers, changing their orientation with respect to each other.

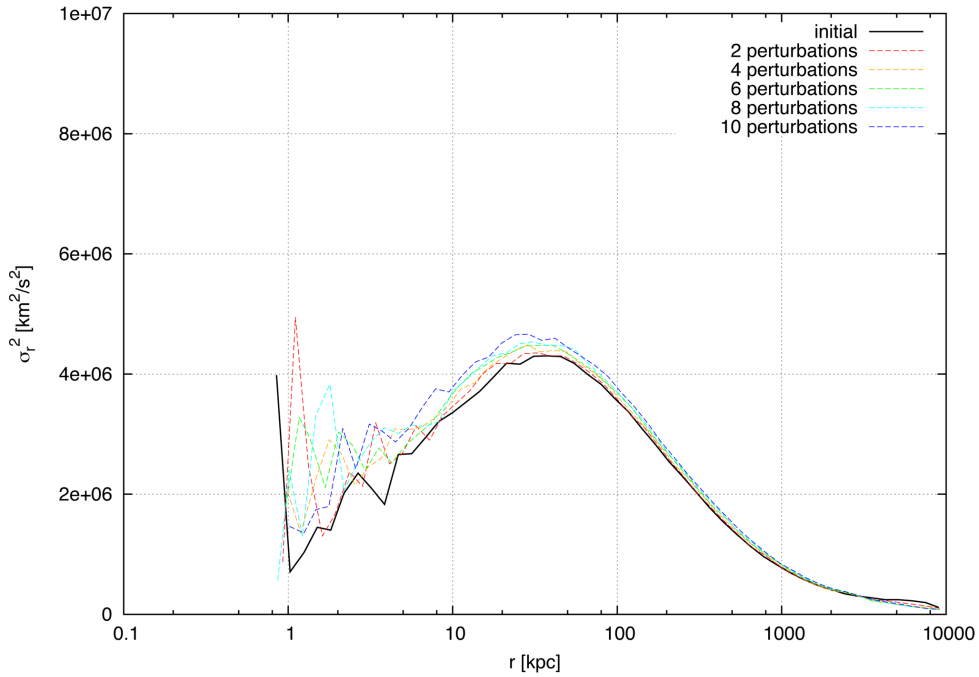

Figure 7.1: *The result of ten dark matter perturbations with $p = 0.25$ for S1a.*

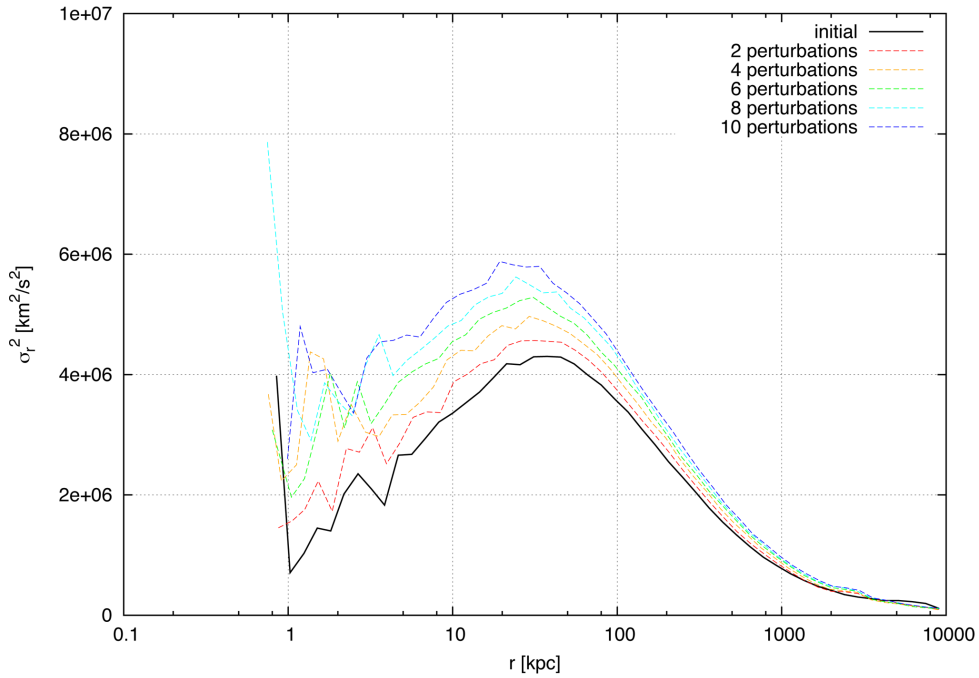

Figure 7.2: *The result of ten dark matter perturbations with $p = 0.50$ for S1a.*

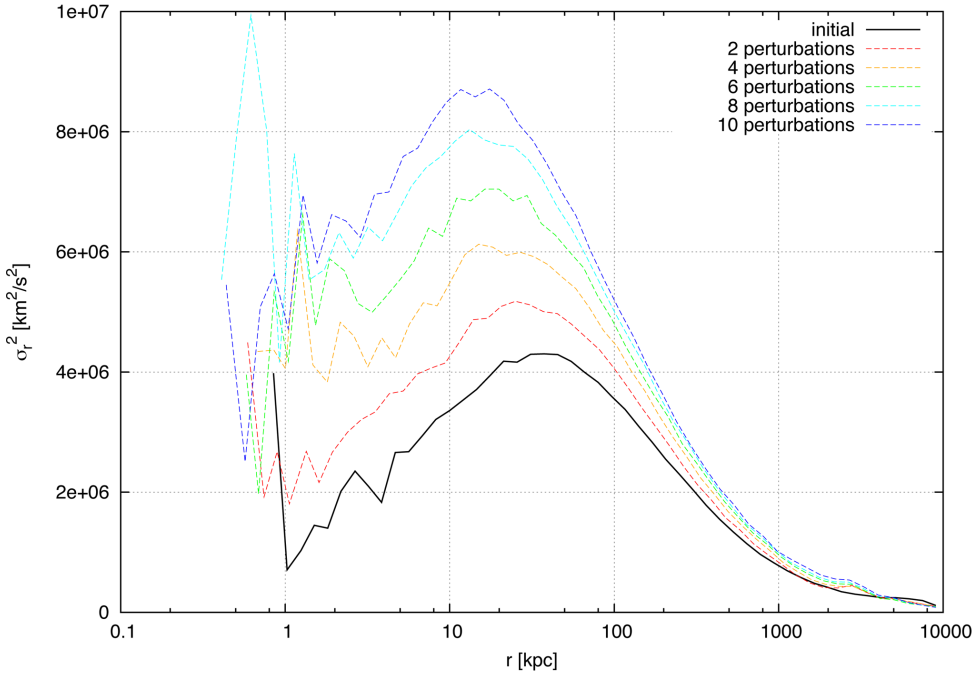

Figure 7.3: *The result of ten dark matter perturbations with* $p = 0.75$ *for S1a.*

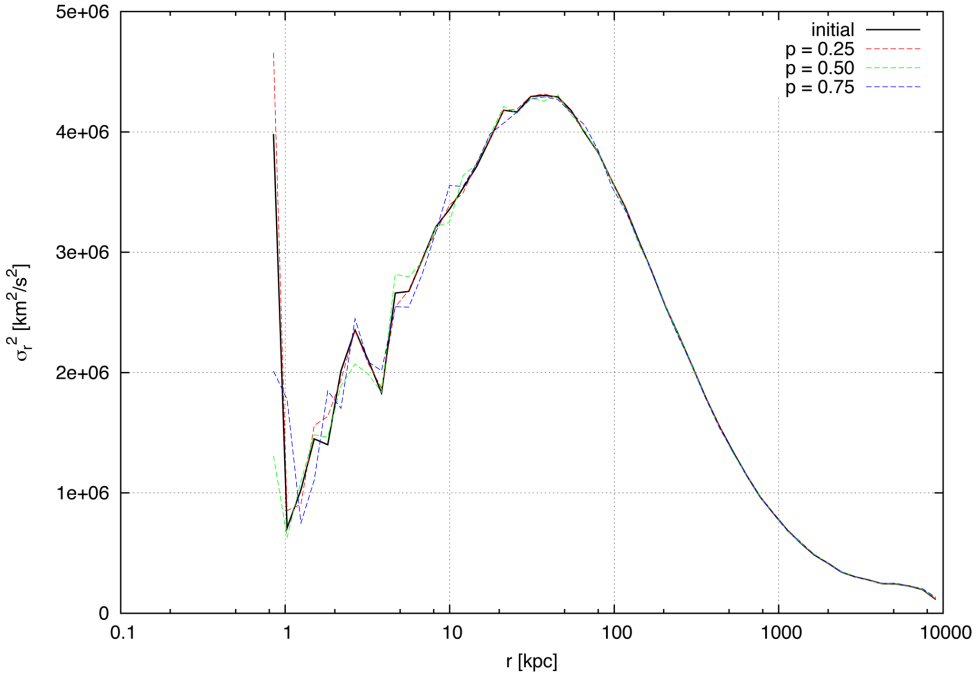

Figure 7.4: *Ten successive dark matter perturbations with* $p = 0.25$, $p = 0.50$ *and* $p = 0.75$ *with no flow between the kicks. The kicks themselves do not change the radial velocity dispersion.*

8 Adiabatic Simulations

We will carry out the first round of perturbations using adiabatic simulations. We will search for two different attractors: the Jeans relation for dark matter and the relation between the temperature of the gas and the dark matter. Compared to simulations with radiation and star formation, there are a lot fewer parameters to handle, so this should make for an easier start. Although adiabatically simulated clusters do not reflect what happens in real clusters, it will be interesting to compare them with other adiabatic simulations. If our results match those of other studies it will confirm that we are on the right track.

8.1 Perturbations

Before we perturb the structures, we let them run for $3t_u$ to make sure, they are in equilibrium. For the dark matter perturbations, we use structures containing one million particles, and each structure is perturbed thirty times. For the G perturbations we use structures containing one million particles, and each structure is perturbed twenty times. The first perturbation uses $\widetilde{G} = 1.2G$, the second $\widetilde{G} = 0.8G$, the third $\widetilde{G} = 1.2G$ and so on. Both the dark matter and G perturbations are evolved an additionally $5 \cdot 1.5t_u$ after the last perturbation to make sure the structures are in equilibrium. For the mergers, we use structures containing 100,000 particles, and the result of each merger will therefore contain 200,000 particles. The mergers are evolved for $20 \cdot 1.5t_u$.

To check whether the structures really approach an attractor in a systematic manner, we plot the radial velocity dispersion of the dark matter as a function of radius for the dark matter perturbations and the G perturbations. In figure 8.1 we plot[1] the result of every fifth dark matter perturbation of S1a. The velocity dispersion profile grows systematically, fluctuates a little and then remains stable. The reason for the fluctuation is most likely that the velocity dispersion is dependent on other properties of the structure (such as the density profile) that are still changing a little.

The G perturbations are more tricky. In figure 8.3 we plot the radial velocity dispersion of every fourth G perturbation of S1a starting with the first perturbation, and in figure 8.2 we plot the radial velocity dispersion of every fourth G perturbation of S1a starting with the third perturbation. The uneven perturbations (perturbation number 1, 3, 5 etc.) increase the gravitational constant. This binds the particles tighter and will therefore increase the radial velocity dispersion. The even number of perturbations, on the other hand, bind the particles looser, and will therefore decrease the radial velocity dispersion. Together,

[1]Note that for this kind of plots (the result of one type of perturbation of one type of structure) we have a total of 30 different plots, since we are working with three different perturbations of ten different structures. To spare the reader for this overwhelming amount of plots, we will only include a small selection in the thesis.

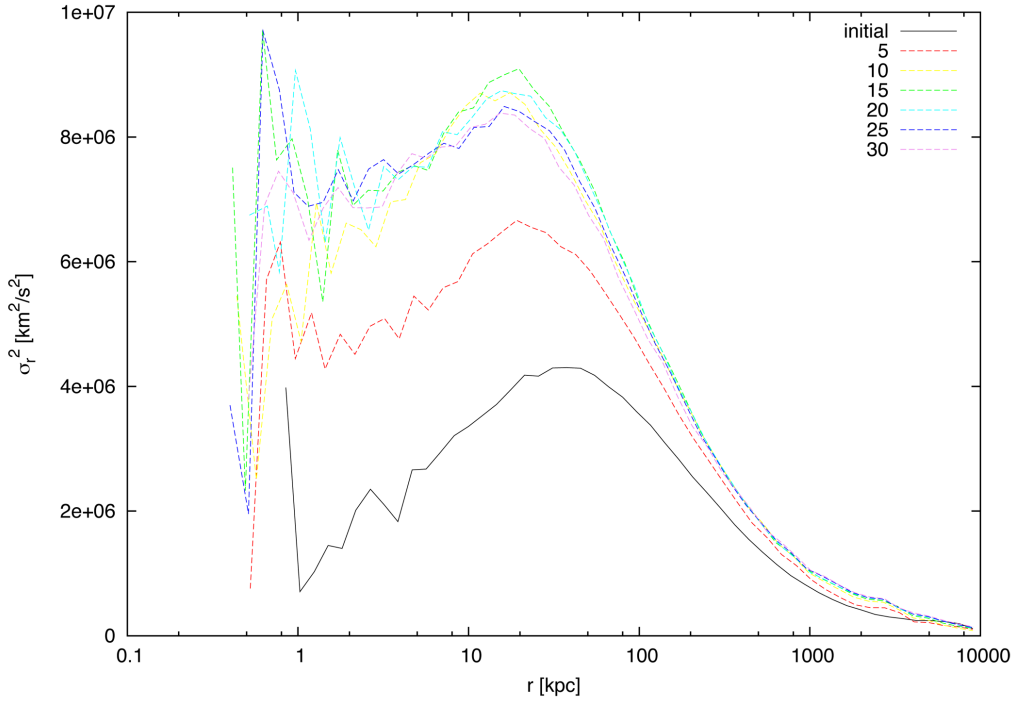

Figure 8.1: *The radial velocity dispersion of S1a after every fifth dark matter perturbation.*

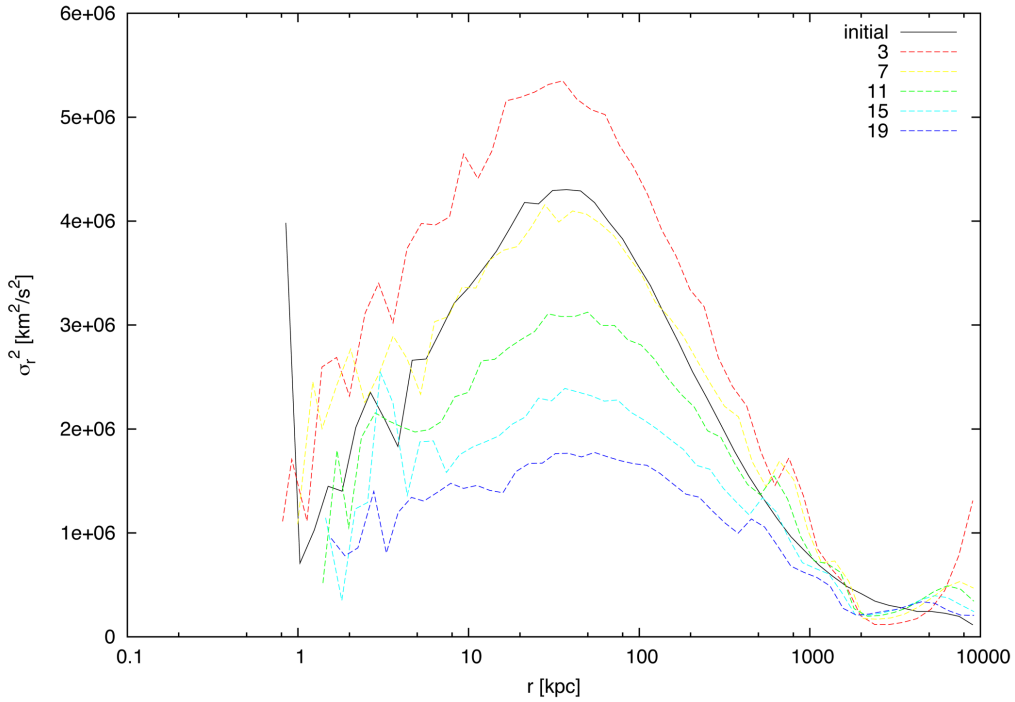

Figure 8.2: *The radial velocity dispersion of S1a after every fourth G perturbation.*

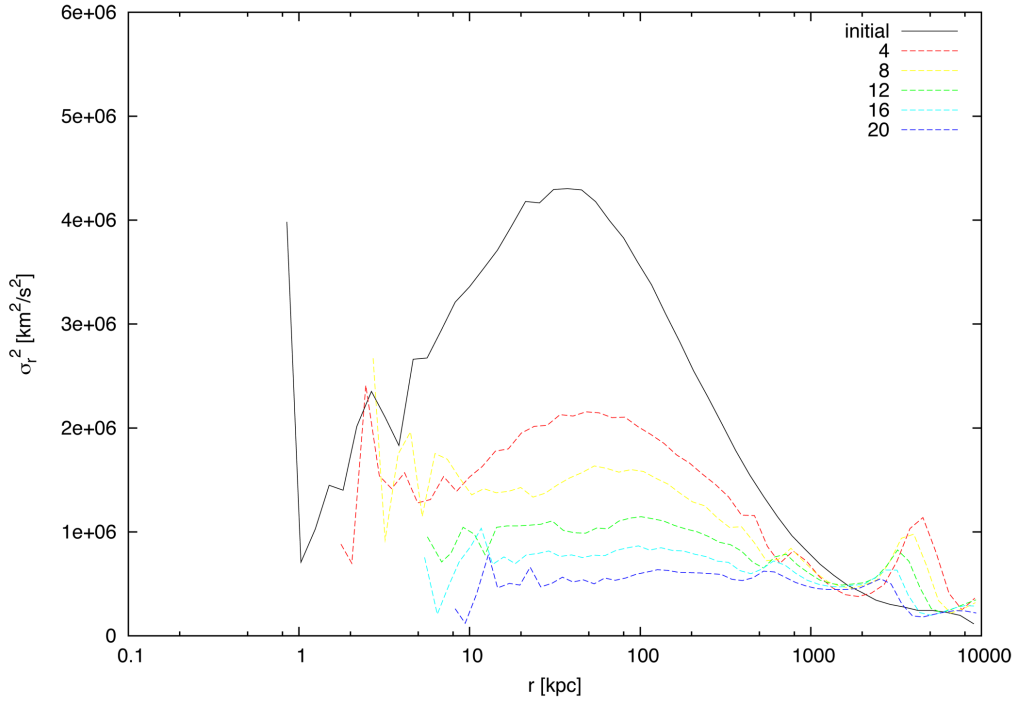

Figure 8.3: *The radial velocity dispersion of S1a after every fourth G perturbation.*

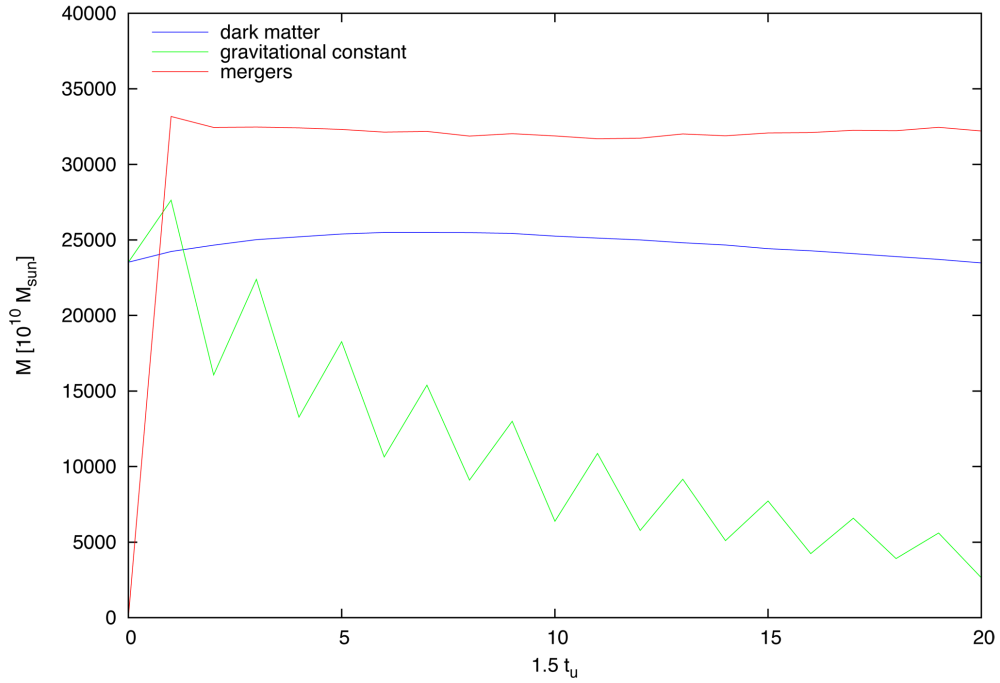

Figure 8.4: *The total mass within the scale radius of S1a for each successive perturbation.*

the perturbations alternately increase and decrease the radial velocity dispersion. Overall, though, the radial velocity dispersion decreases. Looking closer at the figures, we see that the minimum radius shifts to the right. The violent perturbations pushes the particles of the structure outward and away, and this is why the radial velocity dispersion is ultimately decreasing.

In figure 8.4 we plot the total mass within r_0 as a function of time for all three types of perturbations. This confirms that mass is being moved outwards: while the mass within r_0 remains more or less constant for the dark matter perturbations and the mergers, it decreases quite a lot for the G perturbations. It seems that too many G perturbations will eventually ruin the structure, or at least leave us with nothing to analyse in the inner region.

8.2 Shape and Bulk Motion

We begin our analysis by examining whether the equation of hydrostatic equilibrium and the Jeans equation are still valid for the perturbed structures. The initial structures were spherical and had no bulk motion, but these properties could easily have been disturbed by the perturbations.

In figure 8.5 we plot the eccentricity of the perturbed structures (see details in Appendix A.6). They are clearly grouped according to the type of perturbation. Both the dark matter perturbations and the mergers result in structures with a peak in eccentricity, while the spherical nature of the G perturbations leaves the eccentricity of most of the structures almost unaffected. For the G perturbations, four structures with an unusually large eccentricity stand out: S1b, S1c, S2b and S4b. They are also the most eccentric structures of the mergers and of the dark matter perturbations beyond the scale radius. This deviation from the other structures is most likely due to the so-called radial orbit instability. It occurs, when the gravitational field of a small over-density among the radial orbits attracts more particles, and the result is a triaxial system instead of a spherical system [3, p. 434-437]. The behaviour of the radial orbit instability is closely related to the fraction of mass that follows radially anisotropic orbits: the larger the fraction of mass beyond the anisotropy radius, the more it will affect the shape of the structure [1]. The anisotropy radii of the initially isotropic structures are in principle infinitely far away, and these structures will therefore not exhibit any radial orbit instability. Neither will S3b, since so much of its mass is concentrated within its anisotropy radius. That leaves precisely S1b, S1c, S2b and S4b. S1c is affected less than S1a because it has a larger anisotropy radius, and S4b is affected most of all because it is the structure with the most mass beyond its anisotropy radius.

One could imagine that there exists a relation between the eccentricity of a structure and its velocity anisotropy. Some galaxies, for example, are very flat and therefore also anisotropic. This is not something we will investigate thoroughly, but at least the plot in figure B.1 shows that any such relation is definitely not

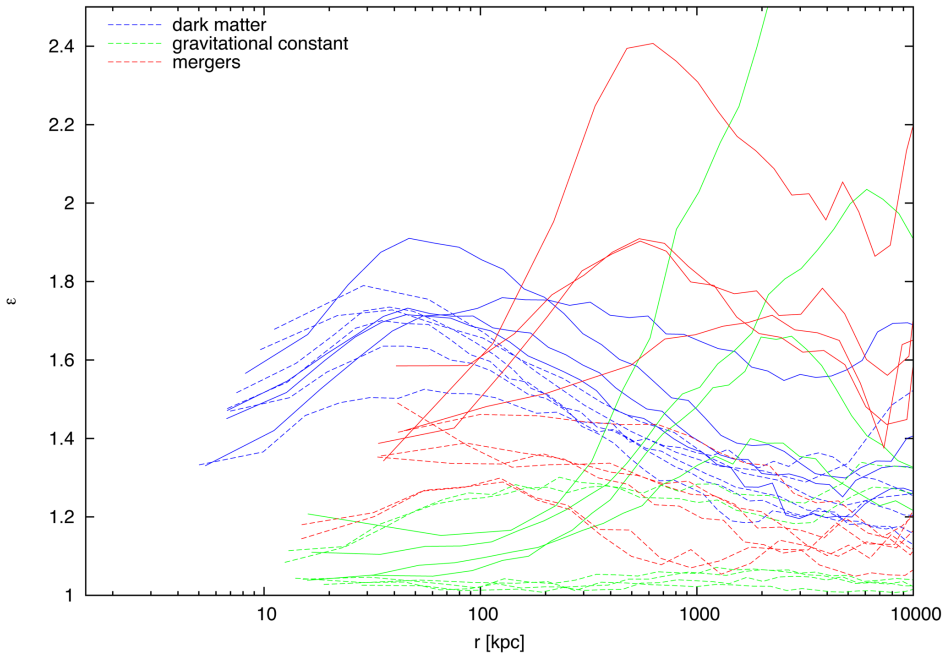

Figure 8.5: *The eccentricity of the final structures. The solid lines represent the structures S1b, S1c, S2b and S4b.*

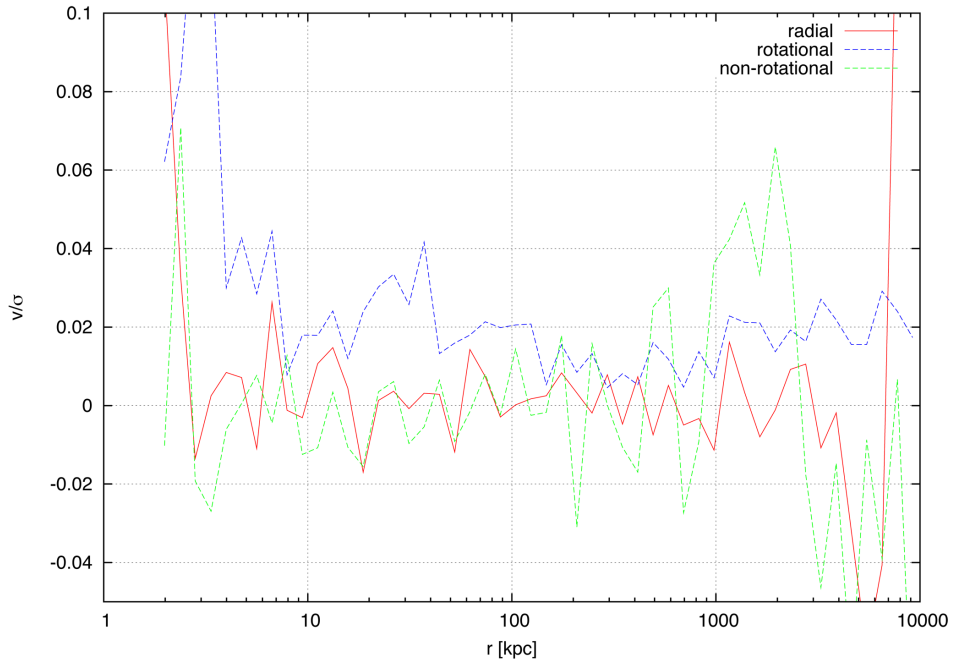

Figure 8.6: *The average dark matter velocities with respect to the velocity dispersion for the dark matter perturbed S1a.*

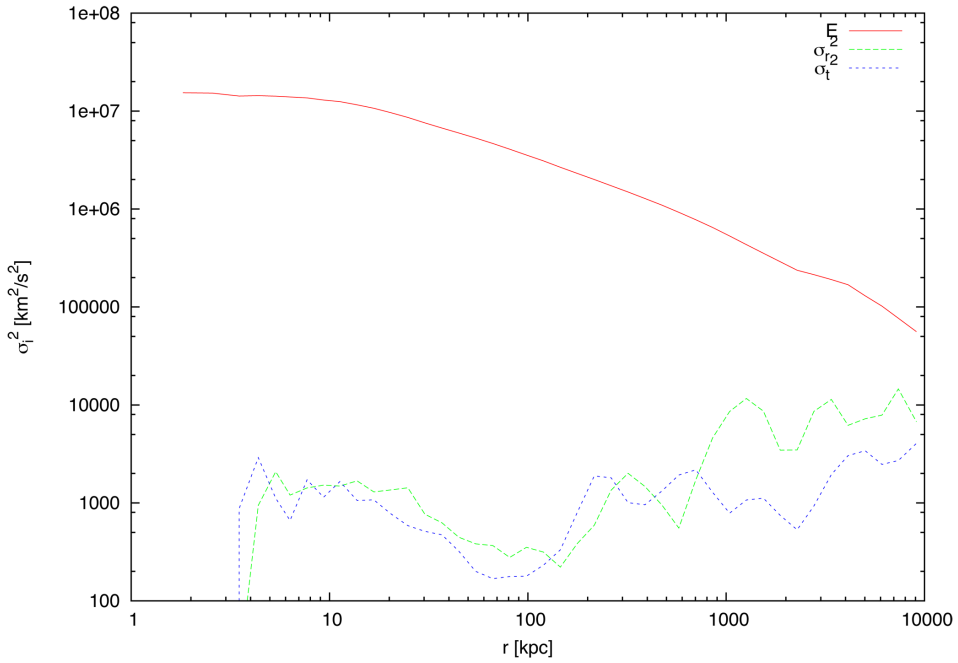

Figure 8.7: *The internal energy and the radial and tangential velocity dispersion for the dark matter perturbed S1a.*

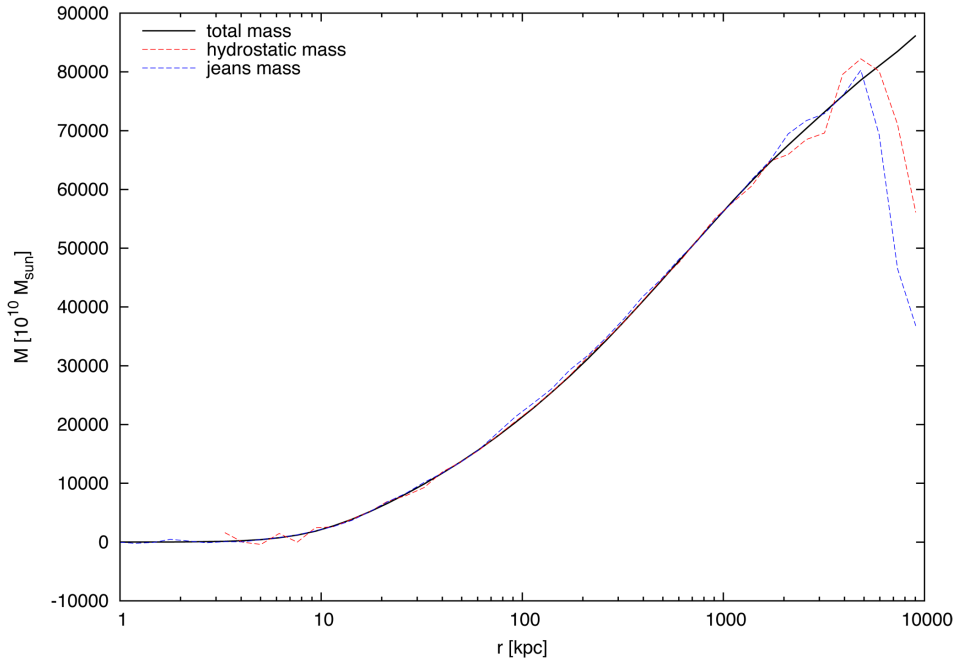

Figure 8.8: *The total mass, the Jeans mass and the hydrostatic mass for the dark matter perturbed S1a.*

linear.

In figure 8.6 we plot the average dark matter velocities divided by the velocity dispersions of the dark matter perturbed S1a. The tangential velocities have been split into a rotational and a non-rotational part as described in Appendix A.7. Both the radial and the non-rotational velocities fluctuate closely around zero within $r = 1000$kpc. The rotational velocity always lies slightly above zero. This is because of how we define the direction of the component. The rotational velocity is about 2-3% of the rotational velocity dispersion, so there is no serious rotation. For all the perturbed structures, the same picture emerges: the radial and tangential velocities fluctuate close to zero, and the rotational velocities are less than 5% of the rotational velocity dispersions. We can therefore conclude that the perturbed structures show no significant bulk motion.

In figure 8.7 we compare the internal energy of the gas to the radial and tangential velocity dispersions of the gas for the dark matter perturbed S1a. The velocity dispersions have remained small compared to the internal energy, and we will therefore not need to take them into account, when we calculate the temperature of the gas. This is the case for all the perturbed structures.

Comparing the total mass with the right hand side of the equation of hydrostatic equilibrium (3.8) and the Jeans equation (3.39) for all the structures, we find that they match almost perfectly within $r = 1000$kpc for all three types of perturbations. The deviations are typically within 5%. In figure 8.8 we plot the total mass, the Jeans mass and the hydrostatic mass of the dark matter perturbed S1a, again demonstrating equilibrium.

8.3 The Jeans Relation

The dark matter perturbations we use, are the same as those that were used to discover the Jeans relation [13]. The relation was found for structures consisting of dark matter only, so it would be interesting to see, if the relation holds for structures containing both dark matter and gas, and if it appears for other types of perturbations. In figure 8.9 we plot $\kappa + \gamma$ as a function of β for the dark matter of the initial structures, and in figures 8.10-8.12 we plot the same for the perturbed structures. Only points for which $2.5\text{kpc} \leq r \leq 1000\text{kpc}$ are included.

As intended, the ten structures span a wide range of initial conditions. Although the Jeans Equation in principle allows all of the presented parameter space to be populated, we have no initial conditions in the upper right corner, where the inequality $2\beta < -\gamma$ prevents any solutions [8].

In figure 8.10 an attractor has clearly emerged. The black, filled circles represents the Jeans relation and has been calculated using the data from the original study [13]. There is some statistical noise in the inner region (small β), where there are fewer particles per bin, and in the outer region (large β) where the structure cannot be completely trusted to be in equilibrium, the attractor broadens. It is worth noticing that the structures have approached a common profile

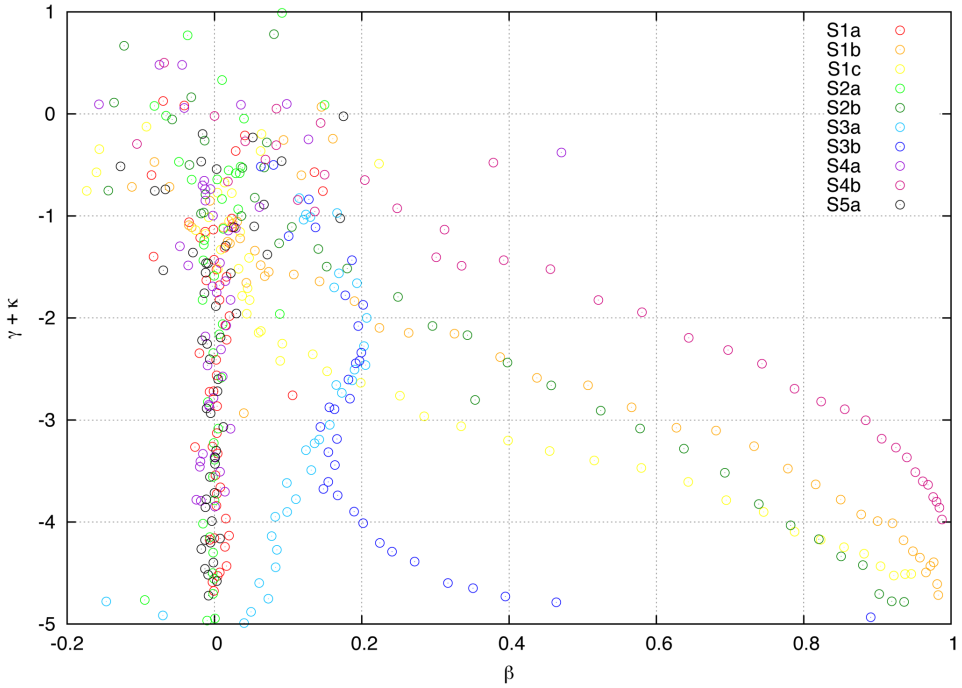

Figure 8.9: *The initial relation between $\gamma + \kappa$ and β. The structures span a wide range of initial conditions.*

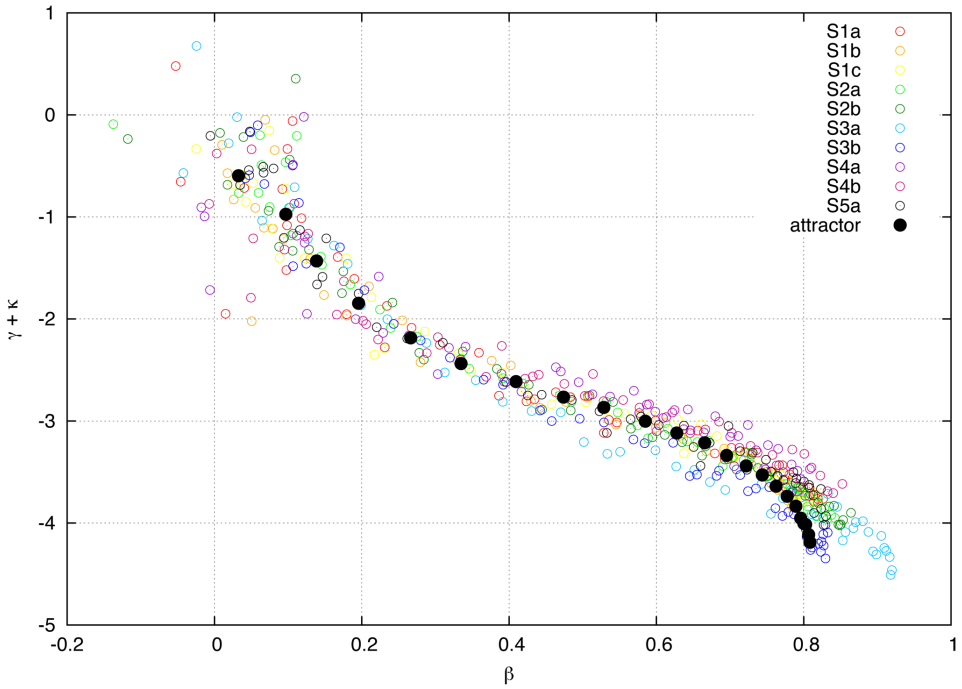

Figure 8.10: *The relation between $\gamma + \kappa$ and β for the dark matter perturbations.*

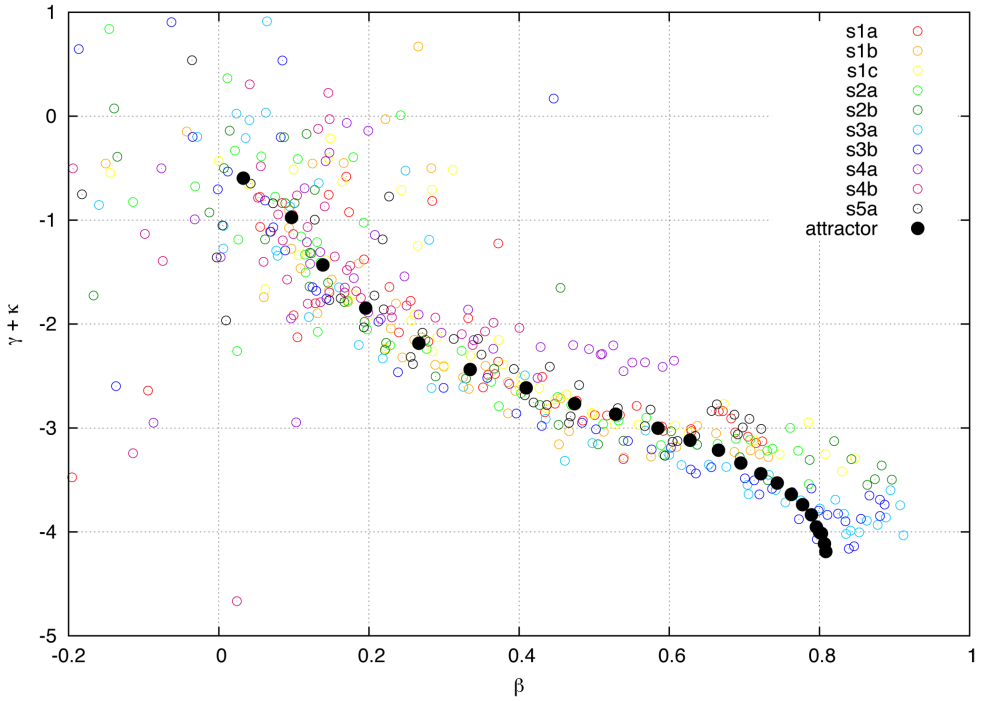

Figure 8.11: *The relation between $\gamma + \kappa$ and β for the G perturbations.*

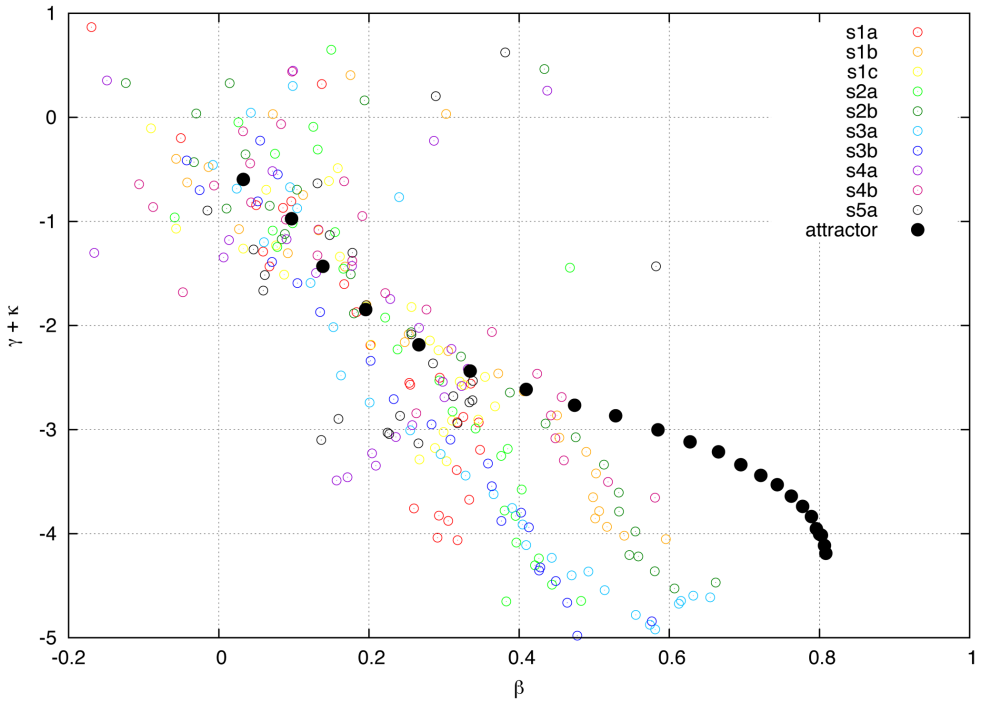

Figure 8.12: *The relation between $\gamma + \kappa$ and β for the mergers.*

from all sides, so the perturbations have not simply manipulated the structures in a specific direction. The attractor matches perfectly with the Jeans relation, and we can therefore conclude that it also exists in structures containing both dark matter and gas.

Despite a larger amount of scatter, it is clear from figure 8.11 that the G perturbations also move the structures towards the Jeans relation. This should eliminate any concerns that the Jeans relation is a result of a specific type of perturbation rather than a real attractor.

For the mergers, we see in figure 8.12 that the final structures roughly follow the Jeans relation for $\beta < 0.6$. Generally, the structures that were initially anisotropic lie closer to the relation for larger radii simply because they started out being closer. For mergers, violent relaxation mainly affects the inner regions, which are therefore perturbed more than the outer regions.

8.4 The Temperature Relation

We now include the gas in our investigations. In figure 8.13 we plot

$$\Gamma = \frac{T_g}{T_{DM}} = \frac{T_g k_B}{\mu m_u} \frac{3}{\sigma_r^2 + \sigma_\phi^2 + \sigma_\theta^2}$$

as a function of r for the initial structures, and in figures 8.14-8.16 we plot the same for the perturbed structures. As for the Jeans relation, the structures span a wide range of initial conditions.

The dark matter perturbations group the structures according to their dark matter density profiles. At the extremes we have the two structures with the most mass concentrated centrally, S3a and S3b, and the two structures with the least mass concentrated centrally, S4a and S4b. After about 30 perturbations, the perturbations no longer affect the structures. This is most likely because the dark matter perturbations are too mild. Once the dark matter has settled on its own attractor, it remains unaffected by the perturbations. As the gas only changes in response to the change in the dark matter, it too will remain unaffected. It is not clear whether the structures were moving towards some attractor before the perturbations stopped affecting them.

In figure 8.15 we see that the G perturbations also group the structures according to their dark matter density profiles. Because the G perturbations are so violent, we only perform 20 perturbations. Unlike the dark matter perturbations, the G perturbations directly affects the gas, and this is probably why Γ is comparatively lower for all the structures. Still, no attractor has emerged. It appears such a thing does not exist for Γ as a function of r for adiabatic simulations.

For the mergers, figure 8.14 shows that the temperature relation is also dependent on the dark matter density profiles. A previous study by Zuhone [42] of adiabatic mergers of galaxies has suggested that $\Gamma \approx 1$, which is clearly not the

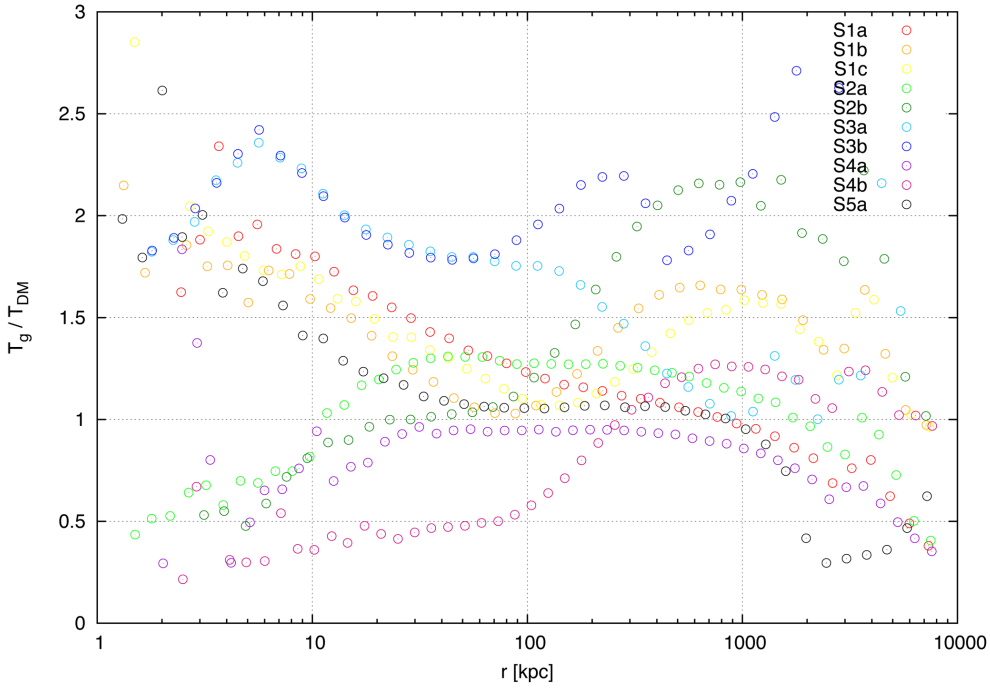

Figure 8.13: *The initial temperature relation. The structures span a wide range of initial conditions.*

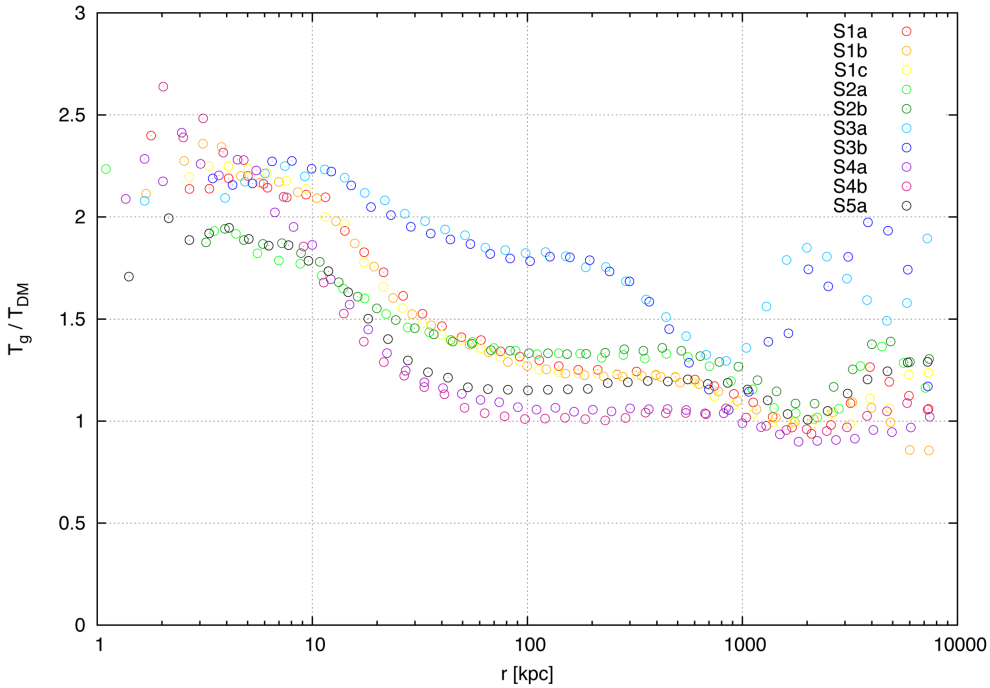

Figure 8.14: *The temperature relation for the dark matter perturbations.*

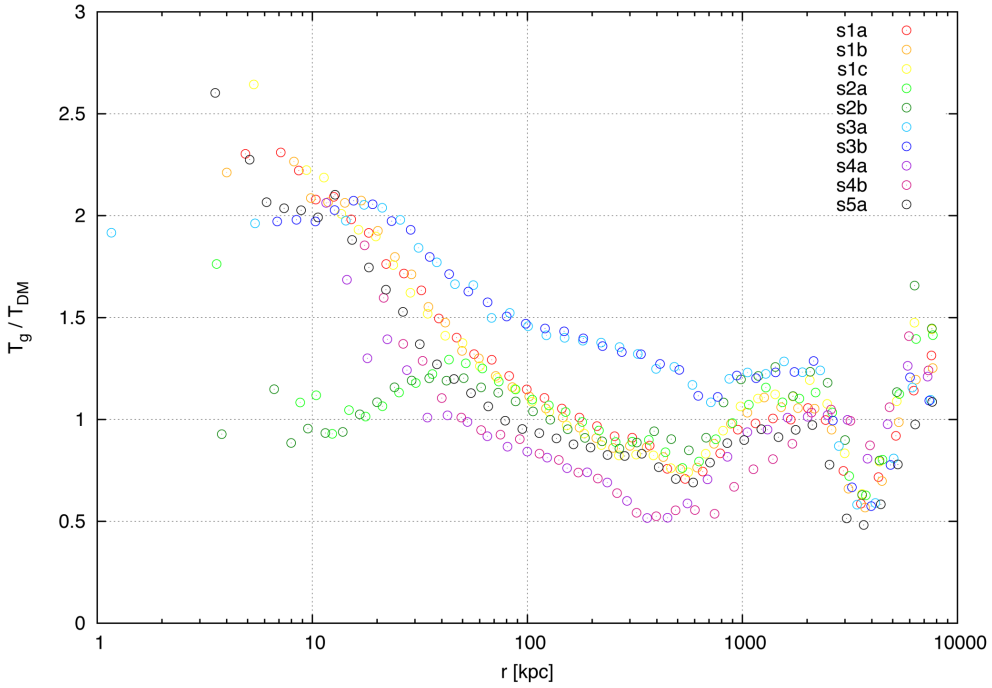

Figure 8.15: *The temperature relation for the G perturbations.*

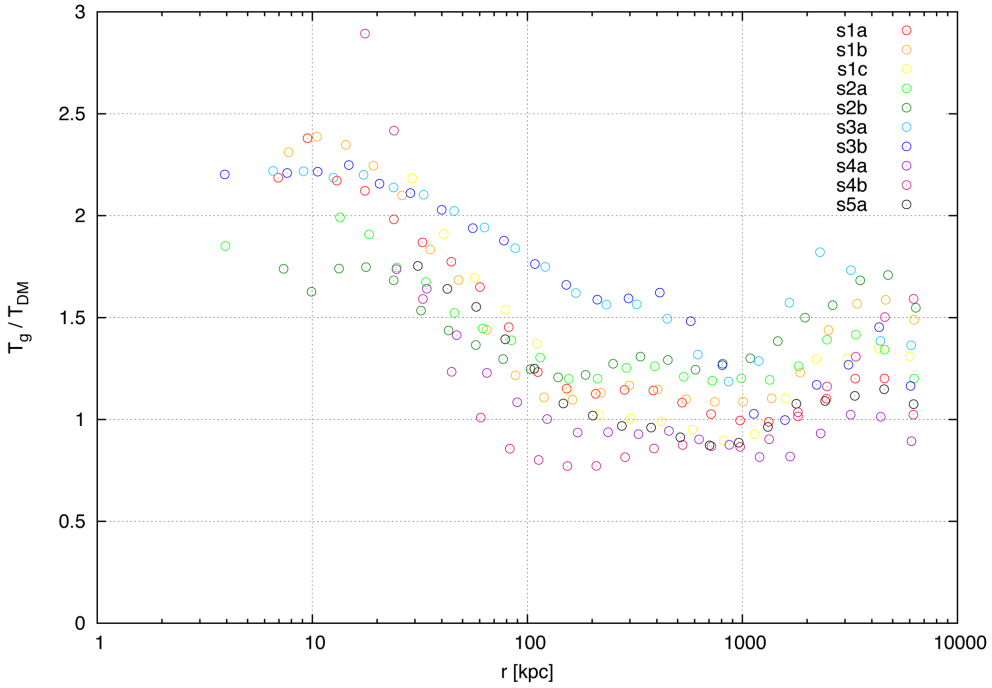

Figure 8.16: *The temperature relation for the mergers.*

case here. However, there is an explanation for this apparent inconsistency. The mergers of Zuhone's study differed in mass and impact parameter, but they all had the same initial dark matter density profile, namely the NFW profile. Among our structures, S1a, S1b and S1c are those that best resemble the NFW profile, and we see that their temperature relations do match the results of Zuhone's study, with $\Gamma \approx 1$ for $r > r_0$. Note that although we compare simulations of structures that differ very much in size, this has no significance, since the simulations are adiabatic and therefore scalable.

9 Simulations with Radiation and Star Formation

We will now turn to our simulations with radiation and star formation. Again, we will investigate the Jeans relation for dark matter and the relation between the gas temperature and the dark matter temperature. If such relations exist, we can use them to reduce the Jeans equation to fewer variables, which in turn will benefit observations of clusters of galaxies.

9.1 Perturbations

Before we perturb the structures, we let them run for $3t_u$ to make sure, they are in equilibrium. For the dark matter perturbations, we use structures containing one million particles, and the structures are perturbed twenty (S1a, S1b, S1c, S5a), thirty (S2a, S2b) and fifty (S3a, S3b, S4a, S4b) times. For the G perturbations we use structures containing one million particles, and each structure is perturbed twenty times. As for the adiabatic simulations, the first perturbation uses $\widetilde{G} = 1.2G$, the second $\widetilde{G} = 0.8G$, the third $\widetilde{G} = 1.2G$ and so on. Both the dark matter and G perturbations are evolved an additionally $5 \cdot 1.5t_u$ after the last perturbation to make sure the structures are in equilibrium. For the mergers, we use structures containing 100,000 particles, and the result of each merger will therefore contain 200,000 particles. The mergers are evolved for $20 \cdot 1.5t_u$.

9.2 Shape and Bulk Motion

Once again, we begin our analysis by examining the eccentricity and bulk motion of the perturbed structures.

In figure 9.1 we plot the eccentricity of the perturbed structures. As for the adiabatic simulations, they are grouped according to the type of perturbation. For the G perturbations and the mergers, the radial orbit instability has affected the structures S1b, S1c, S2b and S4b. However, we note that the structures are not as eccentric as the adiabatic structures. For example, the most eccentric of the adiabatic mergers has an eccentricity peaking at $\epsilon \approx 2.4$, while all the mergers with radiation and star formation have $\epsilon < 1.7$. A previous study has shown that dark matter halos in both galaxies and clusters of galaxies are significantly more spherical in simulations with gas cooling than in adiabatic simulations [20]. The reason is that the condensation of the gas due to cooling leads to a more concentrated dark matter distribution, as it responds to the increasing gravitational field of baryons in the centre (see figures B.4-B.5). Thus, cooling results in a significantly more centrally concentrated mass distribution and a deeper gravitational potential. This leads to a more spherical dark matter halo, since the overall potential becomes rounder as the central condensation grows. The dark matter perturbations shows no signs of neither the radial orbit instability nor a lower eccentricity. The explanation could be that fewer stars are created due to

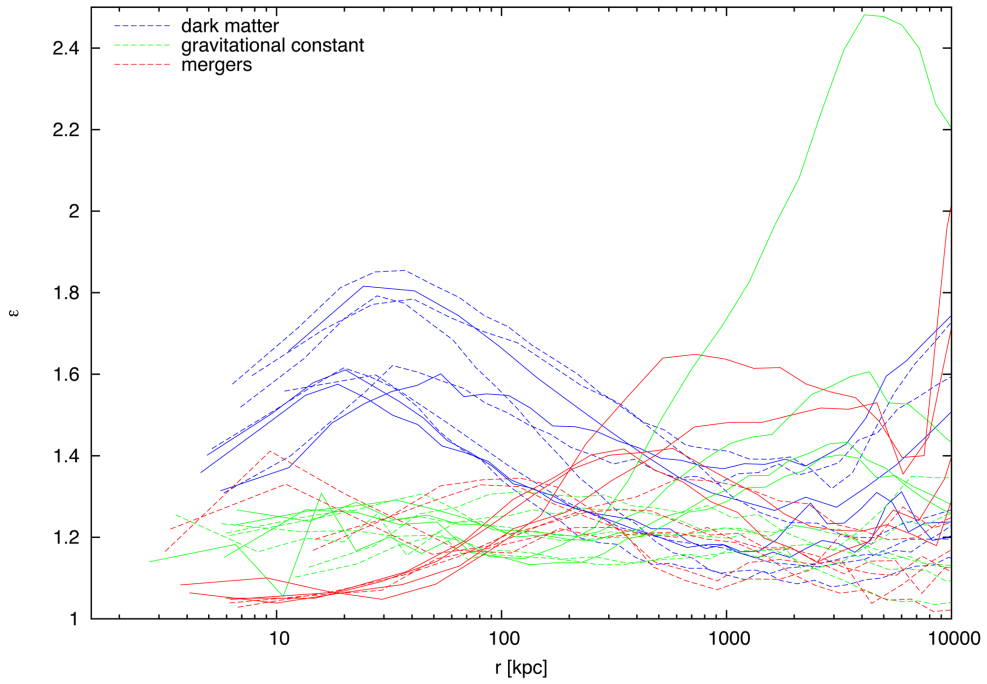

Figure 9.1: *The eccentricity of the final structures. The solid lines represent the structures S1b, S1c, S2b and S4b.*

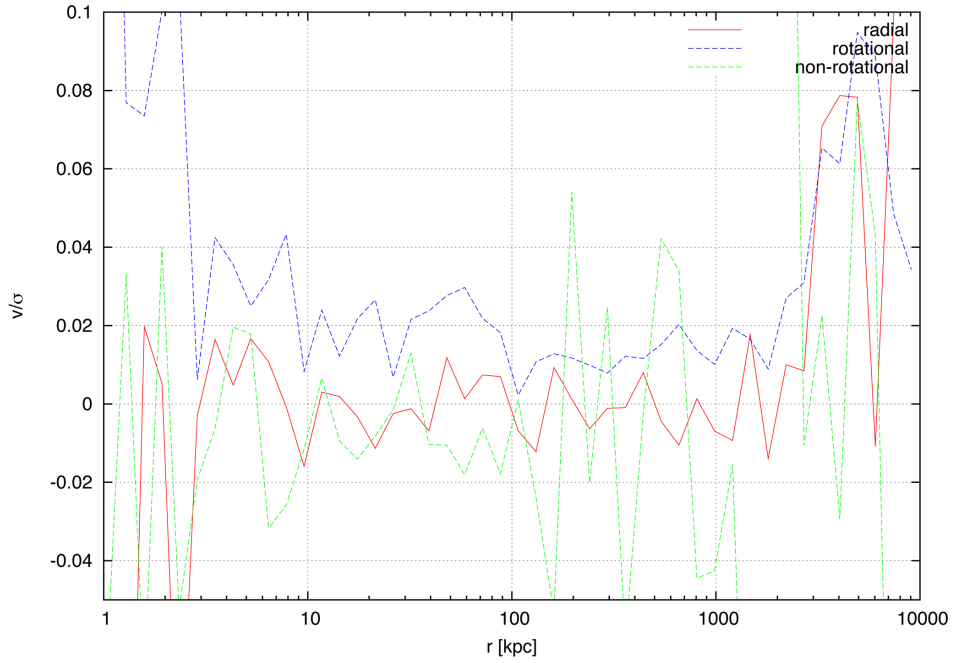

Figure 9.2: *The average dark matter velocities with respect to the velocity dispersion for the dark matter perturbed S1a.*

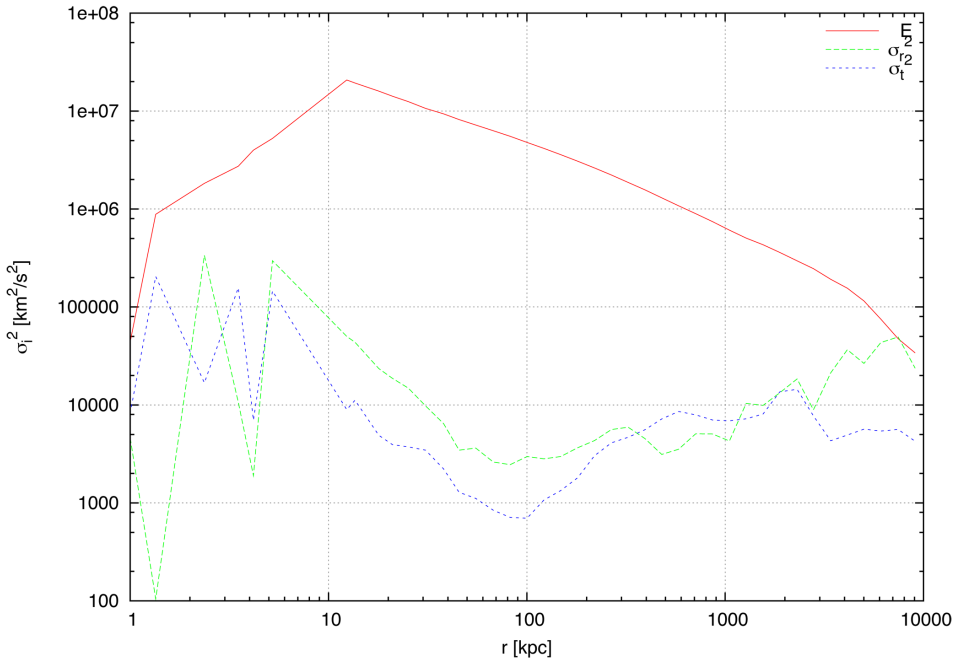

Figure 9.3: *The internal energy and the radial and tangential velocity dispersion for the dark matter perturbed S1a.*

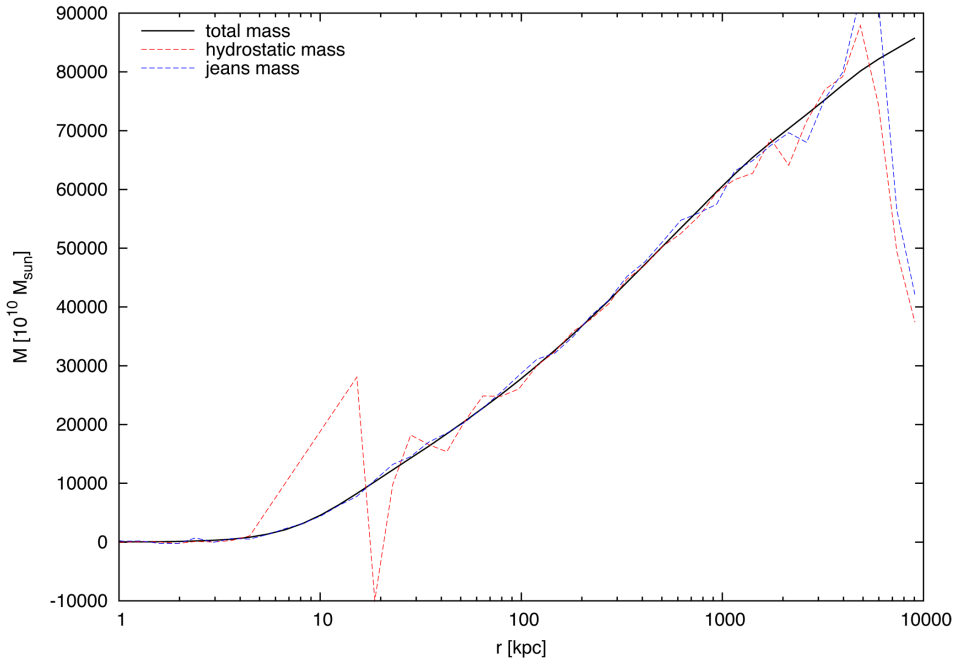

Figure 9.4: *The total mass, the Jeans mass and the hydrostatic mass for the dark matter perturbed S1a.*

the dark matter perturbations than to the G perturbations and mergers, since they are so mild.

For all the perturbed structures, the radial and tangential velocities of the dark matter fluctuate close to zero, and the rotational velocities are less than 5% of the rotational velocity dispersions. We can therefore conclude that the perturbed structures show no significant bulk motion. In figure 9.2 we plot the average dark matter velocities divided by the velocity dispersions of the dark matter perturbed S1a.

In figure 9.3 we compare the internal energy of the gas to the radial and tangential velocity dispersions of the gas for the dark matter perturbed S1a. In the inner region, the internal energy drops fast because of the increased cooling, and the velocity dispersion is affected by the star formation. Overall, the velocity dispersions are small compared to the internal energy, and we will therefore not need to take them into account, when we calculate the temperature of the gas. This is the case for all the perturbed structures.

In figure 9.4 we compare the total mass with the Jeans mass and the hydrostatic mass of the dark matter perturbed S1a. In the inner region the hydrostatic mass fluctuates because of the cooling and star formation, but further out both the hydrostatic mass and the Jeans mass match the total mass. For all three types of perturbations, the deviations from the total mass beyond the star forming region typically lies within 5%.

9.3 The Jeans Relation

In figures 9.5-9.7 we plot $\kappa + \gamma$ as a function of β for the dark matter of the perturbed structures. The initial conditions are the same as for the adiabatic simulations and can be seen in figure 8.9. Only points for which 2.5kpc $\leq r \leq$ 1000kpc are included.

In figure 9.5 the Jeans relation emerges once again, although this time it appears shifted slightly to the right in the inner region. Using the logarithmic derivative of the total density instead of just the dark matter density does not make any difference. Since the eccentricity of the dark matter perturbed structures are the same for both the adiabatic simulations and the simulations with radiation and star formation, it cannot be because of the binning method used. The shift must somehow be related to the presence of cooling and star formation.

For the G perturbations in figure 9.6 the Jeans relation also stands out despite the larger amount of scatter. Again, this must be attributed to the presence of cooling and star formation.

The mergers in figure 9.7 only hint at the Jeans relation. It is possible that additional mergers will make it stand out clearer.

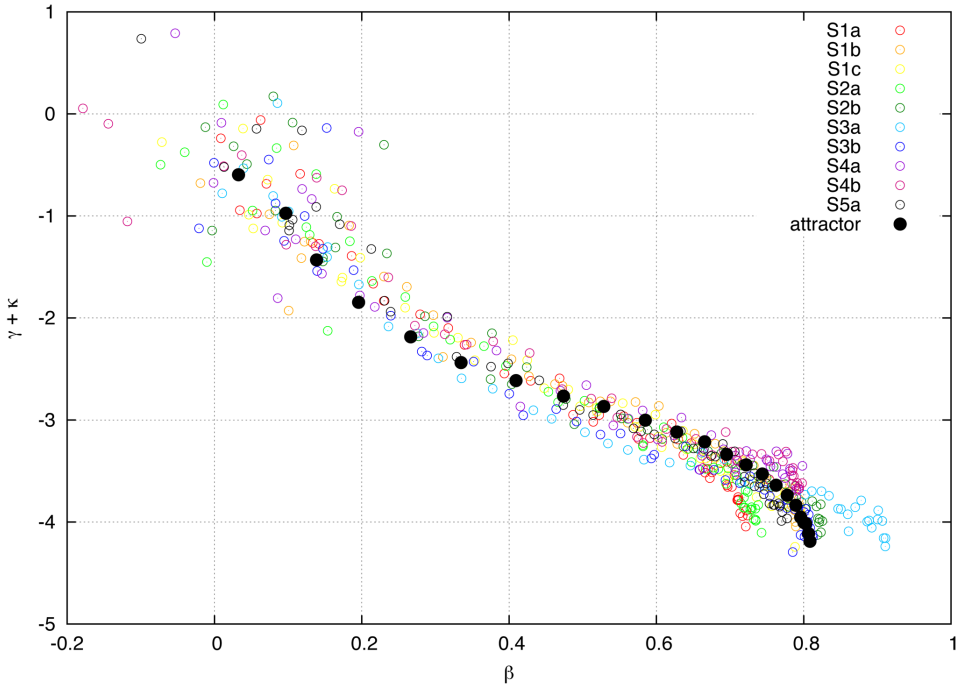

Figure 9.5: *The relation between $\gamma + \kappa$ and β for the dark matter perturbations.*

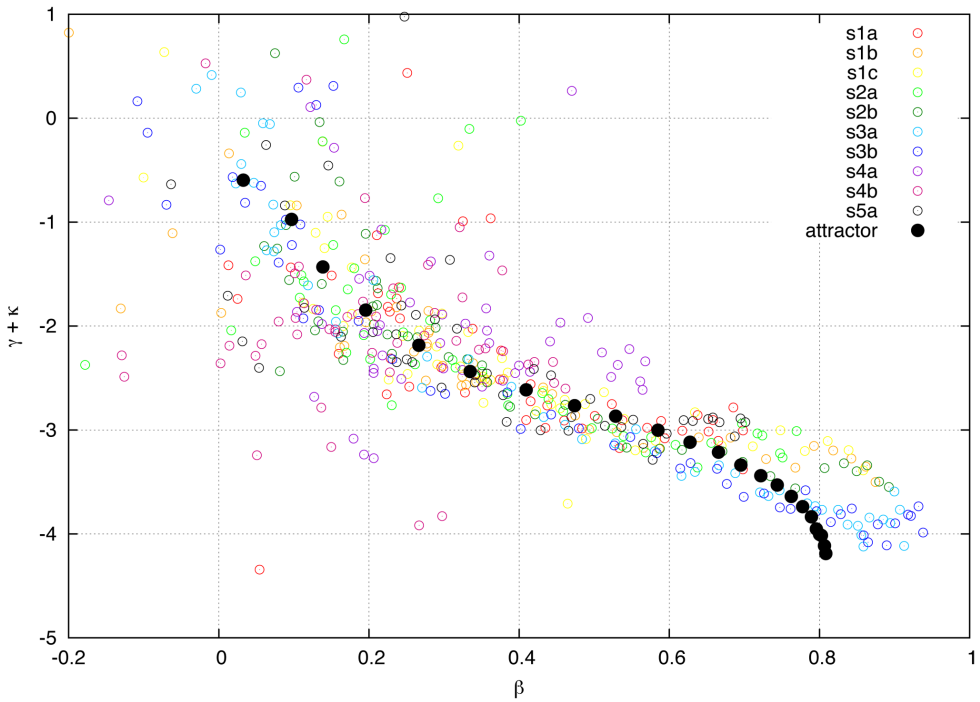

Figure 9.6: *The relation between $\gamma + \kappa$ and β for the G perturbations.*

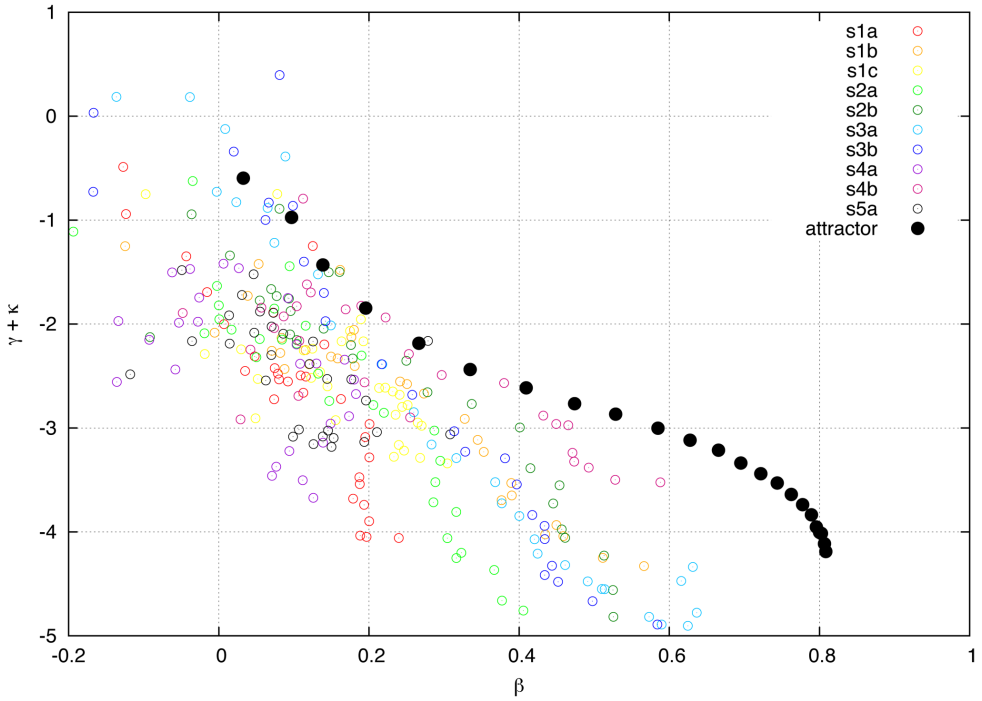

Figure 9.7: *The relation between $\gamma + \kappa$ and β for the mergers.*

9.4 The Temperature Relation

In figures 9.8-9.10 we plot Γ as a function of r for the perturbed structures. The initial conditions are the same as for the adiabatic simulations and can be seen in figure 8.13.

The dark matter perturbations clearly move the structures towards an attractor. As opposed to the adiabatic simulations, the perturbations do not stop affecting the structures after 30 perturbations. This is because the natural perturbation of the gas due to radiation and star formation keeps affecting the gas even when the dark matter has settled on its own attractor. These are very small perturbations, though, and even the 50 perturbations of S3a and S3b were not quite enough to bring the two structures all the way down to the rest of the structures. We see that the temperature relation decreases with the radius in the inner region. For 30kpc $< r <$ 120kpc the attractor is not close to unity as expected, but rather $\Gamma \approx 1.5 \pm 0.2$.

The G perturbations move the structures towards an attractor which lies at $\Gamma \approx 1 \pm 0.3$. The only exceptions are S3a and S3b which lie at $\Gamma \approx 1.5$. This is probably because they need to be perturbed more. In figure B.2 we see that additional perturbations do bring them closer to the rest of the structures, but since the violent perturbations have moved a lot of the gas away from the centres of the structures, we cannot see anything for $r <$ 100kpc.

In a previous study of cosmological simulations of galaxies, it has been shown

that $\Gamma \approx 1$ [14]. This agrees well with the results of our G perturbations, although the temperature relation of that study increases slightly with radius, while our relation appear to fluctuate around $\Gamma = 1$.

Since the dark matter perturbations and the G perturbations both move the dark matter towards the Jeans relation, the difference between their temperature relations must be because the perturbations affect the gas differently. In figures B.6 and B.7 we plot the perturbed gas density and gas temperature for the two types of perturbations, and we see that gas density and gas temperature of the dark matter perturbed structures consistently lie above the gas density and gas temperature of the G perturbed structures. Since the dark matter perturbations do not directly perturb the gas, the G perturbations probably best represent what happens during real, cosmological structure formation. If we were to compare these results with observations, we would therefore expect the G perturbed structures to be the best match.

The mergers exhibit a large spread ranging from $\Gamma \approx 1$ to $\Gamma \approx 2$. We cannot conclude anything without performing additional mergers.

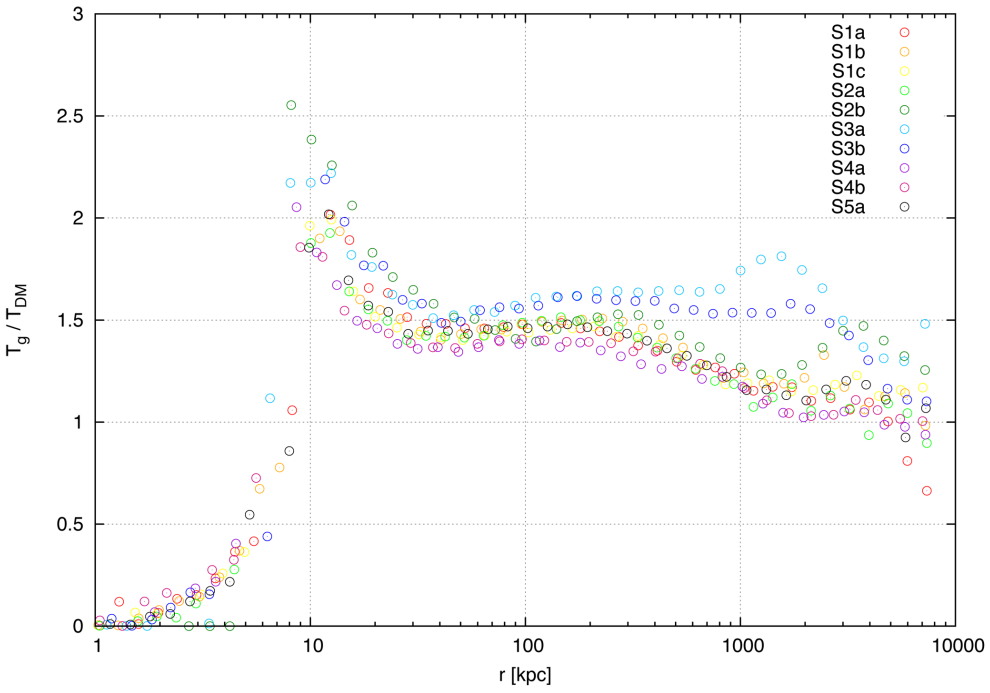

Figure 9.8: *The temperature relation for the dark matter perturbations.*

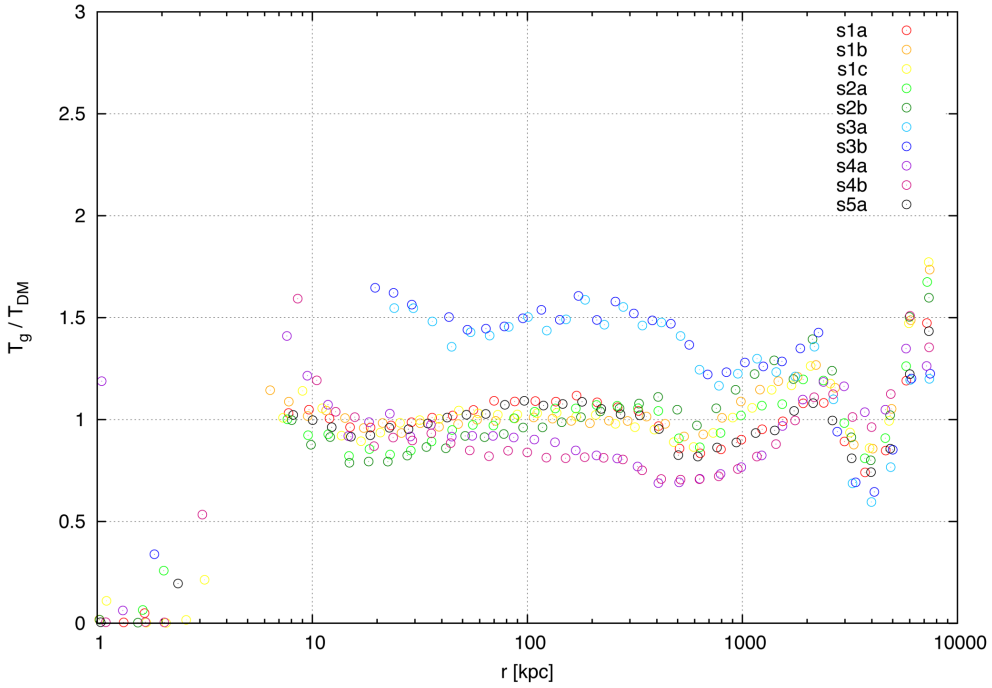

Figure 9.9: *The temperature relation for the G perturbations.*

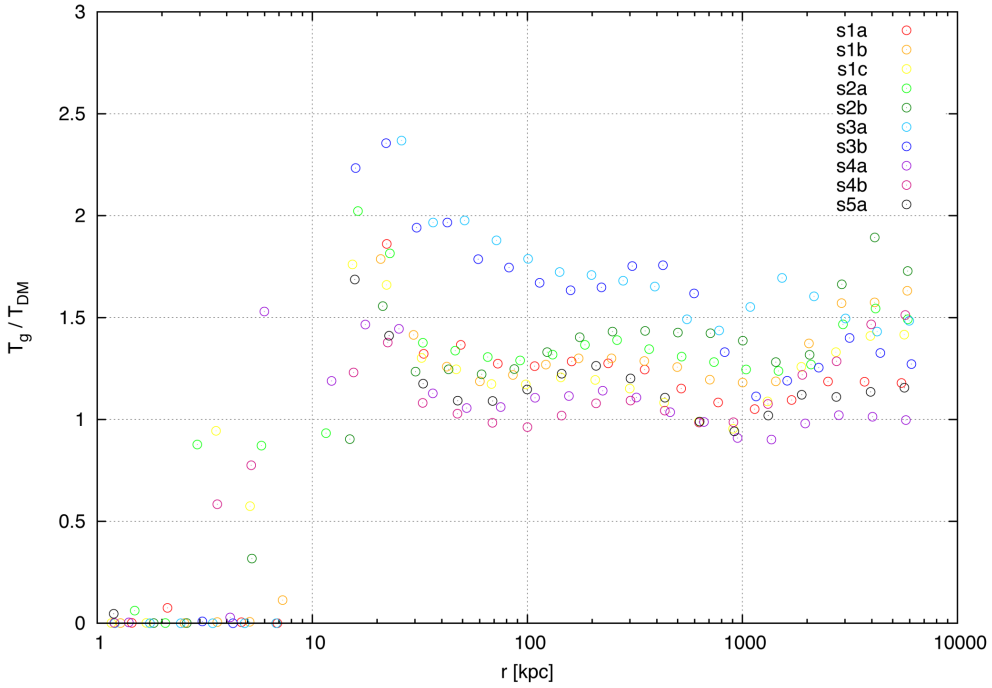

Figure 9.10: *The temperature relation for the mergers.*

10 Discussion

10.1 The Jeans Relation

In Section 3.3 we argued that the Jeans relation can be used to solve the mass velocity anisotropy degeneracy problem in dwarf galaxies. We will now go through the equations and show that this is indeed the case.

If the stars in a dwarf galaxy follow the Jeans relation, $\gamma_* + \kappa_* = A\beta_* + B$, we can write the Jeans equation

$$\begin{aligned} M(r) &= -\frac{r\sigma_{r_*}^2}{G}\left(\frac{\mathrm{d}\ln(\rho_*)}{\mathrm{d}\ln(r)} + \frac{\mathrm{d}\ln(\sigma_{r_*}^2)}{\mathrm{d}\ln(r)} + 2\beta_*(r)\right) \\ &= -\frac{r\sigma_{r_*}^2}{G}\left(\gamma_* + \kappa_* - \frac{2}{A}(\gamma_* + \kappa_* - B)\right) \\ &= -\frac{r\sigma_{r_*}^2}{G}\left((\gamma_* + \kappa_*)\left(1 - \frac{2}{A}\right) + \frac{2B}{A}\right). \end{aligned} \tag{10.1}$$

We see that the Jeans relation allows us to eliminate one variable, the velocity anisotropy, from the Jeans equation. First of all, this imposes restrictions on the available space for analytical solutions. Additional relations might eventually make it possible to completely solve the equation analytically. Secondly, it solves our velocity anisotropy degeneracy problem. The relation enables us to estimate the correct velocity anisotropy of the stars in a system, and we therefore have no free parameters when we subsequently calculate the total mass of the system.

10.2 The Temperature Relation

For structures containing dark matter, gas and stars, we can find the gas temperature and density by measuring the X-ray emission of the gas. We can then use the equation of hydrostatic equilibrium to find the total mass of the structure:

$$M(r) = -r\frac{k_B T_g}{\langle m_g\rangle G}\left(\frac{\mathrm{d}\ln(\rho_g)}{\mathrm{d}\ln r} + \frac{\mathrm{d}\ln(T_g)}{\mathrm{d}\ln r}\right). \tag{10.2}$$

This total mass is the same as the mass on the left hand side of the Jeans Equation:

$$M(r) = -\frac{r\sigma_{r_{\mathrm{DM}}}^2}{G}\left(\frac{\mathrm{d}\ln(\rho_{\mathrm{DM}})}{\mathrm{d}\ln(r)} + \frac{\mathrm{d}\ln(\sigma_{r_{\mathrm{DM}}}^2)}{\mathrm{d}\ln(r)} + 2\beta(r)\right). \tag{10.3}$$

On the right hand side we have three unknown dark matter quantities: ρ_{DM}, $\sigma_{r_{\mathrm{DM}}}^2$ and β. By observing the luminosity of the stars in the structure, we can find their density, and along with the density of the gas and the total mass of the structure, this allows us to calculate the dark matter density:

$$\rho_{\mathrm{DM}}(r) = \frac{1}{4\pi}\frac{\mathrm{d}M(r)}{\mathrm{d}r} - (\rho_g(r) + \rho_*(r)). \tag{10.4}$$

We are now left with two unknown variables on the right-hand-side of the Jeans Equation, $\sigma^2_{r_{\rm DM}}$ and β. If there exists a relation Γ between the gas temperature and the dark matter temperature, we can express $\sigma^2_{\theta_{\rm DM}} + \sigma^2_{\phi_{\rm DM}}$ as a function of T_g and $\sigma^2_{r_{\rm DM}}$:

$$\sigma^2_{\theta_{\rm DM}} + \sigma^2_{\phi_{\rm DM}} = \frac{T_g k_B}{\mu m_p \Gamma} - \sigma^2_{r_{\rm DM}}. \tag{10.5}$$

This allows us to express β as a function of $\sigma^2_{r_{\rm DM}}$ thereby eliminating one of the two unknowns:

$$\beta = \frac{1}{2} - \frac{T_g k_B}{2\mu m_p \Gamma \sigma^2_{r_{\rm DM}}}. \tag{10.6}$$

We are thus left with one unknown and a solvable equation. For a cluster of galaxies or even just a galaxy, the temperature relation makes it possible to deduce β from observations of the gas density, gas temperature and the stellar density. Note that this is possible even if Γ is not a simple constant. As long as we know the radial form of Γ, we can use the method described above. Such an indirect measurement of the velocity anisotropy can provide an independent confirmation of cosmological simulations, and to the suggestion that a non-zero β is a universal property of dark matter structures. Furthermore, a non-zero velocity anisotropy has an effect on the underground direct detection experiments, and a measurement of the velocity anisotropy would therefore decrease the systematic error-bars in these experiments [11, 39, 40].

10.3 Results

With the adiabatic simulations we have demonstrated that the Jeans relation for dark matter holds for structures containing both dark matter and gas, and that there appears to be no simple attractor for the ratio between the gas temperature and the dark matter temperature. Since the simulations did not include cooling and star formation, they do not reflect what happens in real clusters of galaxies, and the results are therefore not comparable to observations. Still, it has been useful to compare them with another adiabatic simulation.

We found that the Jeans relation for dark matter also holds for simulations with gas and radiation, although it appears to be shifted slightly to the right in the inner region. Analogous to the problem with the dwarf galaxies, we can use this relation to estimate the total mass of a cluster from observations of its galaxies alone. Furthermore, the found relation between the temperature of the gas and the temperature of the dark matter will enable us to find the otherwise unobservable velocity anisotropy of the dark matter in a cluster.

11 Conclusions

The goal of this thesis was to investigate the presence of attractors in clusters of galaxies both for adiabatic simulations and for simulations with radiation and star formation.

We successfully created ten very different structures in equilibrium, which we evolved using the TreeSPH code GADGET-2. We performed a number of thorough tests of the simulation parameters, before we submitted the structures to three different types of perturbations: perturbations of the dark matter only, perturbations of the gravitational constant, and mergers.

For the adiabatic simulations, we found that the eccentricity of the perturbed structures depended on the type of perturbations they had been exposed to, and how vulnerable they were to the effects of the radial orbit instability. None of the perturbed structures showed any signs of bulk motion, and despite their increased eccentricity, they all still fulfilled the equation of hydrostatic equilibrium and the Jeans equation. We found that both the dark matter perturbations and the G perturbations moved the dark matter towards the Jeans relation for dark matter. The mergers did as well, but they only managed to reach the relation in the inner part. We did not find any clear signs of an attractor for the relation between the gas temperature and the dark matter temperature as a function of the radius. However, we did notice that the relation appeared to group itself according to the density of the dark matter. We compared our results to that of another study of adiabatic mergers and found that to the extent they were comparable, they matched.

For the simulations with radiation and star formation, we again found that the eccentricity of the perturbed structures depended on the type of perturbation, but because of the presence of cooling, the eccentricities were not as large as for the adiabatic simulations. The structures satisfied the equation of hydrostatic equilibrium and the Jeans equation, although the gas deviated in the inner region, where it cooled rapidly and formed stars. Both the dark matter perturbations and the G perturbations moved the dark matter towards the Jeans relation for dark matter, although it appeared slightly shifted towards the right for the dark matter perturbations, and more scattered for the G perturbations. While the dark matter perturbations suggested an attractor for the temperature relation at $\Gamma \approx 1.5$, the G perturbations suggested an attractor at $\Gamma \approx 1$. Since the dark matter perturbations do not directly perturb the gas, the G perturbations probably best represent what happens during real, cosmological structure formation. We can use these results to 1) estimate the total mass of a cluster of galaxies by observing its galaxies, 2) indirectly measure the velocity anisotropy of a cluster of galaxies from observations of its gas and galaxies.

In a world of infinite time and computer power, it would have been obvious to perform more mergers, since they constantly fell short in the analysis. It would also have been interesting to see if G perturbations of a smaller strength, for

example 10%, would allow for more perturbations without ruining the structures too much. Finally, although there did not exist an attractor for the temperature relation as a function of radius for the adiabatic simulations, a deeper investigation might reveal that there exists one for a more complicated combination of variables.

A Equations

A.1 Mean Molecular Mass

To obtain the mean molecular mass of a gas of mass M, we assume that it is composed of three components: X (mass fraction of hydrogen), Y (mass fraction of helium) and Z (mass fraction of heavier elements). It follows that

$$X + Y + Z = 1. \tag{A.1}$$

Assuming that the gas is completely ionised, we can add the numbers of ions and electrons for each component in turn. For hydrogen the number of ions and electrons are

$$N_{\mathrm{H}^+} = \frac{XM}{m_u}, \tag{A.2}$$

$$N_{\mathrm{e}} = \frac{XM}{m_u}, \tag{A.3}$$

where m_u is the atomic mass constant. The two numbers are the same because a hydrogen atom contains one proton and one electron. For helium the number of ions and electrons are

$$N_{\mathrm{He}^{++}} = \frac{YM}{4m_u}, \tag{A.4}$$

$$N_{\mathrm{e}} = \frac{YM}{2m_u}, \tag{A.5}$$

since the helium atom contains two protons, two neutrons and two electrons. For the heavier elements we assume that they have a mean atomic mass of A. We can ignore the number of ions $N_{\mathrm{A}} = ZM/(Am_u)$, since they are negligible by comparison to the other contributions. The number of electrons is approximately

$$N_{\mathrm{e}} = \frac{ZM}{2m_u}. \tag{A.6}$$

We now add all the contributions to get the total number of particles:

$$N = \left(\frac{XM}{m_u} + \frac{XM}{m_u}\right) + \left(\frac{YM}{4m_u} + \frac{YM}{2m_u}\right) + \frac{ZM}{2m_u} \tag{A.7}$$

$$= \frac{M}{m_u}\left(2X + \frac{3}{4}Y + \frac{1}{2}Z\right). \tag{A.8}$$

The mean molecular mass is then

$$\mu = \frac{M}{Nm_u} \tag{A.9}$$

$$= \frac{1}{2X + \frac{3}{4}Y + \frac{1}{2}Z}. \tag{A.10}$$

A.2 Euler's Equation

Consider a small fluid element of density ρ, volume $\mathrm{d}V$ and mass

$$M = \int \rho \mathrm{d}V. \tag{A.11}$$

If the only two forces acting on the fluid element is a pressure force

$$\mathbf{F}_P = -\oint P \mathrm{d}\mathbf{S} = -\int \nabla P \mathrm{d}V, \tag{A.12}$$

and a gravitational force

$$\mathbf{F}_g = -M\nabla\Phi = -\int \rho \mathrm{d}V \nabla\Phi, \tag{A.13}$$

then the total force acting on the fluid element is

$$\mathbf{F}_{\mathrm{tot}} = \mathbf{F}_P + \mathbf{F}_g = -\int \nabla P \mathrm{d}V - \int \rho \mathrm{d}V \nabla\Phi. \tag{A.14}$$

The total force is also related to the mass and acceleration of the fluid element by

$$\mathbf{F}_{\mathrm{tot}} = M\frac{\mathrm{d}\mathbf{v}}{\mathrm{d}t} = \int \rho \mathrm{d}V \frac{\mathrm{d}\mathbf{v}}{\mathrm{d}t}. \tag{A.15}$$

Combining the two expressions for the total force we find that

$$\rho\frac{\mathrm{d}\mathbf{v}}{\mathrm{d}t} = -\nabla P - \rho\nabla\Phi. \tag{A.16}$$

While $\frac{\mathrm{d}}{\mathrm{d}t}$ describes a change of the element, $\frac{\partial}{\partial t}$ describes the change at a point. The change $\mathrm{d}\mathbf{v}$ in the interval $\mathrm{d}t$ is the sum of the change at a point, $\frac{\partial \mathbf{v}}{\partial t}$, and the change in $\mathbf{v}$ between two point separated by $\mathrm{d}\mathbf{x} = \mathbf{v}\mathrm{d}t$:

$$\begin{aligned} \mathrm{d}\mathbf{v} &= \frac{\partial \mathbf{v}}{\partial t}\mathrm{d}t + \sum_{i=1}^{3} \frac{\partial v_i}{\partial x_i}\mathrm{d}x_i \\ &= \frac{\partial \mathbf{v}}{\partial t}\mathrm{d}t + \sum_{i=1}^{3} \frac{\partial v_i}{\partial x_i}\mathrm{d}v_i\mathrm{d}t \\ &= \frac{\partial \mathbf{v}}{\partial t}\mathrm{d}t + (\mathbf{v}\cdot\nabla)\mathbf{v}\mathrm{d}t. \end{aligned} \tag{A.17}$$

We thus have that

$$\frac{\mathrm{d}\mathbf{v}}{\mathrm{d}t} = \frac{\partial \mathbf{v}}{\partial t} + (\mathbf{v}\cdot\nabla)\mathbf{v}. \tag{A.18}$$

Substituting this expression into equation (A.16) and dividing each term by ρ, we arrive at Euler's equation:

$$-\frac{1}{\rho}\nabla P - \nabla\Phi = \frac{\partial \mathbf{v}}{\partial t} + (\mathbf{v}\cdot\nabla)\mathbf{v}. \tag{A.19}$$

A.3 The Collisionless Boltzmann Equation

Consider an arbitrary closed volume V that is fixed in space and bounded by a surface S. The mass of the fluid in this volume is M. The continuity equation then states that the change of mass in the volume V is equal to the mass that flows through the surface S, and it is given by

$$\frac{\partial \rho}{\partial t} + \frac{\partial}{\partial \mathbf{x}} \cdot (\rho \dot{\mathbf{x}}) = 0. \tag{A.20}$$

The analogous equation for the conservation of probability in phase space is

$$\frac{\partial f}{\partial t} + \frac{\partial}{\partial \mathbf{w}} \cdot (f \dot{\mathbf{w}}) = 0. \tag{A.21}$$

The second term can be written

$$\frac{\partial}{\partial \mathbf{w}}(f \dot{\mathbf{w}}) = \dot{\mathbf{w}} \frac{\partial f}{\partial \mathbf{w}} + f \frac{\partial \dot{\mathbf{w}}}{\partial \mathbf{w}}. \tag{A.22}$$

For this equation the last term is zero since

$$\frac{\partial \dot{\mathbf{w}}}{\partial \mathbf{w}} = \sum_{i=1}^{6} \frac{\partial \dot{w}_i}{\partial w_i} = \sum_{i=1}^{3} \left(\frac{\partial v_i}{\partial x_i} + \frac{\partial \dot{v}_i}{\partial v_i} \right) = \sum_{i=1}^{3} \frac{\partial \dot{v}_i}{\partial v_i} = -\sum_{i=1}^{3} \frac{\partial}{\partial v_i} \left(\frac{\partial \Phi}{\partial x_i} \right) = 0. \tag{A.23}$$

We thus have that

$$\frac{\partial f}{\partial t} + \sum_{i=1}^{6} \dot{w}_i \frac{\partial f}{\partial w_i} = \frac{\mathrm{d} f}{\mathrm{d} t} = 0. \tag{A.24}$$

This is the collisionless Boltzmann equation.

A.4 The Jeans Equation

In spherical coordinates the collisionless Boltzman equation is given by

$$\begin{aligned} 0 = & \frac{\partial f}{\partial t} + v_r \frac{\partial f}{\partial r} + \frac{v_\theta}{r} \frac{\partial f}{\partial \theta} + \frac{v_\phi}{r \sin(\theta)} \frac{\partial f}{\partial \phi} \\ & + \left(\frac{v_\theta^2 + v_\phi^2}{r} - \frac{\partial \Phi}{\partial r} \right) \frac{\partial f}{\partial v_r} \\ & + \left(\frac{v_\phi^2 \cot(\theta) - v_r v_\theta}{r} - \frac{1}{r} \frac{\partial \Phi}{\partial \theta} \right) \frac{\partial f}{\partial v_\theta} \\ & + \left(\frac{-v_\phi v_r - v_\phi v_\theta \cot(\theta)}{r} - \frac{1}{r \sin(\theta)} \frac{\partial \Phi}{\partial \phi} \right) \frac{\partial f}{\partial v_\phi}. \end{aligned} \tag{A.25}$$

To obtain the Jeans equation we multiply the equation with v_r, v_θ and v_ϕ and integrate over the velocity space. This gives us one Jeans equation for each component of the potential gradient. The radial Jeans equation is

$$\begin{aligned}-\rho\frac{\partial\Phi}{\partial r} = \rho\frac{\partial\overline{v}_r}{\partial t} + \rho\left(\overline{v}_r\frac{\partial\overline{v}_r}{\partial r} + \frac{\overline{v}_\theta}{r}\frac{\partial\overline{v}_r}{\partial\theta} + \frac{\overline{v}_\phi}{r\sin(\theta)}\frac{\partial\overline{v}_r}{\partial\phi}\right)\\ + \frac{\partial}{\partial r}\left(\rho\sigma_{rr}^2\right) + \frac{1}{r}\frac{\partial}{\partial\theta}\left(\rho\sigma_{r\theta}^2\right) + \frac{1}{r\sin(\theta)}\frac{\partial}{\partial\phi}\left(\rho\sigma_{r\phi}^2\right)\\ + \frac{\rho}{r}\left[2\sigma_{rr}^2 - \left(\sigma_{\theta\theta}^2 + \sigma_{\phi\phi}^2 + \overline{v}_\theta^2 + \overline{v}_\phi^2\right) + \sigma_{r\theta}^2\cot(\theta)\right].\end{aligned} \tag{A.26}$$

To reduce this equation, we make a series of assumptions about the structure it describes. First of all, we assume that the structure is in equilibrium and therefore that $\partial/\partial t = 0$ and $\overline{v}_r = 0$. Secondly, we assume that there is no rotation such that $\overline{v}_\theta = \overline{v}_\phi = 0$. Thirdly, as the matrix representation of σ_{ij}^2 is symmetric and therefore can be diagonalised, we assume that the structure is spherically symmetric such that $\sigma_{r\theta}^2 = \sigma_{r\phi}^2 = \sigma_{\theta\phi}^2 = 0$. The equation now becomes

$$\frac{1}{\rho}\frac{\partial}{\partial r}(\rho\sigma_{rr}^2) + \frac{2\sigma_{rr}^2 - (\sigma_{\theta\theta}^2 + \sigma_{\phi\phi}^2)}{r} = -\frac{\partial\Phi}{\partial r} = -\frac{GM(r)}{r^2}, \tag{A.27}$$

where $M(r)$ is the total mass within the radius r. Using the definition of β and that

$$\frac{\mathrm{d}\ln(x)}{\mathrm{d}x} = \frac{1}{x} \Rightarrow \mathrm{d}\ln(x) = \frac{\mathrm{d}x}{x}$$

we can rewrite the radial Jeans equation to its final form:

$$M(r) = -\frac{r\sigma_r^2}{G}\left(\frac{\mathrm{d}\ln(\rho)}{\mathrm{d}\ln(r)} + \frac{\mathrm{d}\ln(\sigma_r^2)}{\mathrm{d}\ln(r)} + 2\beta(r)\right). \tag{A.28}$$

A.5 Sphere Point Picking

The area element of a sphere is

$$\mathrm{d}A = r^2\sin\theta\mathrm{d}\theta\mathrm{d}\phi. \tag{A.29}$$

If particles are distributed uniformly on the sphere, the probability of finding a given particle in $\mathrm{d}A$ is

$$P_A\mathrm{d}P_A = \frac{\mathrm{d}A}{4\pi r^2} = \frac{1}{4\pi}\sin\theta\mathrm{d}\theta\mathrm{d}\phi. \tag{A.30}$$

The probability densities for θ and ϕ are therefore

$$P_\theta(\theta)\mathrm{d}\theta = \int_0^{2\pi}\frac{1}{4\pi}\sin\theta\mathrm{d}\theta\mathrm{d}\phi = \frac{1}{2}\sin\theta\mathrm{d}\theta \tag{A.31}$$

$$P_\phi(\phi)\mathrm{d}\phi = \int_0^{\pi}\frac{1}{4\pi}\sin\theta\mathrm{d}\theta\mathrm{d}\phi = \frac{1}{2\pi}\mathrm{d}\phi. \tag{A.32}$$

Our goal is to generate numbers according to P_θ and P_ϕ by first generating uniformly distributed numbers $u_1 \in [0;1[$ and $u_2 \in [0;1[$ and then transforming them. For this we use the transformation method. For the variable θ we have

$$\begin{aligned} u_1 &= \int_0^{\theta(u_1)} P_\theta(\theta)\mathrm{d}\theta = \frac{1}{2}(1-\cos(\theta(u_1))) \\ &\Leftrightarrow \\ \theta(u_1) &= \arccos(1-2u_1). \end{aligned} \tag{A.33}$$

For the variable ϕ we have

$$\begin{aligned} u_2 &= \int_0^{\phi(u_2)} P_\phi(\phi)\mathrm{d}\phi = \frac{1}{2\pi}\phi(u_2) \\ &\Leftrightarrow \\ \phi(u_2) &= 2\pi u_2. \end{aligned} \tag{A.34}$$

A.6 Eccentricity of an Ellipsoid

To find the eccentricity of a uniform ellipsoid distribution of N particles, we start by placing the centre of mass

$$\mathbf{r}_c = \frac{\sum m_i \mathbf{r}_i}{\sum m_i}, \tag{A.35}$$

at the origo of a Cartesian coordinate system. We then calculate the moment of inertia tensor,

$$\mathbf{I} = \begin{bmatrix} I_{11} & I_{12} & I_{13} \\ I_{21} & I_{22} & I_{23} \\ I_{31} & I_{32} & I_{33} \end{bmatrix}$$

, where

$$\begin{aligned} I_{11} &= \sum_{i=1}^{N} m_i(y_i^2+z_i^2), \\ I_{22} &= \sum_{i=1}^{N} m_i(x_i^2+z_i^2), \\ I_{33} &= \sum_{i=1}^{N} m_i(x_i^2+y_i^2), \\ I_{12} &= I_{21} = -\sum m_i x_i y_i, \\ I_{13} &= I_{31} = -\sum m_i x_i z_i, \\ I_{23} &= I_{32} = -\sum m_i y_i z_i. \end{aligned}$$

Here I_{11} denotes the moment of inertia around the x-axis when the particles are rotated around the x-axis, I_{12} denotes the moment of inertia around the y-axis when the particles are rotated around the x-axis and so on. The axes of the ellipsoid do not necessarily coincide with the axes of the coordinate system. Since the tensor is both symmetric and real, we can diagonalise it:

$$\mathbf{I} = \begin{bmatrix} I_1 & 0 & 0 \\ 0 & I_2 & 0 \\ 0 & 0 & I_3 \end{bmatrix}$$

. The eigenvectors of this tensor now coincide with the axes of the ellipsoid, and the eigenvalues (I_1, I_2 and I_3) are therefore called the principal moments of inertia. The lengths of the axes of the ellipsoid are

$$a = \sqrt{\frac{5}{2}\frac{I_2 + I_3 - I_1}{M}}, \tag{A.36}$$

$$b = \sqrt{\frac{5}{2}\frac{I_1 + I_3 - I_2}{M}}, \tag{A.37}$$

$$c = \sqrt{\frac{5}{2}\frac{I_1 + I_2 - I_3}{M}}. \tag{A.38}$$

Defining the eccentricity as the ratio of the major axis to the minor axis we have

$$\epsilon = \frac{a}{c}. \tag{A.39}$$

A.7 Rotation

To find the radial, rotational and non-rotational velocity components of a particle, we first determine the direction of the angular momentum of the bin containing that particle. It is given by

$$\hat{\mathbf{L}} = \frac{\mathbf{L}}{|\mathbf{L}|}, \tag{A.40}$$

where

$$\mathbf{L} = \sum_{i=1}^{N} m_i(\mathbf{r} \times \mathbf{v}). \tag{A.41}$$

Here $\mathbf{r}$ and $\mathbf{v}$ are the Cartesian position and velocity vectors, respectively. The radial velocity component of the particle is

$$v_r = \frac{\mathbf{r} \cdot \mathbf{v}}{|\mathbf{r}|}, \tag{A.42}$$

the rotational velocity component of the particle is

$$v_\theta = \mathbf{v} \cdot \frac{\hat{\mathbf{L}} \times \mathbf{r}}{|\hat{\mathbf{L}} \times \mathbf{r}|}, \tag{A.43}$$

and the non-rotational velocity component of the particle is

$$v_\phi = \mathbf{v} \cdot \frac{(\hat{\mathbf{L}} \times \mathbf{r}) \times \mathbf{r}}{|(\hat{\mathbf{L}} \times \mathbf{r}) \times \mathbf{r}|}. \tag{A.44}$$

B Figures

B.1 Adiabatic Simulations

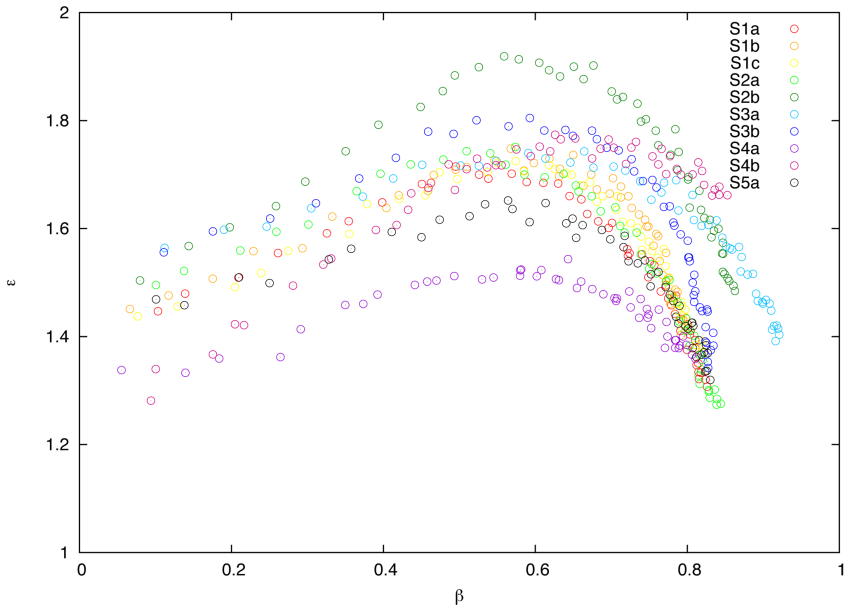

Figure B.1: *The eccentricity as a function of the velocity anisotropy for the dark matter perturbed strutures.*

B.2 Simulations with Radiation and Star Formation

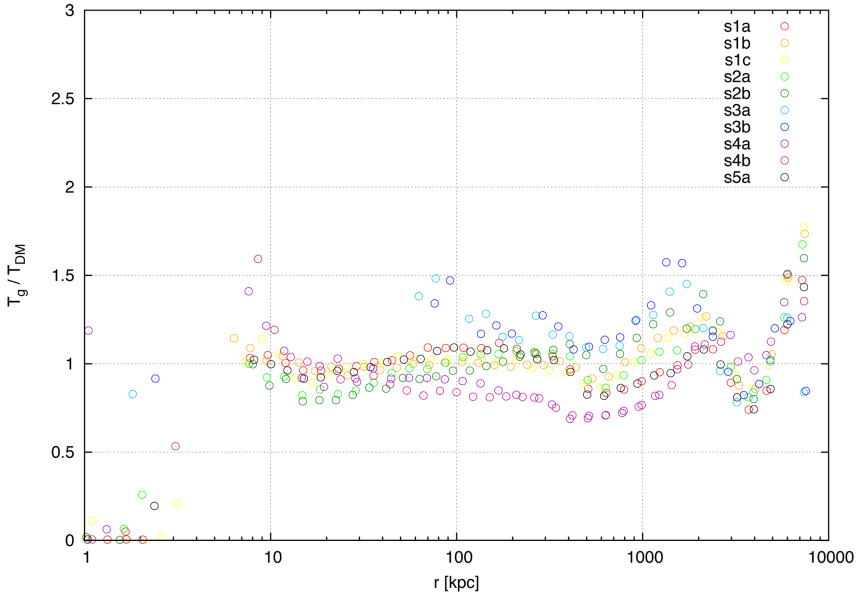

Figure B.2: *The temperature relation for the G perturbed structures. S3a and S3b have been perturbed 30 times.*

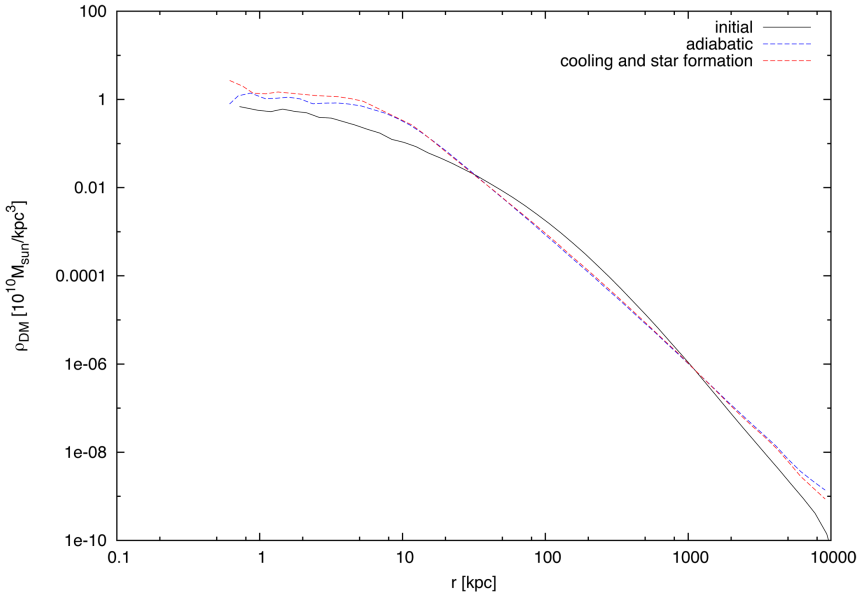

Figure B.3: *The initial and final dark matter perturbed dark matter densities for S1a.*

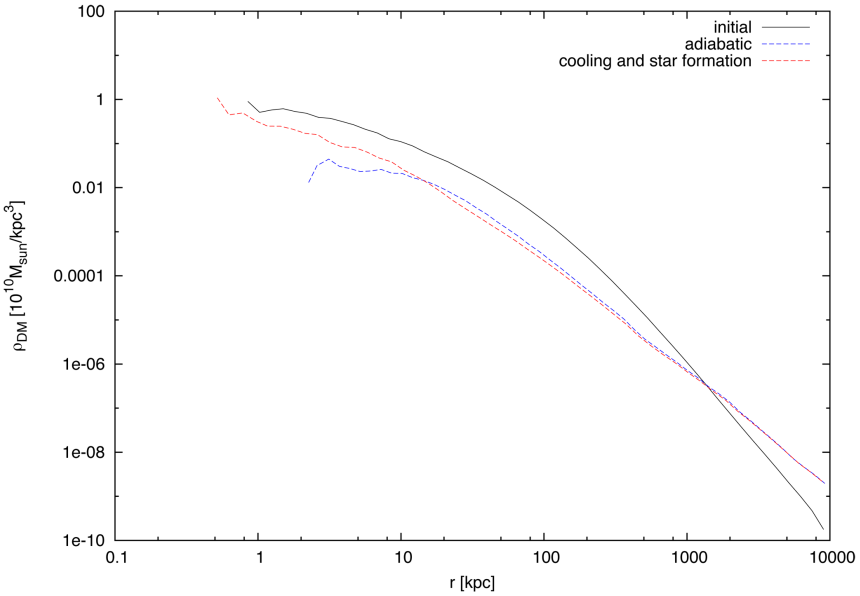

Figure B.4: *The initial and final G perturbed dark matter densities for S1a.*

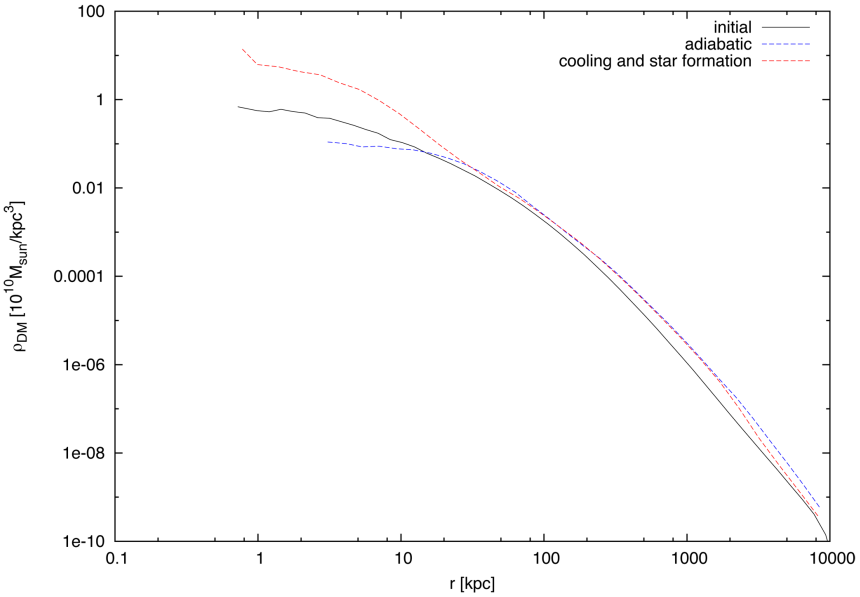

Figure B.5: *The initial and final dark matter densities for the merger of S1a.*

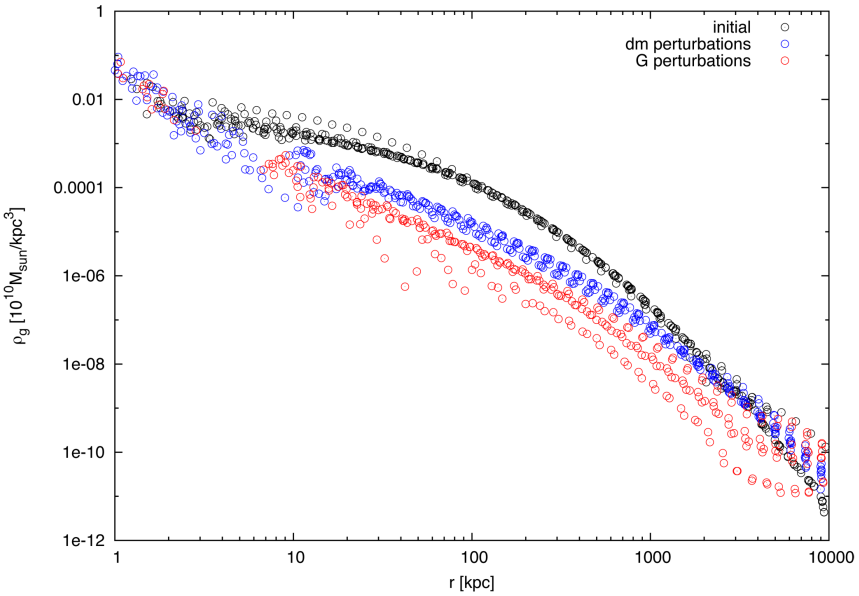

Figure B.6: *The initial, dark matter perturbed and G perturbed density of the gas.*

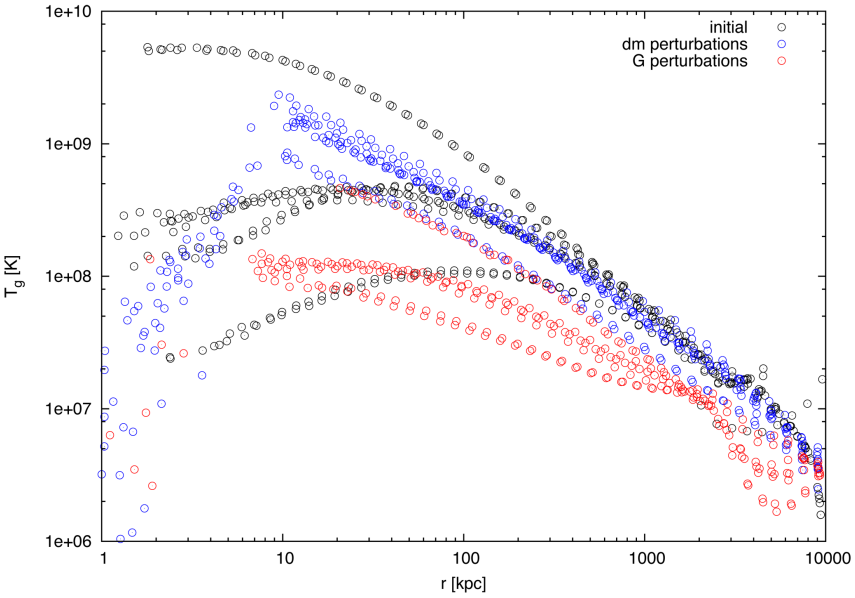

Figure B.7: *The initial, dark matter perturbed and G perturbed temperature of the gas.*

C Programs

I have written all the programs used for this project (except for GADGET-2). They are a mix of Fortran 95 and C programs. Below is a short description of the main programs.

mkstructure.f95
Creates a structure with a chosen dark matter density profile and velocity anisotropy.

merger.f95
Uses an already created structure to make a new file with to two copies of that structure. They are given velocities and positions that will make them merge.

random.f95
Returns a random number $u \in [0; 1[$.

sort.f95
Sorts an $m \times n$ array by a given column using the quick sort algorithm.

analyze.f95
Analyzes a structure by dividing the particles into logarithmic radial bins. Calculates all the properties needed to analyze a structure such as the average radius per bin, the velocity dispersion for each bin and the total mass within a given radius.

eccentricity.f95
Calculates the eccentricity of a structure by dividing the particles into logarithmic potential bins.

vel_avr.f95
Calculates the average velocities of the gas and dark matter.

particlepath.f95
Tracks the path of a single gas or dark matter particle.

scatter.f95
Creates a three-dimensional histogram by binning the radii of the particles of the same structure at two different times.

perturb.c
Perturbs the dark matter of a structure.

References

[1] E. I. Barnes, P. A. Lanzel, and L. L. R. Williams. The Radial Orbit Instability in Collisionless N-body Simulations. ApJ, 704:372–384, 2009.

[2] J. Barnes and P. Hut. A hierarchical $O(N \log N)$ force-calculation algorithm. Nature, 324:446–449, 1986.

[3] J. Binney and S. Tremaine. Galactic Dynamics. Princeton University Press, 1988.

[4] D. A. Boute and A. D. Lewis. The Dark Matter Radial Profile in the Core of the Relaxed Cluster A2589. ApJ, 604:116–124, 2004.

[5] T. Broadhurst, M. Takada, K. Umetsu, X. Kong, N. Arimoto, M. Chiba, and T. Futamase. The Surprisingly Steep Mass Profile of A1689, from a Lensing Analysis of Subaru Images. ApJ, 619:L143–L146, 2005.

[6] A. Cavaliere and R. Fusco-Femiano. X-rays from hot plasma in clusters of galaxies. AAp, 49:137–144, 1976.

[7] G. Chabrier. Galactic Stellar and Substellar Initial Mass Function. PASP, 115:763–795, 2003.

[8] L. Ciotti and L. Morganti. On the global density slope - anisotropy inequality. AIP Conference Proceedings, 1242:300–305, 2010.

[9] D. Clowe, A. Gonzalez, and M. Markevitch. Weak Lensing Mass Reconstruction of the Interacting Cluster 1E0657-558: Direct Evidence for the Existence of Dark Matter. ApJ, 604:596–603, 2004.

[10] S. Cole and C. Lacey. The Structure of Dark Matter Haloes in Hierarchical Clustering Models. MNRAS, 281:716–736, 1996.

[11] N. W. Evans, C. M. Carollo, and P. T. de Zeeuw. Triaxial Haloes and Particle Dark Matter Detection. MNRAS, 318:1131–1145, 2000.

[12] C. Grupen. Astroparticle Physics. Springer, 2005.

[13] S. H. Hansen, D. Juncher, and M. Sparre. An Attractor for Dark Matter Structures. ApJ, 718:L68–L72, 2010.

[14] S. H. Hansen, A. V. Maccio, E. Romano-Diaz, Y. Hoffman, M. Bruggen, E. Scannapieco, and G. S. Stinson. The Temperature of Hot Gas in Galaxies and Clusters: Baryons Dancing to the Tune of Dark Matter. ApJ, 734:62–72, 2010.

[15] S. H. Hansen and B. Moore. A universal density slope - velocity anisotropy relation for relaxed structures. NA, 11:333–338, 2006.

[16] S. H. Hansen and R. Piffaretti. Measuring the dark matter velocity anisotropy in galaxy clusters. AAp, 476:L37–L40, 2008.

[17] S. H. Hansen and J. Stadel. The velocity anisotropy - density slope relation. JCAP, 2006.

[18] L. Hernquist and N. Katz. TreeSPH: A unification of SPH with the hierarchical tree method. ApJ, 70:419–446, 1988.

[19] O. Host, S. H. Hansen, R. Piffaretti, A. Morandi, S. Ettori, S. T. Kay, and R. Valdarnini. Measurement of the Dark Matter Velocity Anisotropy in Galaxy Clusters. ApJ, 690:358–366, 2009.

[20] S. Kazantzidis, A. V. Kravtsov, A. R. Zentner, B. Allgood, D. Nagai, and B. Moore. The Effect of Gas Cooling on the Shapes of Dark Matter Halos. ApJ, 611:L73–L76, 2004.

[21] J. Lequeux. The Interstellar Medium. Springer, 2005.

[22] C. F. McKee and J. P. Ostriker. A theory of the interstellar medium - Three components regulated by supernova explosions in an inhomogeneous substrate. ApJ, 218:148–169, 1977.

[23] J. J. Monaghan and J. C. Lattanzio. A refined particle method for astrophysical problem. AAp, 149:135–143, 1985.

[24] B. Moster, A. V. Maccio, R. S. Somerville, P. H. Johansson, and T. Naab. Can Gas prevent the Destruction of Thin Stellar Discs by Minor Mergers? MNRAS, 403:1009–1019, 2009.

[25] J. F. Navarro, A. Ludlow, V. Springel, J. Wang, M. Vogelsberger, S. D. M. White, A. Jenkins, C. S. Frenk, and A. Helmi. The Diversity and Similarity of Simulated Cold Dark Matter Halos. MNRAS, 402:21–34, 2009.

[26] E. Pointecouteau, M. Arnaud, and G. W. Pratt. The structural and scaling properties of nearby galaxy clusters: I - The universal mass profile. AAp, 435:1–7, 2005.

[27] W. et al. Press. Numerical recipes in Fortran 77. Cambridge University Press, second edition, 1992.

[28] B. Ryden. Introduction to Cosmology. Benjamin Cummings, 2002.

[29] R. S. Somerville, P. F. Hopkins, T. J. Cox, B. E. Robertson, and L. Hernquist. A Semi-Analytic Model for the Co-evolution of Galaxies, Black Holes and Active Galactic Nuclei. MNRAS, 391:481–506, 2008.

[30] R. S. Somerville and J. R. Primack. Semi-Analytic Modeling of Galaxy Formation: The Local Universe. MNRAS, 310:1087, 1999.

[31] L. S. Sparke and J. S. Gallagher. Galaxies in the Universe. Cambridge University Press, 2007.

[32] V. Springel. The cosmological simulation code GADGET-2. MNRAS, 364:1105–1134, 2005.

[33] V. Springel and L. Hernquist. Cosmological SPH simulations: The entropy equation. MNRAS, 333:649–664, 2002.

[34] V. Springel and L. Hernquist. Cosmological SPH simulations: A hybrid multi-phase model for star formation. MNRAS, 339:289–311, 2003.

[35] V. Springel, N. Yoshida, and S. D. M. White. GADGET: A code for collisionless and gasdynamical cosmological simulations. NA, 6:79–117, 2001.

[36] J. Stadel, D. Potter, B. Moore, J. Diemand, P. Madau, M. Zemp, M. Kuhlen, and V. Quilis. Quantifying the heart of darkness with GHALO - a multi-billion particle simulation of our galactic halo. MNRAS, 398:L21–L25, 2009.

[37] R. S. Sutherland and M. A. Dopita. Cooling Functions for Low-Density Astrophysical Plasmas. ApJS, 88:253–327, 1993.

[38] J. E. Taylor and J. F. Navarro. The Phase-Space Density Profiles of Cold Dark Matter Halos. ApJ, 563:483–488, 2001.

[39] J. D. Vergados. The modulation effect for supersymmetric dark matter detection with asymmetric velocity dispersion. PRD, 62, 2000.

[40] J. D. Vergados, S. H. Hansen, and Host O. The impact of going beyond the Maxwell distribution in direct dark matter detection rates. PRD, 77, 2008.

[41] A. Vikhlinin, A. Kravtsov, W. Forman, C. Jones, M. Markevitch, S. S. Murray, and L. Van Speybroeck. Chandra Sample of Nearby Relaxed Galaxy Clusters: Mass, Gas Fraction and Mass-temeprature Relation. ApJ, 640:691–709, 2006.

[42] J. ZuHone. A Parameter Space Exploration of Galaxy Cluster Mergers I: Gas Mixing and the Generation of Cluster Entropy. ApJ, 728:54–79, 2011.